

**MOLECULAR DYNAMICS SIMULATION OF HEAT TRANSPORT ACROSS  
SILICON-CARBON NANOTUBES INTERFACE**

**By**

**TAEJIN KIM**

A dissertation submitted in partial fulfillment of  
the requirements for the degree of

**DOCTOR OF PHILOSOPHY**

**WASHINGTON STATE UNIVERSITY**  
Materials Science Program

December 2007

To the Faculty of Washington State University:

The members of the Committee appointed to examine the dissertation of KIM TAEJIN find it satisfactory and recommend that it be accepted.

---

Chair

---

---

---

---

## ACKNOWLEDGEMENTS

I would like to thank to advisor Dr. Mohamed A. Osman. He provided me a great chance to study molecular dynamics simulation and carbon nanotubes. During 3 and half years PhD program in materials science program, he advised me from the very beginning of research behaviors to advanced research approaches. I learned how to prepare the presentation and what I need to stress on depending on the purpose of presentation. In writing a paper, he taught me very detailed writing skills and helped me to publish the paper, “Molecular Dynamic Simulation of Heat Pulse Propagation in Multiwall Carbon Nanotubes”. In developing molecular dynamics simulation codes, he provided me technique of how to start develop and test the codes.

I would like to thank to PhD program committees, Dr. Cill Richards, Dr. Bob Richards, and Dr. Matthew McCluskey. The MEMS group under Cill Richards, Dr. Bob Richards’s advice provided me a grate chance to do research on thermal interfacial resistance. It was a difficult research topic, however, it also provided me lots of experiences in developing molecular dynamics simulation codes and related codes. I also thank them for their advices during my PhD research. Dr. Matthew McCluskey provided a very helpful idea how to interoperate the atomic motion at the leading heat wave packets in heat pulse propagation on carbon nanotube. He also provided very careful corrections on this thesis. I would like to thank to Dr. David Bahr. He provided very helpful advice on the silicon surface condition, which was related on the most difficult problem of structure breaking down.

I would like to thank to Dr. Jeong-Hyun Cho. He provided me very helpful conceptions and images of experimental conditions. I also thank him for everything he did for me as a good friend.

I also thank for the National Science Foundation (NSF), Grant # CTS 0404370.

**MOLECULAR DYNAMICS SIMULATION OF HEAT TRANSPORT ACROSS  
SILICON-CARBON NANOTUBES INTERFACE**

Abstract

by KIM TAEJIN, Ph.D.

Washington State University

December 2007

Chair: Mohamed A. Osman

Thermal interfacial resistance across single wall nanotube (SWNT) and silicon interface is investigated by molecular dynamics (MD) simulation. The effect of the interaction on thermal interfacial resistance is studied by applying bonded interaction as sum of bonded and non-bonded van der Waals interactions, and only non-bonded van der Waals interaction on the interface. For both cases, different temperature discontinuities (drops) at the interface are obtained. It is found that the thermal interfacial resistance of non-bonded interaction at the 3Å separation is 20 times greater than that of the bonded interaction. At 300K, the thermal interfacial resistance of the bonded interaction is  $2.85 \times 10^{-9} \text{m}^2\text{K/W}$  and that of non-bonded interaction is  $5.65 \times 10^{-8} \text{m}^2\text{K/W}$ . It is also found

that the thermal interface resistance decreases as temperature increases up to room temperature. The low frequency radial phonon modes in CNT are excited due to the coupling with silicon phonon modes and contribute the heat transport across interface under the bonded interaction. In contrast, no change of radial phonon mode in non-bonded interaction is found. The excitation of the radial breath mode (RBM) and low frequency radial phonon modes increase with temperature and transport more heat energy across interface and results in lowering the thermal interfacial resistance at high temperature.

The propagation of heat pulses in zigzag and armchair double wall nanotubes (DWNTs) are also investigated using molecular dynamics simulations. It is found that the leading heat wave packets in zigzag (9,0)/(18,0) and armchair (5,5)/(10,10) DWNT move with the speed of longitudinal acoustic (LA) phonon modes. The intensities of the leading heat wave packets in outer and inner shells in DWNTs were found to be five to seven times larger than that of the corresponding single wall nanotubes (SWNT). The heat energy carried by the leading heat wave packets in zigzag DWNT was about four and five times more than those in armchair DWNT shells. Within the leading LA wavepacket, the strain in the inner shell of the DWNTs is stronger than strain in the outer shell and considerably larger than strain in the corresponding SWNTs. The regions with the largest strain coincide with the regions of high kinetic temperatures within the LA mode wave packets. The higher energy of the LA mode waves in DWNT shells compared to SWNT is attributed to the presence of higher strain fields in DWNT compared to individual SWNT. The higher strain in the inner shell of DWNT compared to the outer shell accounts for the three to five

times higher kinetic energy of leading wave packets in inner shells compared to those in outer shells. The induced strain fields in zigzag DWNT are distributed over a wider region compared to armchair DWNT and the strain in inner and outer shells of zigzag DWNT are out phase by  $180^\circ$

## TABLE OF CONTENTS

ACKNOWLEDGEMENTS.....	iii
ABSTRACT.....	v
LIST OF TABLE.....	xi
LIST OF FIGURES.....	xii

### CHAPTERS

<b>1. INTRODUCTION</b>	<b>1</b>
<b>2. CARBON NANOTUBES AND THERMAL SWITCH</b>	<b>10</b>
2.1 Physical structure of carbon nanotubes.....	10
2.2 Thermal Properties of Carbon Nanotubes.....	12
2.3 Thermal Switch and Thermal Interfacial Resistance.....	19
<b>3. MOLECULAR DYNAMICS</b>	<b>28</b>
3.1 Introduction.....	28
3.2 General Method.....	28
3.3 The Nordsieck-Gear Predictor-Corrector Method.....	30
3.4 Tersoff Potential and Tersoff-Brenner Potential.....	32

3.5	The Lennard-Jones (LJ) Potential.....	35
3.6	Calculating Physical Properties From the MD Simulations.....	37
3.7	Energy Minimization of Multiwall Carbon Nanotubes.....	39
<b>4.</b>	<b>MOLECULAR DYNAMICS SIMULATIONS FOR SILICON-CARBON</b>	
	<b>NANOTUBES INTERFACE</b>	<b>41</b>
4.1	Introduction.....	41
4.2	Bulk Silicon.....	41
4.3	Silicon Surface and Absorption of CNT.....	44
4.4	Silicon Carbide.....	50
<b>5.</b>	<b>HEAT PULSE PROPAGATION IN DOUBLE WALL CARBON</b>	
	<b>NANOTUBES</b>	<b>54</b>
5.1	Introduction.....	54
5.2	Methodology.....	58
5.3	Results and Discussion.....	61
5.4	Summary and Conclusion.....	78
<b>6.</b>	<b>MOLECULAR DYNAMICS SIMULATION OF CARBON NANOTUBES</b>	
	<b>AND SILICON INTERFACE</b>	<b>80</b>

6.1	Introduction.....	80
6.2	Methodology.....	81
6.3	Results and Discussion.....	87
6.4	Thermal Interfacial Resistance of Zigzag SWNT, DWNTs.....	97
6.5	Thermal Interfacial Resistance of (5,5) CNT Bundle.....	102
6.6	Summary and Conclusion.....	106
 <b>Appendix A CARBON NANOTUBES</b>		<b>108</b>
A. 1	Introduction.....	108
A. 2	Hybridization of Carbon Atom.....	108
A. 3	Tight Binding calculation of Molecules and Solids.....	111
A. 4	Electronic structure of Polyacetylene.....	115
A. 5	Two Dimensional Graphite (Graphene).....	118
A. 6	Electronic Structure of Carbon Nanotube.....	121
 <b>REFERENCES.....</b>		<b>124</b>

## LIST OF TABLE

1.1	The measured thermal interfacial resistance of CNT, silicon, mercury droplets and TIMs.....	8
1.2	The results of thermal interfacial resistance of CNT interface with MD simulations.....	9
3.1	The Tersoff parameters for the carbon and silicon.....	35
4.1	Predicted atoms displacements by GVA-PP(1), which are induced by symmetric dimer formation in the Si <sub>9</sub> H <sub>12</sub> model of the Si (001) surface.....	46
4.2	Staking sequence in the c-axis direction for different SiC polytypes.....	51

## LIST OF FIGURES

<b><u>Fig. 2.1</u></b>	The unrolled hexagonal lattice of a nanotube.....	10
<b><u>Fig. 2.2</u></b>	The structure and cross sectional shape of (a)armchair, (b)zigzag and (c)chiral nanotubes.....	11
<b><u>Fig. 2.3</u></b>	Heat (Q) flows from hot reservoir $T_H$ to cold reservoir $T_C$ through a material of cross-sectional area A and length L.....	13
<b><u>Fig. 2.4</u></b>	Thermal conductivity of (a) graphite and (b) diamond.....	14
<b><u>Fig. 2.5</u></b>	Thermal conductivity of multi wall carbon nanotubes (MWNT).....	15
<b><u>Fig. 2.6</u></b>	(a) the normal $\vec{K}_1 + \vec{K}_2 = \vec{K}_3$ and (b) the Umklapp $\vec{K}_1 + \vec{K}_2 = \vec{K}_3 + \vec{G}$  phonon collision process in a two-dimensional square lattice. The square in each figure represents the first Brillouin zone in the phonon $\vec{K}$ space.....	16
<b><u>Fig. 2.7</u></b>	The operation of thermal switch at (a) ‘OFF’ and (b) ‘ON’.....	19
<b><u>Fig. 2.8</u></b>	(a) Liquid-metal micro droplets and (b) vertically aligned carbon nanotube Arrays.....	20
<b><u>Fig. 2.9</u></b>	The thermal resistance of bare silicon, VACNT and mercury droplets for the switch (a) ‘OFF’ and (b) ‘ON’ operation.....	21
<b><u>Fig. 2.10</u></b>	(a) MD simulation configuration for thermal interfacial resistance between two (10,10) CNT and (b) the results of thermal interfacial resistance as a function of separation distance and the length of CNTs.	

	The overlap length between CNTs was 2.5nm.....	26
<b><u>Fig. 3.1</u></b>	The lattice structure of silicon, which is diamond crystal lattice.....	32
<b><u>Fig. 3.2</u></b>	Lennard-Jones 12-6 potential.....	36
<b><u>Fig. 3.3</u></b>	The configuration of Fourier method.....	38
<b><u>Fig. 3.4</u></b>	The structure looking of (a) armchair and (b) zigzag DWCNTs.....	39
<b><u>Fig. 3.5</u></b>	The results of energy distribution as a function of rotating inner shell of (a) (5,5)/(10,10), (b) (9,0)/(18,0) DWNTs and (c) shifting inner shell along z axis.....	40
<b><u>Fig. 4.1</u></b>	The configuration of applying Fourier method to the bulk silicon.....	42
<b><u>Fig. 4.2</u></b>	The phonon spectrum (a) from MD simulation and (b) soild line: density of state and points; two phonon Raman spectrum.....	43
<b><u>Fig. 4.3</u></b>	Dimer formation on the Si (100) surface.....	44
<b><u>Fig. 4.4</u></b>	Displacements of atoms near surface which is induced by the dimer formation in the Si <sub>9</sub> H <sub>12</sub> model. Displacements are indicated by arrows from bulk atom locations.Si <sub>9</sub> H <sub>12</sub> model of the Si (001). Arrows indicate displacements from bulk atom locations.....	45
<b><u>Fig. 4.5</u></b>	Carbon nanotube adsorption sites on Si (001) stepped surfaces.....	47
<b><u>Fig. 4.6</u></b>	Adsorbed (5,5) CNT and its atomic and electronic structure on the terraces of Si (001). (a) the relaxed structure and (b) the band structure of the CNT at site A (c) the band structure of 4H atoms bonded to the nanotube. (d) the geometry of atom and (e) the CNT band structure adsorbed at the site B, (f) The band structure of the (5,5) CNT bonded	

	with 4H atoms. The Fermi levels $E_F$ are indicated by the horizontal dashed lines.....	48
<b><u>Fig. 4.7</u></b>	The atomic and electronic structure of the CNT which is adsorbed (a) $D_B$ step edge, site E, and (c) at step edge site G. the energy bands (b) of the CNT adsorbed at the (b) site E and (d) site G.....	50
<b><u>Fig. 4.8</u></b>	Staking sequences for different SiC polytypes in the [1120] plane.....	51
<b><u>Fig. 4.9</u></b>	(a) The zinc blende lattice structure of the $\beta$ -SiC and (b) the generated bulk size of $\beta$ -SiC.....	52
<b><u>Fig. 4.10</u></b>	The configuration of applying Fourier method to the bulk $\beta$ -SiC.....	53
<b><u>Fig. 5.1</u></b>	The structure of a cell of (a) zigzag CNT and (b) armchair CNT shows the parameters for bond stretching and bond bending.....	61
<b><u>Fig. 5.2</u></b>	Temporal and spatial distribution of kinetic temperature along zigzag DWNT.....	62
<b><u>Fig. 5.3</u></b>	Spatial distribution of kinetic temperature at 5ps after application of heat pulse: (a) zigzag DWNT, (b) (9,0) inner shell and (c) (18,0) outer shell.....	63
<b><u>Fig. 5.4</u></b>	Spatial distribution of kinetic temperature at 5ps along (a) (9,0) SWNT and (b) (18,0) SWNT.....	64
<b><u>Fig. 5.5</u></b>	The distribution of strain $\epsilon$ in (9,0)/(18,0) DWNT (a) inner shell and (b) outer shell.....	66
<b><u>Fig. 5.6</u></b>	The distribution of strain $\epsilon$ in (a) (9,0) SWNT and (b) (18,0) SWNT.....	67
<b><u>Fig. 5.7</u></b>	Velocity distribution along (9,0) inner shell of (9,0)/(18,0) DWNT.....	69

<b><u>Fig. 5.8</u></b>	Temporal and spatial distribution of kinetic temperature along armchair (5,5)/(10,10) DWNT.....	70
<b><u>Fig. 5.9</u></b>	Spatial distribution of kinetic temperature at 5ps along (a) armchair (5,5)/(10,10) DWNT, (b) (5,5) inner shell and (c) (10,10) outer shell.....	71
<b><u>Fig. 5.10</u></b>	Spatial distribution of kinetic temperature at 5ps along (a) (5,5) SWNT and (b) (10,10) SWNT.....	72
<b><u>Fig. 5.11</u></b>	The distribution of strain within the leading wave packets in (5,5)/(10,10) DWNT (a) inner shell and (b) outer shell.....	73
<b><u>Fig. 5.12</u></b>	The distribution of strain within the leading wave packets in (a) (5,5) SWNT and (b) (10,10) SWNT.....	74
<b><u>Fig. 5.13</u></b>	Spatial distribution of kinetic temperature at 5ps along (10,10)/(15,15) DWNT: (a) (10,10) inner shell and (b) (15,15) outer shell.....	75
<b><u>Fig. 5.14</u></b>	The distribution of strain within the leading wave packets in (10,10)/(15,15) DWNT (a) inner (10,10) shell and (b) outer (15,15) shell.....	76
<b><u>Fig. 5.15</u></b>	Kinetic temperature of the leading LA mode wave packets in zigzag DWNT (solid line) and armchair DWNT (dashed line).....	77
<b><u>Fig. 6.1</u></b>	(a) The cross section of silicon groove which (11,11) SWNT is positioned at the center and (b) side view of the CNT-silicon interface. Both ends (gray) are fixed and 2 slabs in CNT is hot slabs with $T_{hot} = T_{amb} + 50K$ and 2 slabs in silicon is cold slabs with $T_{cold} = T_{amb} - 50K$ .....	82
<b><u>Fig. 6.3</u></b>	The distribution of bonded pairs of (a) (10,10) SWNT and (b) (11,11) SWNT in the silicon groove.....	83

<b><u>Fig. 6.4</u></b>	Temperature profile of (a) bonded interaction and (b) non-bonded Interaction.....	88
<b><u>Fig. 6.5</u></b>	Thermal interfacial resistance of (a) bonded interaction and (b) non-bonded interaction.....	89
<b><u>Fig. 6.6</u></b>	Heat flux density of bonded interactions and non-bonded interaction.....	90
<b><u>Fig. 6.7</u></b>	The phonon power spectrum of silicon and CNT ends: (a) radial component (CNT), (b) axial component (CNT) and (c) axial component (silicon).....	92
<b><u>Fig. 6.8</u></b>	The phonon power spectrum of CNT inside silicon groove: (a) radial component, (b) axial component in bonded interactions, (c) radial component in non-bonded interaction and (d) axial component in non-bonded interaction.....	94
<b><u>Fig. 6.9</u></b>	The phonon spectrum of silicon groove in (a) bonded interaction and (b) non-bonded interaction. The radial phonon power spectrum of CNT in groove with bonded interactions at (c) 100K and (d) 300K.....	96
<b><u>Fig. 6.10</u></b>	(a) The cross section and (b) the side view of (19,0) SWNT in the silicon groove and structure of (19,0) SWNT. The diameter and length of (19,0) CNT is 1.506nm and 9.83nm, respectively.....	98
<b><u>Fig. 6.11</u></b>	Temperature profile of (19,0) SWNT and silicon at T=300K.....	99
<b><u>Fig. 6.12</u></b>	The cross section of (a) armchair (6,6)/(11,11) DWNT, (b) zigzag DWNT (10,0)/(19,0), the side view of (c) armchair (6,6)/(11,11)	

	DWNT, (d) zigzag DWNT (10,0)/(19,0). The length of both DWNTs are 9.83nm and 9.8nm respectively. The simulation procedures for MD simulation in DWNTs are the same with those of SWNTs. Thermal interfacial resistance at 300K was examined and compared with thermal interfacial resistance with SWNTs.....	100
<b>Fig. 6.13</b>	Temperature profile of (a) (6,6)/(11,11) DWNT and (b) (10,0)/(19,0) DWNT with silicon at T=300K.....	101
<b>Fig. 6.14</b>	The cross section of (a) (5,5) CNT bundle inside silicon groove and (b) side view of (5,5) CNT bundle with silicon.....	103
<b>Fig. 6.15</b>	Thermal conductivity of SWNT, DWNT and CNT bundles All these results are calculated by Fourier law with MD simulation except (10,10) bundle, MWNT bundle and SWNT bundle.....	104
<b>Fig. 6.16</b>	Three interfaces of (a) two (11,11) CNTs, (b) silicon-silicon (0,0,1) surfaces and (c) (11,11) CNT-silicon (0,0,1) surfaces.....	105
<b>Fig. A.1</b>	sp hybridization of 2p <sub>x</sub> orbitals.....	109
<b>Fig. A.2</b>	Example of $\sigma$ and $\pi$ bands wavefunctions in HC $\equiv$ HC.....	110
<b>Fig. A.3</b>	Trans-polyacetylene, (HC $\equiv$ HC-) <sub>n</sub> with sp <sup>2</sup> hybridization.....	110
<b>Fig. A.4</b>	The unit cell of trans-polyacetylene bounded by a box defined with dotted lines.....	115
<b>Fig. A.5</b>	The energy dispersion relation E <sub>±</sub> (k) for polyacetylene [(CH) <sub>x</sub> ].....	116
<b>Fig. A.6</b>	The structure of graphite with graphene layers.....	117
<b>Fig. A.7</b>	(a) The unit cell and (b) the Brillouin zone of two dimensional graphite.....	118

<b>Fig. A.8</b>	The energy dispersion relations for 2D graphite in the whole region of the Brillouin zone.....	121
<b>Fig. A.9</b>	The condition for metallic energy bands.....	122

# CHAPTER ONE

## INTRODUCTION

Since they were discovered in 1991 [1], carbon nanotubes (CNTs) have attracted scientists' and engineers' interest due to its unique physical and electronic properties. The strong covalent carbon bonding provides good mechanical properties, such as high Young's modulus, strong stiffness, tension and bending strength. The electrical structure of a carbon nanotube is the same  $sp^2$  hybridization present in two dimensional graphite sheets. However, due to the periodicity along the circumferential direction on the lattice, the energy band can have certain amount of gap, which makes the system either metallic or semiconducting. Beside these interesting mechanical and electrical properties, carbon nanotubes have excellent thermal properties.

The thermal conductivity of carbon nanotubes [2] is greater than graphite and diamond. The thermal conductivities of diamond and graphite reach their maxima at low temperature (175K, 100K) [3,4]. Quite interestingly, the maximum of thermal conductivity of carbon nanotubes occurs above room temperature [2]. The high thermal conductivity and its monotonic increase up to room temperature make it attractive thermal management and thermal switch applications.

A thermal switch is designed to control heat flow between micro size heat engines by 'ON' and 'OFF' operations. In order to transfer heat energy across the thermal switch

during the ‘ON’ process, mercury droplets were used as heat transfer material [5]. However, the mercury droplet has a limitation in developing thermal devices due to its toxic properties. In order to develop the thermal switch without side effect and increases the efficiency of heat transfer during the ‘ON’ operation, vertically aligned carbon nanotubes (VACNT) were used as heat transfer material. However, the measured thermal interfacial resistance of VACNT was 20 times greater than that of mercury under the same experimental conditions.

The fact that carbon nanotubes exhibit their maximum thermal conductivities at or above room temperature whereas both diamond and graphite reach their maximum values well below room temperature (175K for diamond and 100K for graphite) [3,4], makes nanotubes very attractive for thermal management and thermal switch applications. The use of vertical arrays of MWNT as a thermal switch in a MEMS-based micro heat dynamic engine that generates electrical power by deforming piezoelectric membrane was investigated in [5]. The heat engines are cascaded to increase the output electrical power with thermal switches between successive stages. The expanded membrane of a given stage transmits heat energy to the next stage MEMS heat engine through the thermal switch, which turns on the engine. The use of arrays of vertically oriented multi-wall carbon nanotube (MWNT) and mercury droplets of same size were as heat transfer material in the thermal switch were investigated in [5]. The measured thermal contact resistance (TCR) with applied load of 0.1N of the vertical array of MWNT was 26 times larger than the TCR of mercury droplet even though the thermal conductivity of mercury (8.3 W/mK) is

considerably smaller than that of MWNT. CNTs were also investigated for possible use as thermal interface materials (TIM) because their significantly lower thermal resistance than air, can improve thermal transfer across solid interfaces where microscopic roughness can trap air pockets giving rise to limited contact area where heat transfer occurs. Also, the measured the thermal interfacial resistance under 0.445 MPa pressure between silicon substrate and CNT mat samples with (1) 60% of Ni-CNT coverage, (2) 90% of Fe-CNT coverage and (3) 80% of Fe-CNT coverage, were found to  $2.3 \times 10^{-5} \text{m}^2 \text{K/W}$ ,  $3.2 \times 10^{-5} \text{m}^2 \text{K/W}$ , and  $3.7 \times 10^{-5} \text{m}^2 \text{K/W}$ , respectively [6]. The measured thermal interfacial resistance of SWNT and MWNT in ranged from  $2.5$  to  $5.0 \times 10^{-4} \text{m}^2 \text{K/W}$  which is similar or higher than other commercial TIMs ( $\sim 2.0 \times 10^{-4} \text{m}^2 \text{K/W}$ ). Coating of raw carbon nanotube array with  $1 \mu\text{m}$  aluminum layer was also reported to reduce thermal contact resistance from  $1.52 \times 10^{-4} \text{m}^2 \text{K/W}$  to  $8.3 \times 10^{-5} \text{m}^2 \text{K/W}$  [7]. Baratunde et al used vertically oriented carbon nanotube arrays synthesized on both side of metal foil [8]. At the contact, both CNT and foil were deformed and it significantly increased the number of CNT contact spots on both sides of foil. This process results thermal interfacial resistance in less than  $1 \times 10^{-5} \text{m}^2 \text{K/W}$ . More recently, the effects of catalyst structure on the thermal interface resistances, quality and diameters of vertically oriented MWNT arrays grown on Ti/SiO<sub>2</sub>/Si substrate, were investigated in [9]. They also reported that the use of dendrimer to deliver the catalyst led to stronger anchoring of MWNT arrays to the substrate, which was responsible for lower measured ( $\leq 10^{-5} \text{m}^2 \text{K/W}$ ) thermal interface resistances even though they contained more defects and impurities. The measured thermal interfacial resistances are summarized in Table 1.1. When heat flows across different materials, the temperature

drop at the interface exists due to the thermal interfacial resistance [10]. At room temperature, the thermal interfacial resistance has been usually neglected since the energy carrier's mean free paths are quite small (~10-100nm) and the thermal resistance of bulk material is dominant.

Classical MD simulations has been used to investigate the effect chemical functionalization on the intrinsic SWNT thermal conductivity and the interfacial resistance of nanotubes surrounded by octane molecules [11,12]. In these MD simulations, a fraction of the octane molecules were covalently bonded to carbon atoms at random locations on the nanotube and the thermal interfacial resistance was found to decrease as the fraction of functionalized atoms increased. Furthermore, the thermal interfacial resistance between two (10,10) single wall nanotubes (SWNT) function of separation distance between CNTs was also calculated using MD simulations in [13]. The calculated thermal interfacial resistance exhibited a rapid increase with increase in separation distance due to the weak van der Waals interaction. On the other hand, fusing the two CNTs together via bonded interactions between CNTs resulted in significant decrease in the thermal interfacial resistance. The thermal interfacial resistance of SWNT was also studied for CNT bundle with MD simulation [14]. In their MD simulation, center CNT of the bundle was heated up 400K for 10ps, while other CNTs temperatures were 300K. The thermal interfacial resistance between center shell and others was measured as  $6.46 \times 10^{-8} \text{m}^2\text{K/W}$  by heat transfer between shells. MD simulations were also used to investigate the thermal interfacial resistance between two FCC crystals that interact via pair-wise Lennard-Jones (LJ) inter-atomic potential only in [15] for three different interface conditions: (1) mass

mismatch, (2) lattice mismatch and (3) alloyed interface. The MD simulation approach provides better estimates of thermal interfacial resistance compared to the diffuse mismatch model (DMM), because it accounts for both elastic and inelastic scattering at the interface where as DMM accounts for only elastic scattering. The thermal interfacial resistance between CNT and different materials (silicon and aluminum) was investigated in [16] using finite element method (FEM). However, FEM approach does not take into account the details of heat flow across the inter-atomic contact between two materials such as phonon scattering at the interface due to the diffuse mismatch, mass and lattice mismatch between CNT and other materials. The results of thermal interfacial resistance by MD simulation are summarized in Table 1.2

The molecular dynamics (MD) simulation can account for both elastic and inelastic scattering at the interface and showed better performance than diffuse mismatch model (DMM) in estimating thermal interfacial resistance [15]. Maruyama et al investigated the thermal interfacial resistance of CNT bundle. In their MD simulation, center CNT of the bundle was heated up 400K for 10ps, while other CNTs temperatures were 300K. The thermal interfacial resistance between center shell and others was measured as  $6.46 \times 10^{-8} \text{m}^2\text{K/W}$  by heat transfer between them [14]. Zhong et al calculated thermal interfacial resistance between two (10,10) single wall carbon nanotubes (SWNTs) as a function of different separation between CNTs [17]. When two CNTs were separated by  $3.5 \text{\AA}$ , the thermal interfacial resistance between two CNTs was  $\sim 8 \times 10^{-8} \text{m}^2\text{K/W}$ . These two approaches used the heat diffusion and heat conduction. The MD simulation modeling on the thermal interfacial resistance between CNT and other material such as silicon is not

reported yet and fundamental mechanism of thermal interfacial resistance of CNT is still open research area.

The goal of the research is to develop a MD simulation model for the thermal interfacial resistance between silicon and CNT. In order to model the heat flow from the CNT to the silicon substrate, models for MD simulation of silicon was developed with the Tersoff potential [18]. The thermal conductivity of silicon and its phonon modes were calculated and compared with standard values. The bonded interaction between carbon and silicon was examined by investigating thermal properties of silicon carbide using the Tersoff potential [18]. The armchair SWNT is placed on silicon (0,0,1) surface based on the stable configuration between two materials. At the interface, two different cases are investigated by two different Si-CNT interactions; (1) Lennard-Jones non-bonded van der Waals interaction and (2) bonded interaction as sum of Si-C bonded and non-bonded van der Waals interactions. For both cases, the temperature discontinuity (drop) at the interface was obtained and thermal interfacial resistance for each case is calculated as a function of temperature. To clarify the mechanism behind the heat energy transport across the interface, the phonon power spectrum for each interaction is calculated by the velocity auto-correlation function by Fourier transformation. In addition, the thermal interfacial resistance of zigzag SWNT, both armchair and zigzag DWNTs and (5,5) CNT bundle with silicon (0,0,1) surface were investigated with bonded interactions.

This thesis is organized into six chapters. Chapter 2 describes the thermal properties of carbon nanotubes with experimental and theoretical approaches. It also introduces the thermal switch, experimental results of thermal interface resistance and theoretical

approaches. A detailed explanation of MD simulation and energy minimization on the double wall carbon nanotubes can be found in chapter 3. The MD simulation modeling on the thermal properties and phonon distributions on the silicon and silicon carbide are discussed in Chapter 4. The silicon surface geometry and carbon nanotube adsorption on silicon (0,0,1) surface are also discussed in Chapter 4. Chapter 5 describes the methodology and results of heat pulse propagations in double wall carbon nanotube (DWNTs). In chapter 6, the thermal interfacial resistance of CNT (SWNT, DWNT and CNT bundle)-Si interface with three different interactions and detailed phonon analysis are provided.

Contact Material	Method	Results (m <sup>2</sup> K/W)	Ref
SWNT/MWNT	60% lower thermal resistance than bare Si-Cu interface, but higher than TIM	$5.0 \times 10^{-4}$	19
CNT Array	Mat type CNT array on Si substrate Thermal contact resistance between CNT and Cu.	$2.3 \times 10^{-5}$	6
CNT-Al coated	Coat CNT array tip with 1 $\mu$ m thick Al layer	$4.5 \times 10^{-4}$	7
CNT in TIM	Combination of CNT array with a phase change material (TIM)	$5.2 \times 10^{-6}$	20
CNT on metal foil	Synthesis vertically oriented CNT array on both sides of metal foil	$1 \times 10^{-5}$	8
MWNT arrays	Diameter distribution and quality of MWNT were varied by using Fe <sub>2</sub> O <sub>3</sub> nano-particles	$\leq 10^{-5}$	21
CNT array	Thermal resistance between 30 $\mu$ m wide vertically aligned CNT array and silicon substrate	$2 \times 10^{-5}$	22
Mercury droplet	Thermal resistance between 30 $\mu$ m diameter mercury droplets and silicon substrate	$1 \times 10^{-6}$	22
Silicon-silicon contact	Thermal resistance between two silicon wafer	$4.2 \times 10^{-4}$	23
Microfaze A6	Thermal interface material (TIM)	$2.1 \times 10^{-4}$	19
Omegatherm 201	Thermal interface material (TIM)	$2.0 \times 10^{-4}$	19

**Table 1.1** Measured thermal interfacial resistance of CNT, silicon, mercury droplet and TIMs.

Type	Method	Results (m <sup>2</sup> K/W)	Ref
(5,5) CNT bundle	Thermal interfacial resistance between center and surrounded CNTs	$6.46 \times 10^{-8}$	14
Two (10,10) SWNTs	Thermal interfacial resistance between two (10,10) SWNTs.	$8 \times 10^{-8}$ separation = 3.5 Å	13
CNT in octane liquid	Thermal interfacial resistance between CNT and liquid octane	$4 \times 10^{-8}$	24
CNT in octane liquid	Thermal interfacial resistance between CNT and liquid octane	$4.52 \times 10^{-8}$	25

**Table 1.2** The results of thermal interfacial resistance of CNT interface with MD simulations.

# CHAPTER TWO

## Carbon Nanotubes and Thermal Switch

### 2.1 Physical Structure of Carbon Nanotubes

The structure of a carbon nanotube is the cylindrical shape of a rolled 2D graphite sheet (see Fig. 2.1). The point O in Fig. 2.1 can be rolled into the point A which makes the graphene into the cylindrical shape. This process also brings the lattice site B into the other site B'. Therefore the vector OA and BB' are perpendicular to the tube axis. Depending on where point O position on the other position O-A, the diameter and chirality of nanotube are determined.

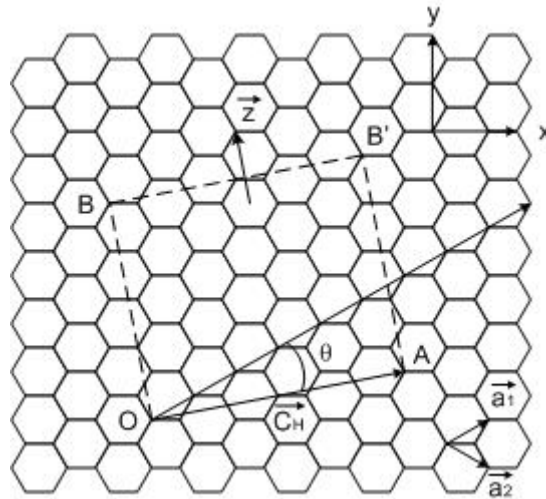


**Figure 2.1** The unrolled hexagonal lattice of a nanotube (from Ref 26).

Therefore, the vector OA defines the chiral vector  $\vec{C}_h$  and the vector OB' defines the

translational vector  $\vec{T}$ . The chiral vector can be expressed by the sum of unit vector of hexagonal lattice,  $\vec{a}_1$  and  $\vec{a}_2$  with multiplication integers, n and m:

$$\vec{C}_h = n\vec{a}_1 + m\vec{a}_2 \equiv (n, m) \quad (2.1)$$

The index pair (n,m) determines the chirality of the CNT. In the case of n=m, the shape of the cross section becomes cis-type as shown in Fig. 2.2 (a) and called armchair nanotube. In case of either index is zero, the shape of cross section becomes trans-type as shown in Fig. 2.2 (b) and called zigzag nanotube. In case of two index are different each other, the shape of cross section becomes the mixture of cis and trans and is called chiral nanotube.

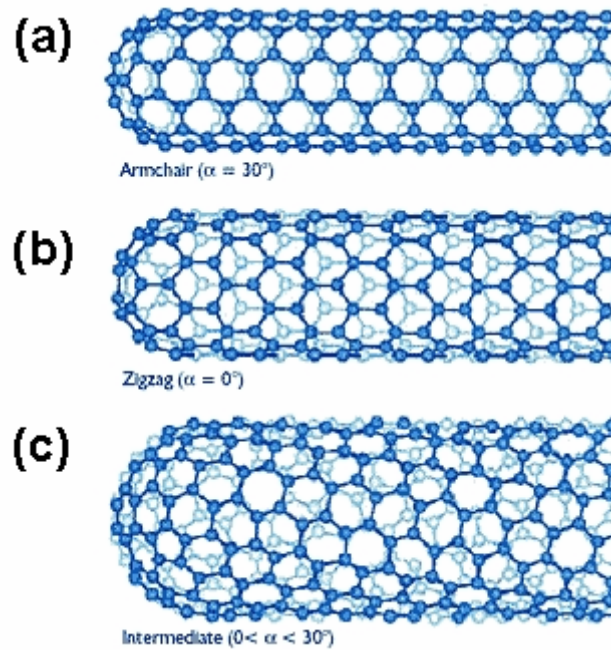


**Figure 2.2** The structure and cross sectional shape of (a)armchair, (b)zigzag and (c)chiral nanotubes [27]

Since the displacement of vector OA becomes the circumference (L) of nanotube, the magnitude of chiral vector  $\vec{C}_h$  can determine the diameter ( $d_i$ ) of the nanotube.

$$d_i = L / \pi \quad L = |\vec{C}_h| = \sqrt{\vec{C}_h \cdot \vec{C}_h} = a\sqrt{n^2 + m^2 + nm} \quad (2.2)$$

There is another geometry parameter which determines the chirality of a CNT. As shown in Fig. 2.1,  $\vec{C}_h$  defines a chiral angle  $\theta$  with the unit vector of hexagonal lattice,  $\vec{a}_1$ . From the inner product of  $\vec{C}_h$  and  $\vec{a}_1$ , the chiral angle  $\theta$  can be written as

$$\cos \theta = \frac{\vec{C}_h \cdot \vec{a}_1}{|\vec{C}_h| |\vec{a}_1|} = \frac{2n + m}{2\sqrt{n^2 + m^2 + nm}} \quad (2.3)$$

The range of angle  $\theta$  is  $0 \leq \theta \leq 30^\circ$  due to the symmetry of hexagonal symmetry of honeycomb lattice. The armchair CNT corresponds to  $\theta=30^\circ$  and zigzag CNT corresponds to  $\theta=0^\circ$ .

## 2.2 Thermal Properties of Carbon Nanotubes

Thermal conductivity is defined by heat flow rate across a material with temperature difference. In Fig. 2.3, a slab of cross-sectional area A and length L is placed between two heat sources,  $T_H$  and  $T_C$ , which ( $T_H > T_C$ ). The rate of heat flow, J is given by

$$H(=Q/t) = kA \frac{T_H - T_C}{L} \quad (2.4)$$

$k$  is called the thermal conductivity which has a unit [W/mK]. On the other hand, the thermal resistance  $T_R$  of a material of thickness  $L$  is defined by

$$T_R = \frac{L}{k} \quad (2.5)$$

which has a unit [m<sup>2</sup>K/W].

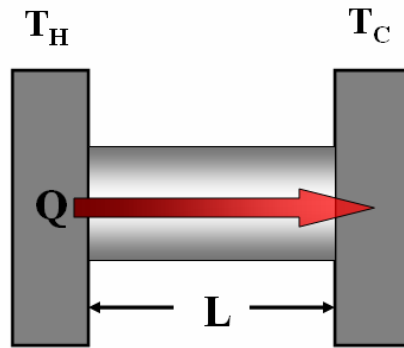


**Figure 2.3** Heat ( $Q$ ) flows from hot reservoir  $T_H$  to cold reservoir  $T_C$  through a material of cross-sectional area  $A$  and length  $L$ .

The carbon nanotubes exhibit thermal conductivities at room temperature that are higher than diamond and graphite. For example, some of the recent measurements of the

thermal conductivities of multiwall and single wall nanotubes reported values exceeding 3000 W/mK at room temperature, whereas measured thermal conductivities of diamond (including type II and thin films grown using chemical vapor deposition (CVD) process) range from 1300 to 2200 W/mK and that of graphite range from 1800 to 2000 W/mK [2,3,28]. However, the thermal conductivities of both diamond and graphite reach their maximum values well below room temperature (175K for diamond and 100K for graphite) [3,4] as shown in Fig. 2.4. On the other hand, the measured thermal conductivities of single wall nanotubes (SWNT) and multiwall carbon nanotubes (MWNT) exhibit a monotonic increase up to room temperature [2,29].

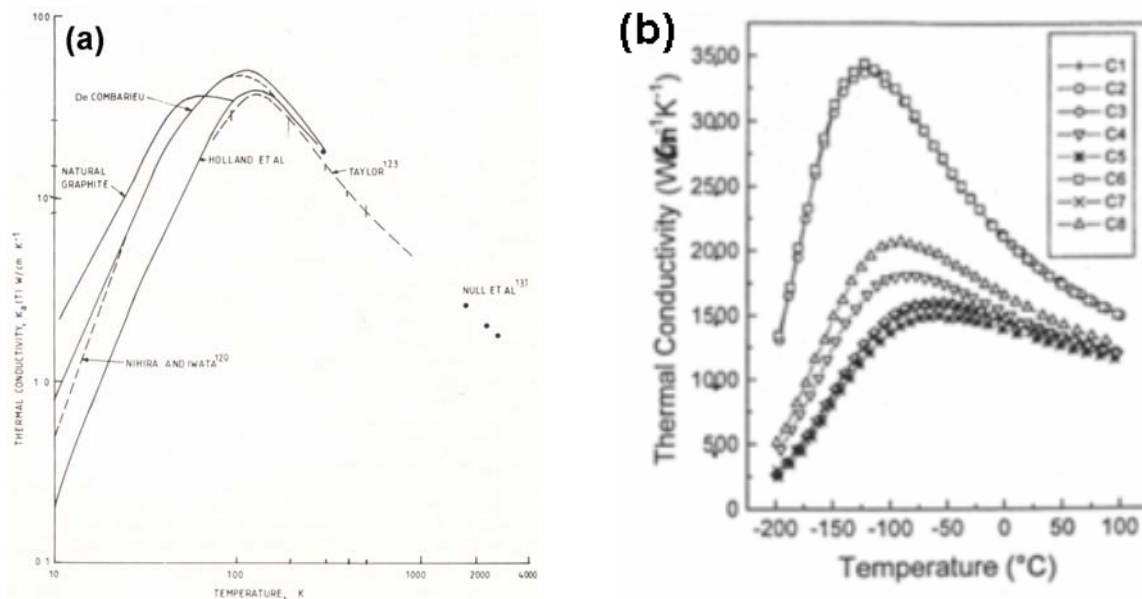


**Figure 2.4** Thermal conductivity of (a) graphite and (b) diamond [3,4]

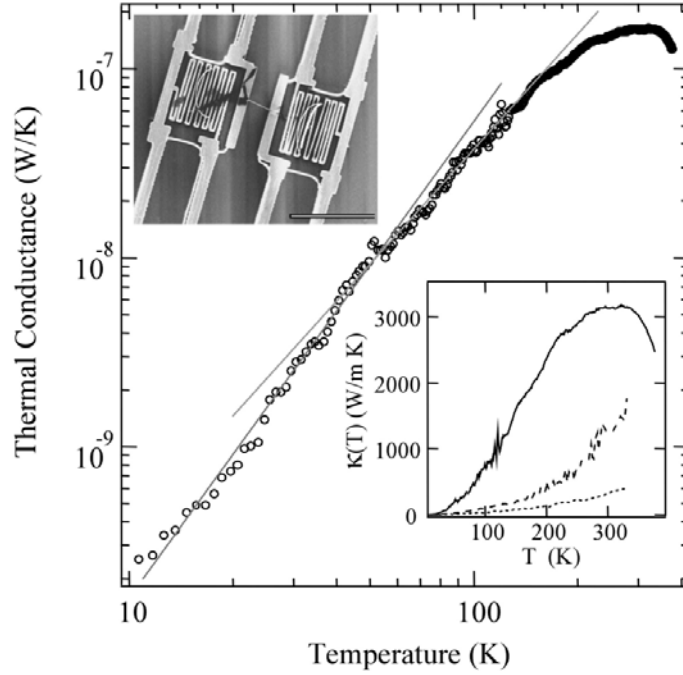


**Figure 2.5** Thermal conductivity of multi wall carbon nanotubes (MWNT) [2]

The example of monotonic thermal conductivity increase of multiwall carbon nanotubes is plotted in Fig. 2.5. In this result, the thermal conductivity starts to decrease beyond room temperature and it is attributed to defects and anharmonic phonon-phonon scattering (Umklapp process). For the phonon-phonon scattering, thermal resistance is caused by three-phonon processes

$$\vec{K}_1 + \vec{K}_2 = \vec{K}_3 + \vec{G} \quad (2.6)$$

where  $\vec{K}_1, \vec{K}_2, \vec{K}_3$  are the phonon wave vector and  $\vec{G}$  is the reciprocal lattice vector.

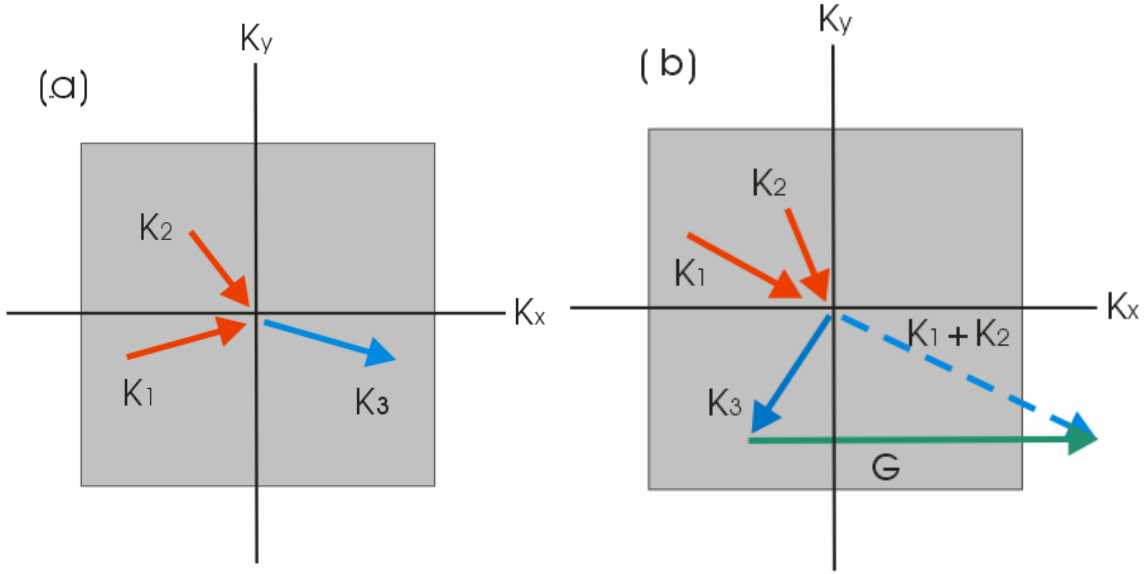


**Figure. 2.6** (a) the normal  $\vec{K}_1 + \vec{K}_2 = \vec{K}_3$  and (b) the Umklapp  $\vec{K}_1 + \vec{K}_2 = \vec{K}_3 + \vec{G}$  phonon collision process in a two-dimensional square lattice. The square in each figure represents the first Brillouin zone in the phonon  $\vec{K}$  space.

These processes are called Umklapp processes. The only meaningful phonon  $\vec{K}$ 's wavevectors lie in the first Brillouin zone, so that any longer  $\vec{K}$  produced in the collision must be brought into the first Brillouin zone by addition of a  $\vec{G}$  (see Fig. 2.6 (b)). On the other hand, when two phonon collision makes  $\vec{G}=0$  process, it is called normal or N processes as shown in Fig. 2.6 (a). If the temperature is higher than Debye temperature, all phonon modes are excited and at these high temperatures, most phonon collisions involve the Umklapp process. The on tube Debye temperature of carbon nanotube  $\theta_D$  is 960 while the transverse Debye temperature  $\theta_{\bar{D}}$  is 13K [30].

At high temperature regime, the lattice thermal resistivity is proportional to the temperature. Therefore, the mean free path is reduced at high temperature due to the Umklapp process and thermal conductivity of the system is decreased. Thermal conductivity,  $k$ , is given by:

$$k = \frac{1}{3}Cvl \quad (2.7)$$

where  $C$  is the heat capacity,  $v$  is the average particle speed and  $l$  is the mean free path. The onset of Umklapp processes occurs at low temperatures in graphite and diamond compared to nanotubes which exhibit a drop in thermal conductivity beyond room temperature. Recent theoretical investigation of relaxation through Umklapp processes in zigzag nanotubes have shown phonon mean free path length of the order of  $1 \mu\text{m}$  at  $300 \text{ K}$  [31].

The unique thermal properties of carbon nanotubes were measured by various research groups. Hone *et al.*[32] measured the thermal conductivity of SWCNT's mat and obtained a value of  $35 \text{ W/mK}$  at  $300\text{K}$ . Yi *et al.* reported the same order of magnitude for the bundles of MWNT's ( $25\text{W/mK}$ ) [33]. Hone *et al.* also measured the improved thermal conductivity of magnetically aligned SWNT film which exhibited  $200 \text{ W/mK}$  [34]. Motoo Fujii et al [35] used T-type nano-sensor device to measure thermal conductivity of single nanotube with  $9.8\text{nm}$  diameter and reported  $2000\text{W/mK}$  at room temperature. Recently, it was found that thermal conductivity of metallic SWCNT of length  $2.6\mu\text{m}$  and diameter  $1.7\text{nm}$  was  $3500\text{W/mK}$  at room temperature. [36].

A lowering of the thermal conductivity of individual multi-wall nanotubes with increased diameter to values lower than that of graphite was also reported in [2]. Investigations of the thermal conductivity of carbon nanotubes (CNT) using molecular dynamics (MD) simulation also report a wide range of thermal conductivities and show dependence on sample length [37,38,39,40,41]. These investigations used non-equilibrium molecular dynamics (NEMD) method based on Fourier law [37,38], NEMD using fictitious external forces [39], and equilibrium molecular dynamics (EMD) based on the Green-Kubo approach [40] to calculate the thermal conductivity of CNT.

By the NEMD method, thermal conductivity of armchair and zigzag SWNT were calculated as  $\sim 2000\text{W/mK}$  at 300K [37]. Since the mean free path of phonon in CNT is few micrometers, the size of CNT becomes important in MD simulation. For instance, it was reported that the thermal conductivity of CNT are affected by the length of CNT in NEMD method and it is called the finite-size effect. However, since heat source and sink are not used in Green-Kubo method, the finite-size effect is apparently much less severe than that for the direct method. As length of CNT increases,  $\kappa' \text{ (thermal conductance) } /L$  tends to a constant in Green-Kubo method.

Some research groups used the homogenous non-equilibrium Green-Kubo (HNEGK) molecular dynamics method. Berber et al [39] reported very high thermal conductivity ( $6600\text{W/mK}$ ) of (10,10) CNT at 300K with HNEGK. In their work, a fictitious force was applied, so that the system was not in equilibrium. Zhang et al [42] used same method and thermal conductivity of (11,11) at 300K was obtained to be  $\sim 3500\text{W/mK}$ .

### 2.3 Thermal Switch and Thermal Interfacial Resistance

As the size of device decreases to micro scale, it becomes also necessary to develop micro-size power source to operate the device. Cho et al reported developing a MEMS-based micro heat dynamic engine which consumes low temperature heat to do mechanical work and produce electrical power [5]. The heat engine is operated by a thermal switch, which controls heat transfer with ‘ON’ and ‘OFF’ operation (see Fig. 2.7). For the switch ‘OFF’ operation, high thermal resistance is required to prevent any heat leak through the thermal switch. The thermal resistance of ‘OFF’ operation is determined by the thermal properties of the empty gap between bottom and upper layers. However, at the switch ‘ON’ operation, the thermal resistance is minimum, to maximize the heat flow through the thermal switch. The thermal resistance of ‘ON’ operation is determined by the thermal properties of the contact material between layers.

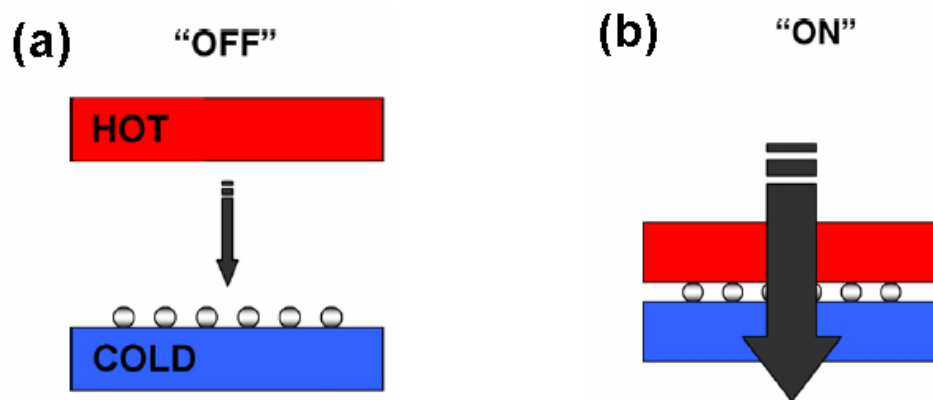


**Figure 2.7** The operation of thermal switch at (a) ‘OFF’ and (b) ‘ON’ [43]

During the thermal switch ‘ON’ state, the heat energy transfers into the heat engine and generates electrical power by deforming a piezoelectric membrane. The expanded membrane transmits heat energy to the other thermal switch to turn on the next stage engine. As heat transfer materials in thermal switch, mercury droplet and vertically aligned carbon nanotube (VACNT) were used. The mercury thermal switch was made of 40×40 grid of 1600 mercury droplets with 30- $\mu\text{m}$  diameter that was deposited via selective vapor decomposition (see Fig. 2.8), where as VACNT switch of same size array was prepared by chemical vapor deposition (CVD) (see Fig. 2.8). Both mercury droplet and VACNT thermal switches were fabricated on a silicon die.

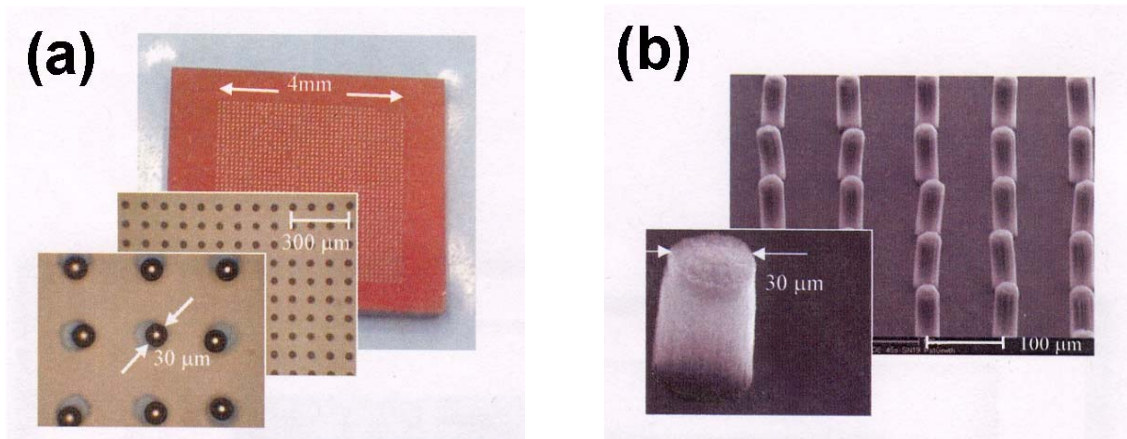


**Figure 2.8** (a) Liquid-metal micro droplets and (b) vertically aligned carbon nanotube arrays [5]

In order to examine the performance of thermal switch, three switch conductor materials were tested, (1) polished silicon surface, (2) Hg micro droplet and (3) VACNT. For the ‘OFF’ operation, three materials have the same thermal resistance as shown in Fig.

2.8 (a), since the thermal resistance of ‘OFF’ operation is characterized by the empty gap between silicon dies. The thermal resistance of ‘ON’ operation was measured with applied pressure which squeezes two silicon dies.

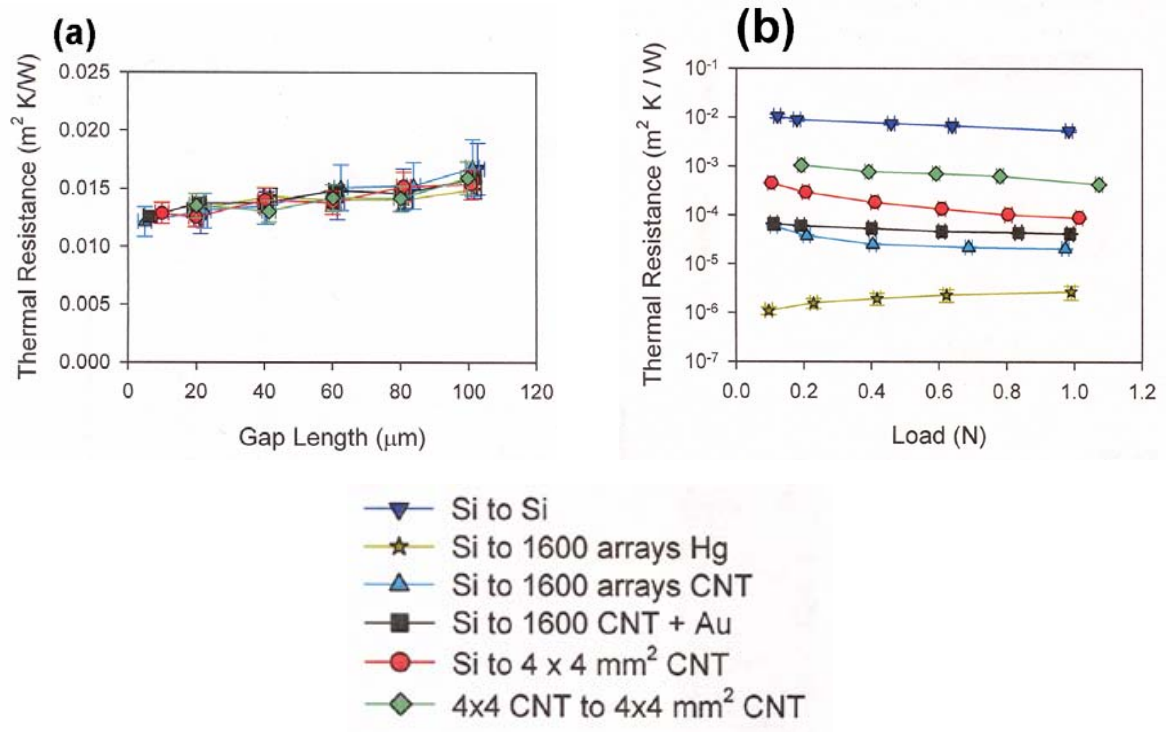


**Figure 2.9** The thermal resistance of bare silicon, VACNT and mercury droplets for the switch (a) ‘OFF’ and (b) ‘ON’ operation [22]

A lower thermal resistance was expected in VACNT because of its higher thermal conductivity compared to mercury (the measured thermal conductivity of MWNT bundle is ~25W/mK [33] vs 8.3W/mK for mercury). However, thermal contact resistance of Hg varies from  $4 \times 10^{-6}$  W/mK to  $1 \times 10^{-6}$  W/mK and that of VACNT varies  $8 \times 10^{-5}$  W/mK to  $2 \times 10^{-5}$  W/mK, as the applied load changes 0.1N to 1N, which results are shown in Fig. 2.9

(b). Roughly, therefore, thermal contact resistance of VACNT is 20 times greater than that of mercury droplets. The thermal contact resistance of two silicon dies was  $\sim 10^{-2}$  W/mK in the same range of applied load. The thermal contact ratio between ‘ON’ and ‘OFF’ state,  $R_{\text{off}}/R_{\text{on}}$  for mercury droplets, VACNT and silicon dies are 168, 6.8, and 3.4 respectively. Since it is required high thermal contact ratio between ‘ON’ and ‘OFF’, mercury droplets show the best performance, but CNT is only two times better than the bare silicon contact.

In general, thermal interfacial resistance exists due to the imperfections between contact surfaces. In order to minimize this problem, the thermal interfacial material (TIM) is applied at the contact surface. Most TIMs can be categorized in four groups, solder, thermal paste, phase change material and sheet-type material. Thermal interfacial resistance of these TIMs is approximately  $5 \times 10^{-6} \text{m}^2\text{K/W}$  [44]. The thermal interfacial resistance of carbon nanotube was measured and compared with the TIMs by few research groups. Jun et al measured the thermal interfacial resistance of mat type of carbon nanotube on the silicon substrate with copper contact. [44]. The surface of silicon was prepared with three different materials, (1) 60% of Ni-CNT coverage, (2) 90% of Fe-CNT coverage and (3) 80% of Fe-CNT coverage. The thermal interfacial resistance decreased with the applied pressure and at a pressure of 0.445 MPa, and the resistances of the three samples were  $2.3 \times 10^{-5} \text{m}^2\text{K/W}$ ,  $3.2 \times 10^{-5} \text{m}^2\text{K/W}$ , and  $3.7 \times 10^{-5} \text{m}^2\text{K/W}$  respectively. These values are higher than average thermal interfacial resistance of TIMs. Chuang et al also compared the thermal interfacial resistance of CNT with commercial TIMs. They found that the measured thermal interfacial resistance of SWNT and MWNT were  $2.5 \sim 5.0 \times 10^{-4} \text{m}^2\text{K/W}$  which is

similar or higher than other commercial TIMs [45]. Jun et al reported improved results of thermal interfacial resistance. They also reported improved results of the thermal interfacial resistance between copper and an undoped silicon wafer with carbon nanotubes, a phase change materials (PCMs) and indium (In) sheet as interfacial layers [46]. Compared to the Cu-In-Si interface, the addition of the CNT array (Cu-In-CNT-Si) slightly reduced the resistance. However, the addition of the CNT array to the PCM combination (Cu-PCM-CNT-Si) greatly reduced the PCM-CNT array composite's thermal interfacial resistance compared to the Cu-PCM-Si composites. Under a pressure of 0.35MPa, the PCM-CNT array combination produced the minimum thermal interfacial resistance of  $5.2 \times 10^{-6} \text{m}^2\text{K/W}$  while the resistance of Cu-PCN-Si composites reached  $\sim 1.5 \times 10^{-5} \text{m}^2\text{K/W}$ . As a different approach to enhance thermal conductance at CNT interface, Wu et al coated raw carbon nanotube array (CAN) with 1  $\mu\text{m}$  aluminum layer and succeeded in decreasing thermal contact resistance by 50% ( $1.52 \times 10^{-4} \text{m}^2\text{K/W}$  to  $0.83 \times 10^{-4} \text{m}^2\text{K/W}$ ) [7]. However, the analytical and numerical approaches to examine the high thermal interfacial resistance of CNT are not fully investigated and are currently an active research area.

In general, the investigating of heat transfer between two different materials is a very challenging issue. When heat flows across different materials, a temperature drop at the interface exists due to the thermal interfacial resistance [47]. At room temperature, the thermal interfacial resistance has been usually ignored since the energy carrier's mean free paths are quite small ( $\sim 10\text{-}100\text{nm}$ ) and the thermal resistance of bulk material is dominant. However, recently as the size of devices decreased to nano scale, the thermal interfacial

resistance becomes the major thermal resistance at room temperature. Theoretically, Baowen et al studied the thermal interfacial resistance between two anharmonic lattices [48]. It was reported that the phonon band gap between two systems decreased as the temperature increased. When the temperature surpassed a certain value, the gap disappears and the two phonon modes overlap each other. Ravi et al studied microscopic and macroscopic thermal contact resistance of pressed mechanical contact between silicon and copper [49]. They used the diffuse mismatch model (DMM) and unified contact heat transfer model to discuss the real surface contact of silicon-copper. Since the thermal properties of copper are determined by both the phonon and the electron behavior, they also applied the compensation of thermal interfacial resistance due to the electron. The measured thermal interfacial resistance of silicon-copper decreased as the temperature increased and the theoretical results of the thermal interfacial resistance shows the same behavior.

Robert et al [50] used MD simulation to investigate the thermal interfacial resistance between two FCC crystals interacting with the pair-wise Lennard-Jones (LJ) interatomic potential. They investigated three different interface cases, mass mismatch, lattice mismatch and alloyed interfaces and compared MD results with the diffuse mismatch model (DMM). At the low temperature, the heat transport at the interface is determined by the elastic scattering, whereas both elastic and inelastic scattering contribute at high temperature. Since the MD simulation accounts for both scattering types, whereas DMM accounts only for elastic scattering, DMM underpredicts thermal interfacial conductivity at

high temperature. MD simulation provided a factor of two or more increase at higher temperature. The theoretical limitation of DMM and acoustic mismatch model (AMM) was also reported by experimental approach [51]. Swartz et al measured the solid (metal)-solid (dielectric substrate) thermal interfacial resistance and compared the measured results with theoretical predictions by AMM and DMM. Both measured and theoretical expectations were well matched at low temperature. However, the measured and expected values diverged from each other above 30K.

Maruyama et al calculated using MD simulations, the thermal interfacial resistance between center shell and the surrounding 6 shells in (5,5) CNT bundles [14]. In their MD simulation, the whole CNT bundle was held at 300K for 100ps and then only the center CNT was heated up to 400K for 10ps. The thermal interfacial resistance was calculated as  $6.46 \times 10^{-8} \text{ m}^2\text{K/W}$  by the heat diffusion between center and surrounding shells. The thermal interfacial resistance between two (10,10) single wall nanotubes (SWNT) was calculated as a function of separation distance between CNTs in [52]. The MD simulation configuration for their work is plotted in Fig. 2.10 (a). To stabilize the two CNTs, they fixed CNT ends. The thermal interfacial resistance rapidly increased as separation distance increased due to the weak van der Waals interaction as shown in Fig. 2.10 (b). However, when two CNTs were close enough to allow bonding, the thermal interfacial resistance decreased dramatically due to the bonded interactions between CNTs. The MD simulation was performed by the heat conduction between hot slab (cold slab) and the rest of CNT.

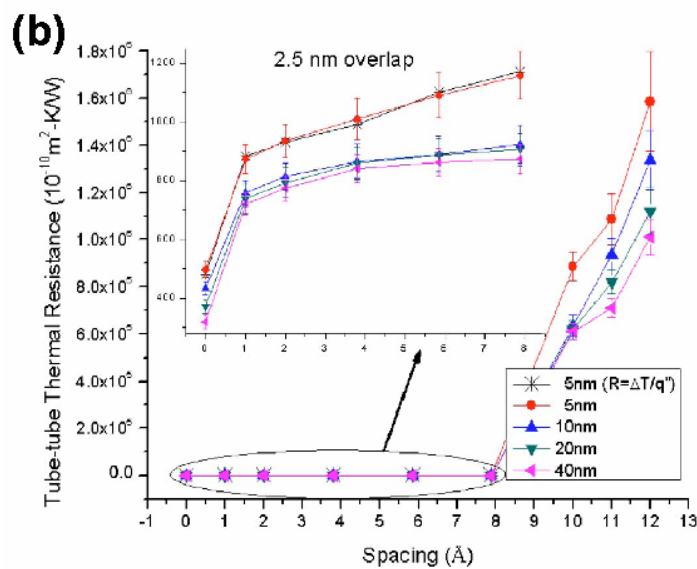
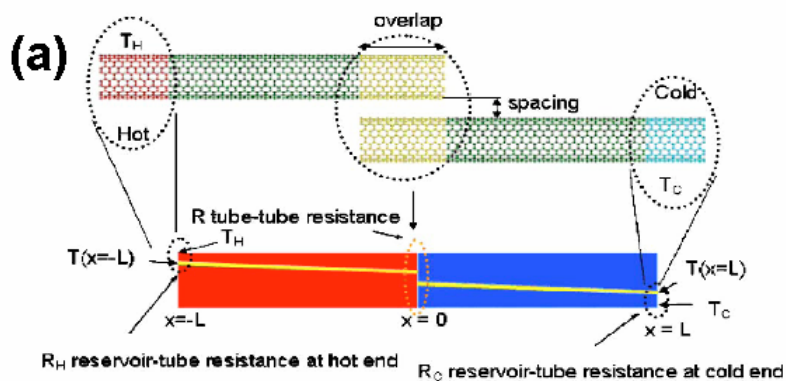


**Figure 2.10** (a) MD simulation configuration for thermal interfacial resistance between two (10,10) CNT and (b) the results of thermal interfacial resistance as a function of separation distance and the length of CNTs. The overlap length between CNTs was 2.5nm. [13]

Mahajan et al used finite element method (FEM) to study thermal interfacial resistance between CNT and different materials (silicon and aluminum) [53]. Since FEM was applied to their research, the details of heat flow due to the interatomic contact between

two materials were eliminated and therefore several microscopic heat flow phenomena at the interface were not taken into account. For example, the effect of phonon scattering at the interface due to the diffuse mismatch was not included and the effect of mass and lattice mismatch between CNT and silicon, aluminum were also ignored. MD simulation can account for these effects, however, the interface thermal resistance between CNT and other solids with MD simulation approach is very active research area.

# **CHAPTER THREE**

## **MOLECULAR DYNAMICS**

### **3.1 Introduction**

The first MD calculation was performed in the 1960s [54]. The MD theory and algorithm have developed with the dramatic advance of computer processing ability. Classical MD simulation makes use of Newtonian mechanics to determine the behavior of system. The classical forces acting on each atom are determined by the inter-atomic potential. Each atom's positions and velocities are predicted by numerical predictor-corrector methods and Taylor series expansions. Compared to the MD method, the quantum mechanical approach for the N-body problem is extremely difficult with the theoretical limitation of quantum mechanics itself. In addition, a majority of behavior in various states can still be understood by a non-quantum mechanical (classical) approach. Compared to the experiment, the MD simulation provides very high time and space resolutions of the structure, fluctuation, etc. which are not available by the experiment. From these merits of MD method, various MD algorithms were developed for the study of mechanical and thermal properties of CNT.

### **3.2 General Method**

Molecular Dynamics (MD) Simulation is a classical approach to modeling systems

of atoms and molecules, which uses Newton's laws of motion and an accurate interatomic potential. For a given interatomic potential,  $U$ , the force between two particles due to the potential,  $U$  is given by

$$\vec{F}_{ij} = -\nabla U_{ij} \quad (3.1)$$

where  $i$  and  $j$  are  $i$ th and  $j$ th atoms in the  $N$  particles system. The total force which acts on  $i$ th particle from the system is

$$\vec{F}_{ij} = -\sum_{j \neq i} \nabla U_{ij} \quad (3.2)$$

In MD modeling, it is not necessary to calculate all force pairs between  $i$ th particle and  $j$ th particle (where  $j=1, \dots, N$  except  $i$ ). Instead, a neighbor list of interaction atoms pairs is prepared and the interatomic potential calculation covers only pairs of atoms in the neighbor list. The neighbor list is determined by the cut off distance between two particles and cut off distance is different from atomic number and used interatomic potential.

The MD simulation calculates the change of the system in small times step,  $\Delta t$ . At each time step, the components of position and velocity are calculated. For the numerical integration, a Taylor series expansion is used to predict the position, velocity, acceleration as given in equation (3.3)~(3.6). The predicted values are calculated from the present time step with higher-order terms of each atom.

$$r(t + \Delta t) = r(t) + \dot{r}(t) \cdot \Delta t + \frac{1}{2!} \ddot{r}(t) \cdot \Delta t^2 + \frac{1}{3!} \dddot{r}(t) \cdot \Delta t^3 \quad (3.3)$$

$$\dot{r}(t + \Delta t) = \dot{r}(t) + \ddot{r}(t) \cdot \Delta t + \frac{1}{2!} \dddot{r}(t) \cdot \Delta t^2 \quad (3.4)$$

$$\ddot{r}(t + \Delta t) = \ddot{r}(t) + \dddot{r}(t) \cdot \Delta t \quad (3.5)$$

$$\dddot{r}(t + \Delta t) = \dddot{r}(t) \quad (3.6)$$

The calculation of above Taylor series give the velocity ( $\dot{r}(t)$ ), which is the time-derivative of the position  $r(t)$ , the acceleration ( $\ddot{r}(t)$ ) which is the second time-derivative of the position, and the third time-derivative of the position ( $\dddot{r}(t)$ ). Once the position, velocity, acceleration, and the third time-derivative of the position have been predicted for the next time step, they are used to calculate the physical properties of the system at that time step, such as temperature and energy. However, since the Taylor series is infinite series, there can be numerical error between right and left side of equation (3.3)~(3.6) due to the truncation of the series after the third-order term. As simulation time goes on, small numerical error between right and left terms can produce large deviation from the proper results. In order to correct the numerical error in predicted values, we use the Nordsieck predictor and corrector method.

### 3.3 The Nordsieck-Gear Predictor-Corrector Method

This scheme makes its predictions based on a slightly modified form of equations 3.3~3.6):

$$r(t + \Delta t) = r(t) + \dot{r}(t) \cdot \Delta t + \frac{1}{2!} \ddot{r}(t) \cdot \Delta t^2 + \frac{1}{3!} \dddot{r}(t) \cdot \Delta t^3 \quad (3.7)$$

$$\dot{r}(t + \Delta t) \cdot \Delta t = \dot{r}(t) \cdot \Delta t + \ddot{r}(t) \cdot (\Delta t)^2 + \frac{1}{2!} \dddot{r}(t) \cdot \Delta t^3 \quad (3.8)$$

$$\ddot{r}(t + \Delta t) \cdot \frac{(\Delta t)^2}{2!} = \ddot{r}(t) \cdot \frac{(\Delta t)^2}{2!} + \dddot{r}(t) \cdot \frac{(\Delta t)^3}{2!} \quad (3.9)$$

$$\dddot{r}(t + \Delta t) \cdot \frac{(\Delta t)^3}{3!} = \dddot{r}(t) \cdot \frac{(\Delta t)^3}{3!} \quad (3.10)$$

Based on these equations, the vector  $z(t)$  and the matrix  $A$  are defined as following

$$z(t) = \begin{pmatrix} r(t) \\ \dot{r}(t) \cdot \Delta t \\ \ddot{r}(t) \cdot \frac{(\Delta t)^2}{2!} \\ \dddot{r}(t) \cdot \frac{(\Delta t)^3}{3!} \end{pmatrix} \quad \text{and} \quad A = \begin{pmatrix} 1 & 1 & 1 & 1 \\ 0 & 1 & 2 & 3 \\ 0 & 0 & 1 & 3 \\ 0 & 0 & 0 & 1 \end{pmatrix} \quad (3.11)$$

Thus, the prediction consists of the matrix equation  $z^P(t + \Delta t) = A \cdot z(t)$ . The superscript  $P$  indicates that the values are the predicted values.

For correction, the Nordsieck formulation makes a comparison between the acceleration calculated in equation (3.4),  $\ddot{r}(t + \Delta t)$ , and that calculated from the interatomic potential in equation (3.1),  $a(t + \Delta t)$ . Then, the error can be defined as

$$e(t) = [a(t + \Delta t) - \ddot{r}(t + \Delta t)] \frac{(\Delta t)^2}{2!}. \quad \text{To correct this error, the results of equations (3.6)-(3.9)}$$

are scaled by a value proportional to the error in the acceleration, such that

$$z(t + \Delta t) = z^P(t + \Delta t) + e(t) \cdot \begin{bmatrix} 1/6 \\ 5/6 \\ 1 \\ 1/3 \end{bmatrix} \quad (3.12)$$

### 3.4 Tersoff Potential and Tersoff-Brenner Potential

As it described above, MD simulation needs to use precise interatomic potential to predict exact values. The interface system consists of silicon and a carbon nanotube. Therefore, we need to apply the interatomic potential for (1) bulk silicon, (2) carbon nanotube and (3) silicon-carbon bonded interaction at the interface. Tersoff developed the interatomic potential for the covalent bonded atoms, such as silicon, carbon and germanium [55] and interatomic potential for the multicomponents systems [18]. In 1990, Tersoff updated Tersoff parameters [56].

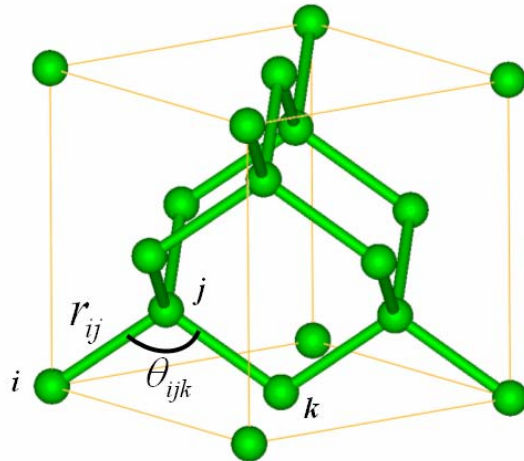


**Figure 3.1** The lattice structure of silicon, which is diamond crystal lattice.

The total energy of the system is expressed the sum of interatomic potentials as given by:

$$E = \sum_i E_i = \frac{1}{2} \sum_{i \neq j} V_{ij} \quad , \quad V_{ij} = f_C(r_{ij}) [f_R(r_{ij}) + b_{ij} f_A(r_{ij})] \quad (3.13)$$

where E is the total energy of the system, i, j, and k label the atoms of the system and  $r_{ij}$  is the length of the ij bond (see Fig. 3.1). In equation (3.13)  $f_R$  represents repulsive force,  $f_A$  represents the attractive force and  $f_C$  indicates the cutoff term which is used to build the neighbor list in calculating forces. In detail, attractive and repulsive forces have exponential forms such as

$$f_R = A_{ij} \exp(-\lambda_{ij} r_{ij}), \quad f_A = -B_{ij} \exp(-\mu_{ij} r_{ij}) \quad (3.14)$$

while the cut off term,  $f_C$  has geometry limit depends on the distance between two particles.

$$f_C(r_{ij}) = \begin{cases} 1, & r_{ij} < R_{ij} \\ \frac{1}{2} + \frac{1}{2} \cos\left[\frac{\pi(r_{ij} - R_{ij})}{S_{ij} - R_{ij}}\right], & R_{ij} < r_{ij} < S_{ij} \\ 0, & r_{ij} > S_{ij} \end{cases} \quad (3.15)$$

The coefficient,  $b_{ij}$  is determined as a function of Tersoff parameters, cut off term and a function of bonding angle,  $g(\theta_{ijk})$ .

$$b_{ij} = \chi_{ij} (1 + \beta_i^{n_i} \zeta_{ij}^{n_i})^{-\frac{1}{2n_i}}, \quad \zeta_{ij} = \sum_{k \neq i, j} f_C(r_{ij}) \omega_{ik} g(\theta_{ijk}) \quad (3.16)$$

The function  $g(\theta_{ijk})$  is determined by Tersoff parameters (Table 3.1) and the bond angle between ij and ik as shown in Fig. 3.1.

$$g(\theta_{ijk}) = 1 + \frac{c_i^2}{d_i^2} - \frac{c_i^2}{[d_i^2 + (h_i - \cos \theta_{ijk})^2]} \quad (3.17)$$

Some of Tersoff parameters are calculated with the mixture equations as given below:

$$\lambda_{ij} = \frac{\lambda_i + \lambda_j}{2}, \quad \mu_{ij} = \frac{\mu_i + \mu_j}{2} \quad (3.18)$$

$$A_{ij} = (A_i A_j)^{\frac{1}{2}}, \quad B_{ij} = (B_i B_j)^{\frac{1}{2}} \quad (3.19)$$

$$R_{ij} = (R_i R_j)^{\frac{1}{2}}, \quad S_{ij} = (S_i S_j)^{\frac{1}{2}} \quad (3.20)$$

while i and j indicate the ith and jth atoms, either can be the same or different atoms.

The MD simulation of bulk silicon uses the Tersoff potential with the Tersoff parameters of silicon. The bonded interaction between carbon and silicon is performed by the Tersoff potential and Tersoff parameters of Si-C which were prepared by the mixture relation (equations 3.18~3.20).

Brenner found some inherent problems when the Tersoff potential was applied to certain double-bonding situations in carbon [57]. Therefore, he added an adjustment to the

bond-order terms to correct those problems. The combination of Tersoff's bond-order potential and Brenner's subsequent adjustment for carbon is known as the Tersoff-Brenner interatomic potential. For the interatomic potential of carbon nanotube, The Tersoff-Brenner interatomic potential is used.

	<b>Carbon</b>	<b>Silicon</b>
A	$1.3936 \times 10^3$	$1.8308 \times 10^3$
B	$3.467 \times 10^2$	$4.7118 \times 10^2$
$\lambda$	3.4879	2.4799
$\mu$	2.2119	1.7322
$\beta$	$1.5724 \times 10^{-7}$	$1.1000 \times 10^{-6}$
n	$7.2751 \times 10^{-1}$	$7.8434 \times 10^{-1}$
c	$3.84049 \times 10^4$	$1.0039 \times 10^5$
d	$4.384 \times 10^0$	$1.6217 \times 10^1$
h	$-5.7058 \times 10^{-1}$	$-5.9825 \times 10^{-1}$
R	1.8	2.7
S	2.1	3.0
$\chi_{C-Si}$	0.9776	

**Table 3.1** The Tersoff parameters for the carbon and silicon

### 3.5 The Lennard-Jones (LJ) Potential

Besides the interatomic pair potential for covalent bonding, the non-bonded interaction is also necessary to perform precise MD simulation. For example, the 6-12 Lennard-Jones (LJ) type van der Waals interaction is applied to the non-bonded interaction between nanotube shells in multi wall carbon nanotubes.

$$U_{vdW} = \sum_{\text{non-bonded pairs}} 4\varepsilon_{ij} \left[ \left( \frac{\sigma_{ij}}{r_{ij}} \right)^{12} - \left( \frac{\sigma_{ij}}{r_{ij}} \right)^6 \right] \quad (3.21)$$

where  $r_{ij}=|r_i-r_j|$  is the separation between two atoms,  $i$  and  $j$  in the different shells,  $\varepsilon_{ij}$  is the potential well depth,  $\sigma_{ij}$  is the van der Waals separation distance. In the case of non-bonded interaction between silicon and carbon at the CNT-Si interface, LJ parameters are determined by the Lorentz-Berthelot rules, which is given by

$$\begin{aligned} \sigma_{ij} &= \frac{\sigma_i + \sigma_j}{2} \\ \varepsilon_{ab} &= \sqrt{\varepsilon_i \varepsilon_j} \end{aligned} \quad (3.22)$$

In calculating non-bonded interaction, the neighbor list is also built up with cut off distance of each material.

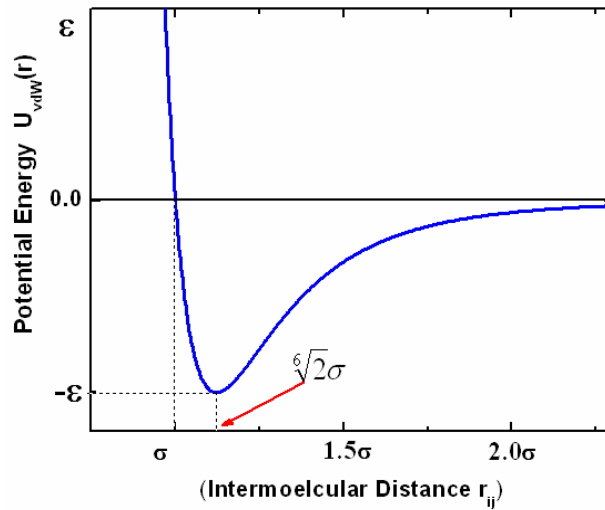


**Figure 3.2** Lennard-Jones 12-6 potential

The equilibrium distance of Lennard-Jones potential is given by  $\partial U_{vdW} / \partial r = 0$  which results in  $\sqrt[6]{2}\sigma$ , where the energy has minimum value,  $-\epsilon$ . Graphically, it is plotted in Fig. 3.2.

### 3.6 Calculating Physical Properties From the MD Simulations

From the MD simulation modeling, the positions and the velocities of atoms in the system at the desired time steps are obtained. From this information, thermal properties of the system can be calculated. The total energy of the N atoms system is the sum of individual atom's kinetic energy, namely

$$E_{system} = \sum_{i=1}^N \frac{1}{2} m_i v_i^2 \quad (3.33)$$

The average kinetic energy of the system is obtained by dividing total kinetic energy by the total number of atoms in the system,

$$E_{avg} = \frac{1}{N} \sum_{i=1}^N \frac{1}{2} m_i v_i^2 \quad (3.34)$$

From the law of equipartition, the temperature of the system is proportional to the average kinetic energy. In three dimensions, the temperature of the system can be given by the following relation,

$$E_{avg} = \frac{3}{2} k_B T \quad (3.35)$$

where  $k_B$  is the Boltzmann's constant and  $T$  is the temperature of the system.

From the information of temperature, it is possible to increase or decrease temperature of specific regions of the system. Once temperature in one region of system increases and that of the other part decreases, heat energy flows from hot to cold regions and it generates temperature gradient. This method is analogous to the experimental setup to calculate the thermal conductivity of the system. This method is called the Fourier method. The Fourier method is also known as the direct method or nonequilibrium molecular dynamics method (NEMD).

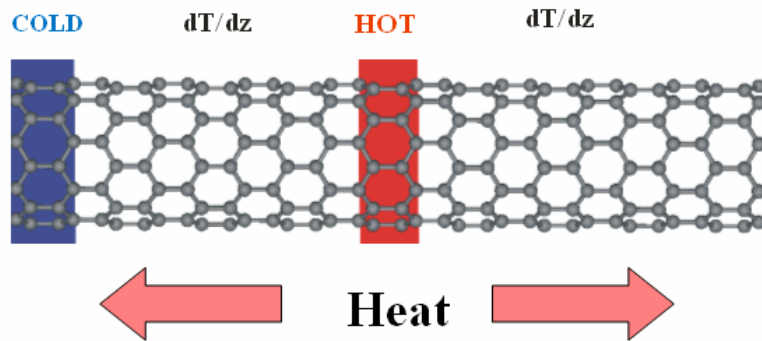


**Figure 3.3** The configuration of Fourier method

In details, heat  $\Delta\epsilon$  is added in a thin slab (hot slab) and removed from different slab (cold slab) of same size by rescaling particles velocities at each time step using

$$v_{i,new} = v_{i,old} \cdot \sqrt{\frac{T_{control}}{T_{current}}} \quad (3.36)$$

$$\kappa = -\frac{1}{A} \cdot \frac{dQ/dt}{dT/dz} \quad (3.37)$$

where  $T_{\text{current}}$  is the current temperature and  $T_{\text{control}}$  is desired temperature of the hot and cold slabs,  $v_{\text{old}}$  is the current velocity and  $v_{\text{new}}$  is updated velocity of particles in the slab. When the system achieves steady state, the heat current is given by  $Q = \Delta \varepsilon / 2A \Delta t$  ( $\Delta t$  is time step,  $A$  is cross section area). The temperature gradient ( $dT/dz$ ) is then calculated and Fourier law is used to obtain thermal conductivity, equation 3.37. In NEMD method, it is very important to achieve a steady state current flow. It usually takes a very long simulation time to obtain a smooth temperature profile under steady-state current flow.

### 3.8 Energy Minimization of Multiwall Carbon Nanotubes (MWNTs)

In order to understand the effect of CNT shells in heat pulse propagations (Chapter 5), two double wall carbon nanotubes (DWNTs), (5,5)/(10,10) and (9,0)/(18,0) were used for heat pulse propagation simulations. The structures of DWNTs are plotted in Fig. 3.4

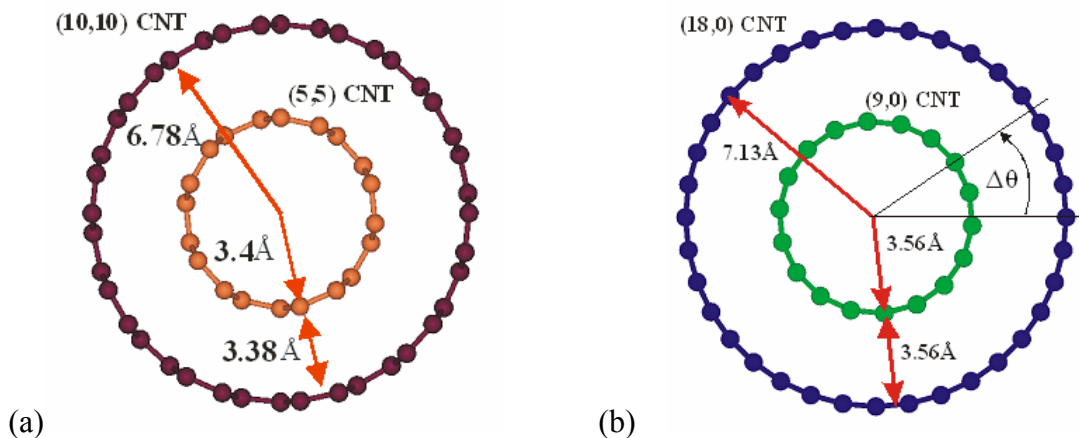


**Figure 3.4** The structure looking of (a) armchair and (b) zigzag DWCNTs

The initial coordinates of DWNTs were generated with arbitrary relative orientation

between shells. Therefore, in general, the initial structure does not have minimum energy. In order to stabilize the DWNTs structures, energy minimization was performed before the MD simulations (heat pulse propagation, thermal conductivity and thermal interfacial resistance) of DWNTs start. The energy minimization is performed for both rotational and lateral directions. For both displacements, temperature of the system quenched to 0K, which makes the system depend on only the potential energy. For rotational displacement, the inner shell was rotated with small angle with respect to outer shell. The angular energy minimizations of (5,5)/(10,10) and (9,0)/(18,0) DWNT are plotted in Fig. 3.5. For the lateral displacement, the inner shell shifted along the z-axis with small displacement and the result is shown in Fig. 3.5.

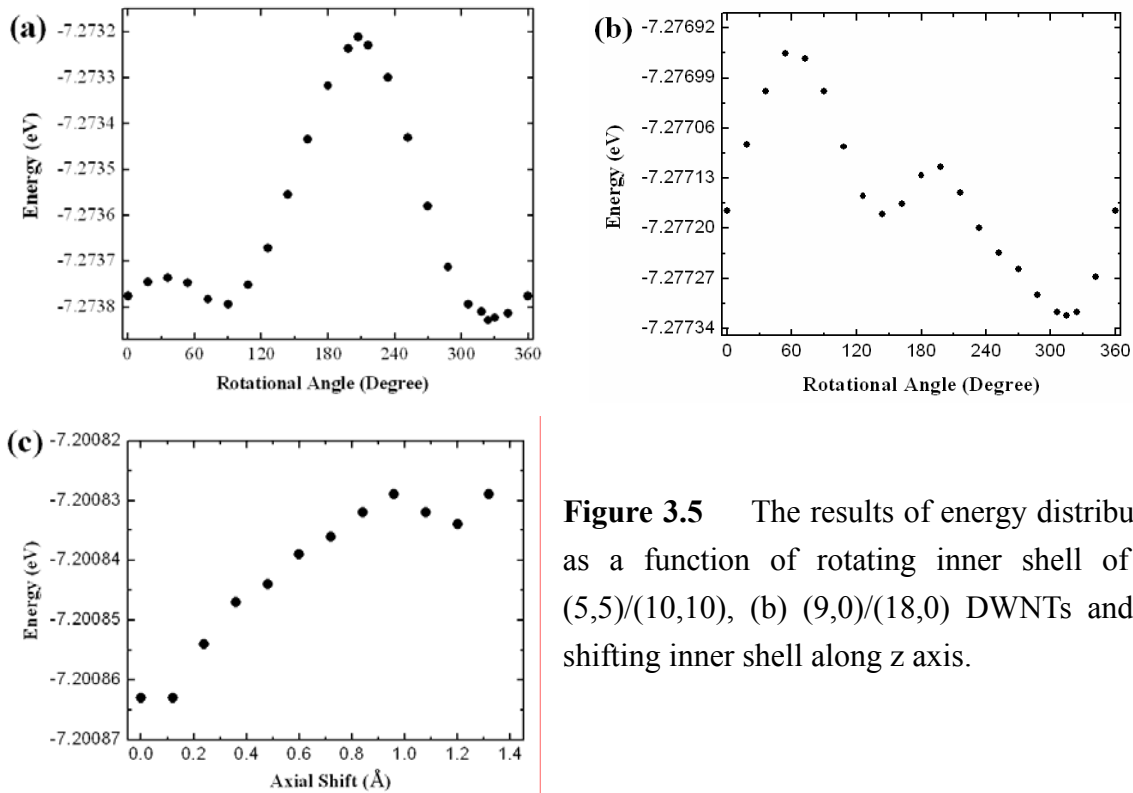


**Figure 3.5** The results of energy distribution as a function of rotating inner shell of (a) (5,5)/(10,10), (b) (9,0)/(18,0) DWNTs and (c) shifting inner shell along z axis.

# **CHAPTER FOUR**

## **MOLECULAR DYNAMICS MODEL FOR SILICON-CARBON NANOTUBES INTERFACE**

### **4.1 Introduction**

The final goal of this project is to develop the MD simulation model of CNT silicon interface to study the thermal interfacial resistance. In order to achieve this goal, it is necessary to develop MD modeling for bulk silicon and silicon-carbon bonding. For this purpose, the Tersoff potential for multi-components systems was chosen for silicon-silicon bonding and silicon-carbon bonding. In order to examine the developed MD modeling, thermal conductivity and phonon spectrum of silicon were calculated and compared with measured values. For the silicon-carbon interaction, thermal conductivity of  $\beta$ SiC was calculated. In addition, the geometry of reconstructed silicon (0,0,1) surface, the absorption of CNT on the silicon surface are discussed.

### **4.2 Bulk Silicon**

Silicon is the 14<sup>th</sup> element in the periodic table. Silicon crystallizes in the same structure as diamond (see Chapter. 3.4, Fig. 3.1). The lattice parameter of the silicon is 0.543nm, and silicon bond length is 0.235nm.

The MD simulation was used with Tersoff potential to solve Hamilton's classical equations of Si-Si motions with predictor-corrector algorithms with fixed time steps of 0.5fs. Two thermal properties of silicon were examined using MD simulations, (1) Thermal conductivity of bulk silicon at 300K and (2) phonon power spectrum at 300K. To examine these properties, a sample made of  $4 \times 4 \times 30$  unit cells of silicon was prepared. The size of each unit cell is  $5.431 \text{ \AA} \times 5.431 \text{ \AA} \times 5.431 \text{ \AA}$ , and the total size of  $4 \times 4 \times 30$  of silicon is  $2.7 \text{ nm} \times 2.7 \text{ nm} \times 163 \text{ nm}$ . During the simulation, periodic boundary conditions were applied. The initial structure was quenched to 0K for 50,000 steps and then equilibration at 300K was followed for 200,000 steps.

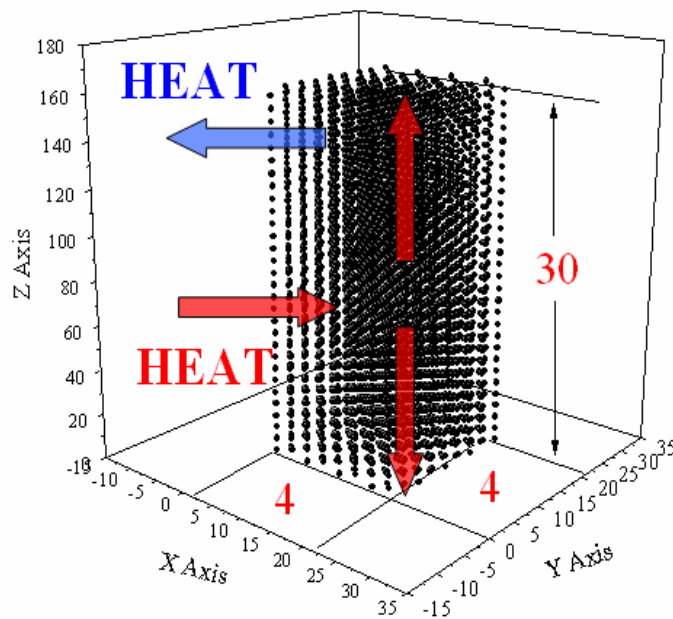


**Figure 4.1** The configuration of applying Fourier method to the bulk silicon.

The thermal conductivity of bulk silicon was calculated by the Fourier method. To build

a temperature gradient, the temperature of silicon center was set to 320K and that of end was set to 280K by the velocity scaling method as shown in Fig. 4.1. The steady state heat flow was calculated over 70,000 steps MD time out of 150,000 total MD simulation steps. Thermal conductivity of silicon calculated by NEMD using Fourier law approach was found to be 170W/mK at 300K. This result is close enough to standard thermal conductivity of silicon at 300K (150W/mK). The velocity auto-correlation functions were also calculated to determine the silicon phonon power spectrum. The phonon power spectrum is obtained by Fast Fourier Transformation (FFT) of velocity auto-correlation data. In Fig. 4.2 (a), the phonon spectrum from the MD simulation is plotted. The silicon phonon spectrum from Raman spectroscopy and theoretical expectations [58] are also plotted on Fig. 4.2 (b) for the comparison. The overall spectrum distribution and peaks positions from MD simulation are well matched to measured result.

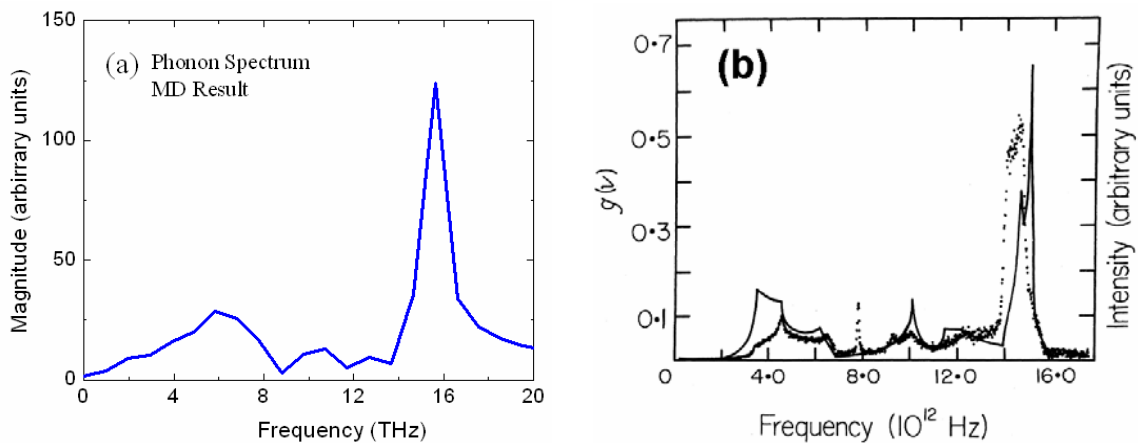


**Figure 4.2** The phonon spectrum (a) from MD simulation and (b) solid line: density of state and points; two phonon Raman spectrum [58]

### 4.3 Silicon Surface and Absorption of CNT

A dimerization of silicon surface is important to for device fabrication, since the lattice structure near the surface is changed due to the reactions on the surface. Fig 5.3 shows an illustration of the unreconstructed silicon surface [59]. The initial distance between two silicon surface atoms is  $3.84\text{\AA}$ . The orientation of two dangling bonds is favorable for bond formation between the two surface silicon atoms.

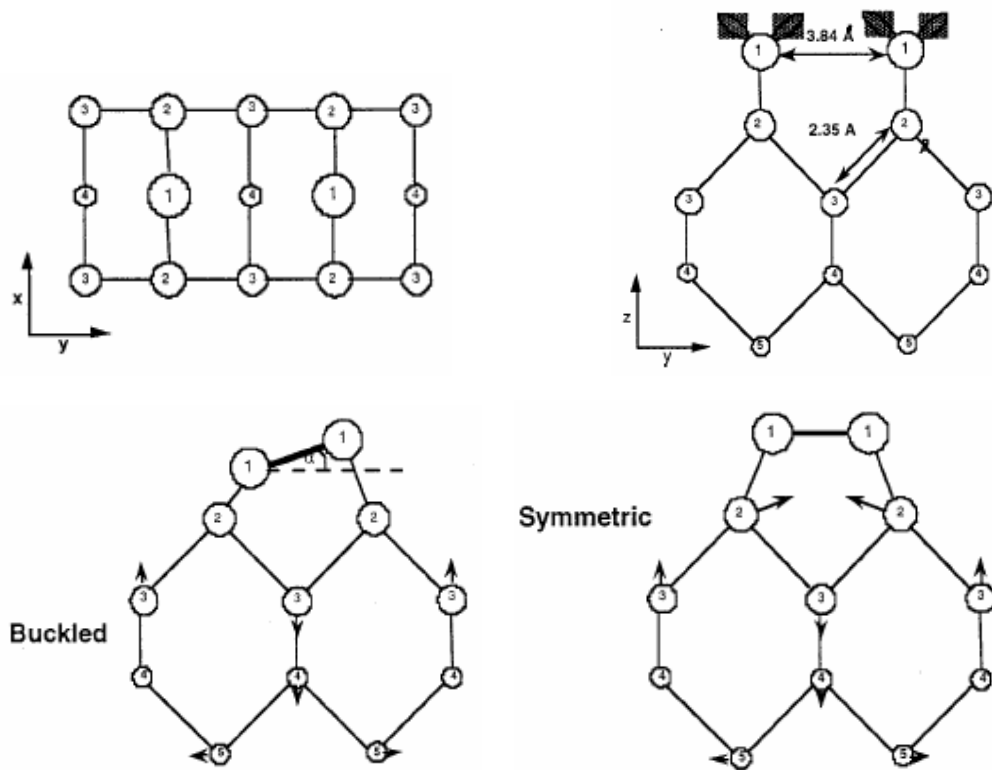


**Figure 4.3** Dimer formation on the Si (100) surface (Ref:59 )

After the dimer bond is formed as shown in Fig. 4.3, the distance between surface atoms is reduced by  $1.6\text{\AA}$  to approximately  $0.1\text{\AA}$  less than the Si lattice bond distance of  $2.35\text{\AA}$ . This large amount of atomic displacement on the silicon surface causes atomic

displacement in several layers below the surface. There are two dimerizations on silicon surface, symmetric and buckled dimerizations. In a symmetric dimerization, both silicon atoms are located in the same plane perpendicular to the (0,0,1) lattice direction with zero buckling angle. In a buckled dimer, one silicon atom is positioned above the other, with non-zero buckling angle  $\alpha$ . Experiments indicate that the dimerized Si (0,0,1) surface is dominated by buckled dimers rather than symmetric dimers. However, the multireference wave function models of dimer bonding in silicon clusters containing one or more dimers predict that the symmetric dimer is the true minimum. James et al [59] studied series of  $\text{Si}_n\text{H}_m$  clusters with ab initio electronic structure calculations. Figure. 4.4. shows the optimized geometry of  $\text{Si}_9\text{H}_{12}$ . Silicon atoms are shifted from lattice positions with direction of arrow. The atoms in dimer in the dimer move approximately  $0.8\text{\AA}$  closer to each other along the y-axis and  $0.15\text{\AA}$  down from the lattice positions. The second layer atoms are dragged along by the surface atoms and are drawn closer together.

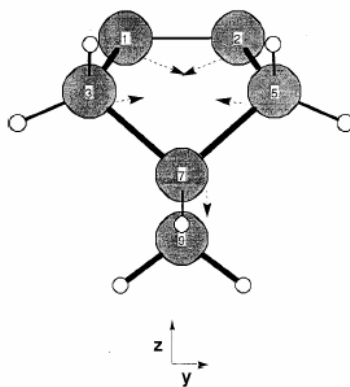


**Figure 4.4** Displacements of atoms near surface which is induced by the dimer formation in the  $\text{Si}_9\text{H}_{12}$  model. Displacements are indicated by arrows from bulk atom locations. (Ref:59 )

The displacement of the second layer brings the third layer atoms down roughly 0.1Å. They calculated the displacement of atoms in 4 layers below the dimer row with 6-31G basis and Hay-Wadt (HW) effective core potentials (ECPs). As it is shown in Table 5.1, the effect of surface dimer becomes smaller in deeper layers. Therefore, a few layers below the silicon surface shrink with small amount of atomic displacement due to the surface dimers.

Atom	HW ECP(d)			6-31G		
	$\delta x$	$\delta y$	$\delta z$	$\delta x$	$\delta y$	$\delta z$
Surface						
1	0.000	0.794	-0.154	0.000	0.804	-0.152
2	0.000	-0.794	-0.154	0.000	-0.804	-0.152
Layer 2						
3	0.026	0.137	0.083	0.031	0.144	0.091
4	-0.026	0.137	0.083	-0.031	0.144	0.091
5	0.026	-0.137	0.083	0.031	-0.144	0.091
6	-0.026	-0.137	0.083	-0.031	-0.144	0.091
Layer 3						
7	0.083	0.000	-0.098	0.085	0.000	-0.095
8	-0.083	0.000	-0.098	0.085	0.000	-0.095
Layer 4						
9	0.000	0.000	-0.003	0.000	0.000	0.004

**Table 4.1** Predicted atoms displacements by GVA-PP(1), which are induced by symmetric dimer formation in the Si<sub>9</sub>H<sub>12</sub> model of the Si (001) surface. (ref:59 )

Savas et al [60] studied carbon nanotube absorption on the various positions on the silicon (0,0,1) stepped surface. The locations of carbon nanotube on the silicon dimer surface are plotted in Fig 4.5. The dark bold spots indicate the silicon surface atoms and cylinder structure indicates (5,5) carbon nanotube on the silicon surface. Adsorption sites A~D are terrace adsorption sites which are parallel (B and D) or perpendicular (A and C) to the dimer rows. The absorption at the step edge has two metastable adsorption sites (E and G) with unequal stability due to the existence or lack of covalent bonding with lower terrace atoms. On the absorption of CNT on silicon surface, it was found that the bond length between carbon and silicon,  $d_{\Lambda} \sim 1.97 \text{ \AA}$  and this value is slightly larger than  $1.89 \text{ \AA}$  which corresponds to Si-C bond length in SiC.

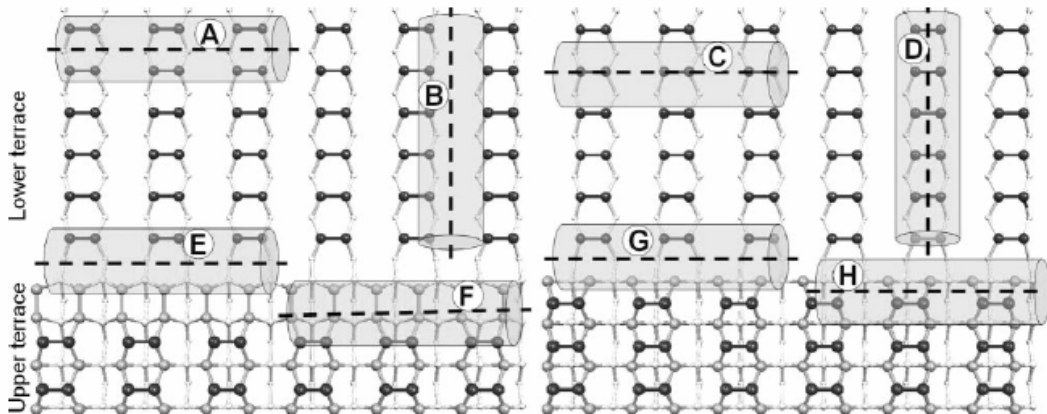


**Figure 4.5** Carbon nanotube adsorption sites on Si (001) stepped surfaces. (from ref 60)

The adsorption energy is defined by the energy difference between total energy of the combined system and the summation of the total energies of an isolated CNT and a clean

surface in the same simulation box. Positive adsorption energy indicates that adsorption is favorable on that site. Adsorption at site A is calculated as the most favorable site with the adsorption energy of 2.77eV. The least favorable adsorption site is C which has almost zero adsorption energy. The second most favorable adsorption sites are B which has adsorption energy of 1.76eV.

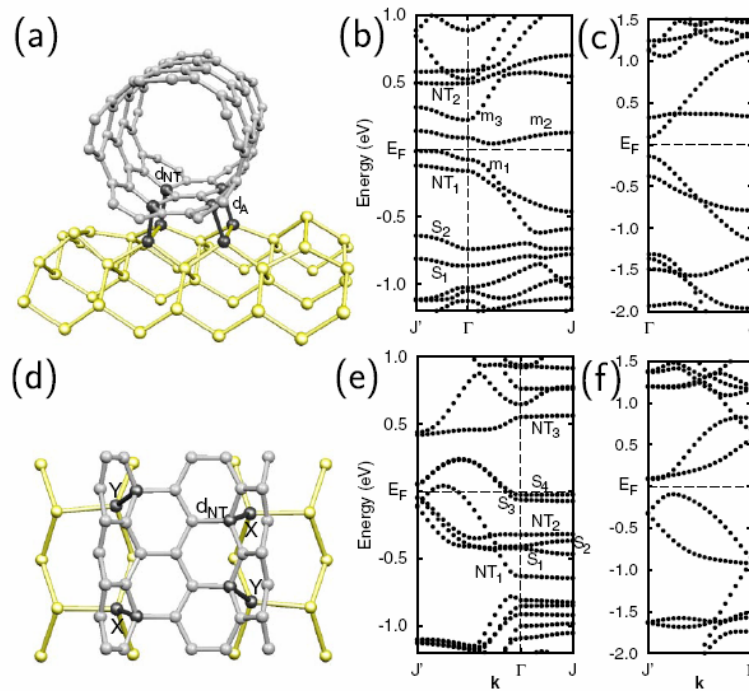


**Figure 4.6** Adsorbed (5,5) CNT and its atomic and electronic structure on the terraces of Si (001). (a) the relaxed structure and (b) the band structure of the CNT at site A (c) the band structure of 4H atoms bonded to the nanotube. (d) the geometry of atom and (e) the CNT band structure adsorbed at the site B, (f) The band structure of the (5,5) CNT bonded with 4H atoms. The Fermi levels  $E_F$  are indicated by the horizontal dashed lines. (from ref 60)

The geometry and energy band structure of site A and site B which are plotted in Fig. 4.6. show how the energy band and electric properties of nanotube change due to the absorption on silicon surface. In appendix A, it is shown that armchair CNT is metallic because the density states at the Fermi level has finite value and the energy gap becomes zero at the point K in the Brillouin zone. However, the energy band in Fig. 4.6 (b) shows semiconducting behavior because the Fermi level ( $E_F$ ) does not cross any energy band along  $\Gamma$  to J and band gap is also opened (see Fig. 4.6 (b)). When four hydrogen atoms are attached the same carbon atoms highlighted by dark shading in Fig. 4.6 (a), it changes the  $sp^2$  hybridization to  $sp^3$  hybridization and causes band gap opening as shown in Fig 4.6 (c). Therefore, the band gap opening of CNT on silicon surface is due to the carbon-silicon bonding which introduces  $sp^3$  bonded atoms into the  $\pi$  electron network results in the gap opening and the flattening of the  $\pi$  bands.

The adsorption geometry and its energy band on  $D_B$  step edge are plotted in Fig. 4.7. Because of the geometric restriction on silicon step edge, the CNT forms only three covalent bonds with silicon atoms on this site. The calculated adsorption energy for the step edge is  $\sim 1.88\text{eV}$  which is slightly larger than the corresponding value for the terrace trench at site B ( $\sim 1.76\text{eV}$ )

Therefore, the sites A and G are the most and second favorable adsorption site for carbon nanotube. Due to the carbon and silicon bonding, the  $sp^2$  bonding changes to the  $sp^3$  bonding and it causes the energy gap to be opened and the metallic nanotube comes a semiconducting one. In developing the CNT-Si interface structure, we use both adsorption sites A and G to make CNT stable at the interface under steady state heat flow.

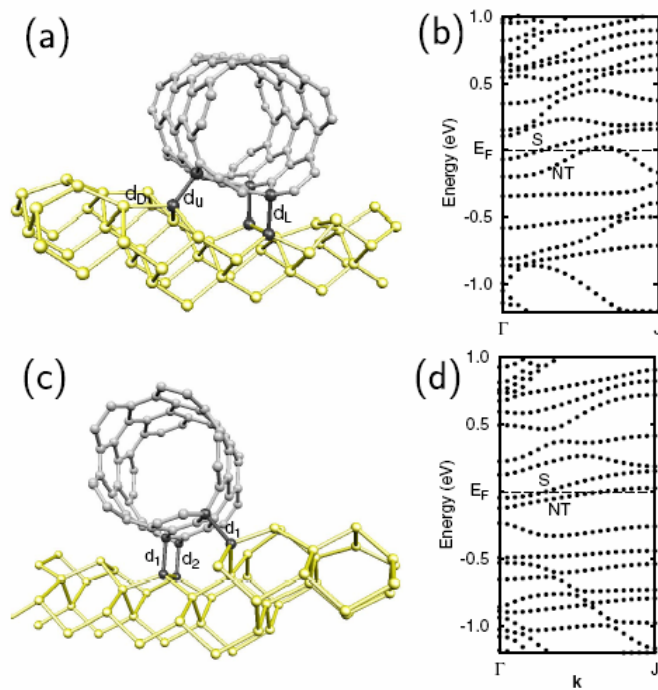


**Figure 4.7** The atomic and electronic structure of the CNT which is adsorbed (a)  $D_B$  step edge, site E, and (c) at step edge site G. the energy bands of the CNT adsorbed at the (b) site E and (d) site G. (from ref 60)

#### 4.4 Silicon Carbide

In developing silicon-carbon nanotube interface, it is necessary to apply bonded interaction on silicon and carbon. The Tersoff potential provides the inter-atomic potentials for multi-component system, such as SiC or SiGe. In MD modeling of silicon-CNT interface, it is difficult to trace silicon and carbons bonding working properly, since most atoms belong to C-C or Si-Si bonding. In order to examine the Si-C bonding and related MD modeling, it is necessary to prepare the system which contains only silicon and carbon bonding.

Silicon Carbide is a wide band gap semiconductor existing in many different polytypes. Since it is composed of two different atoms, it has more than 200 different polytypes depending on how layers stack together. The most common polytypes of SiC are cubic-3C SiC, 4H-SiC, 6H-SiC and 15R-SiC and their stacking sequence, number of hexagonal and number of cubic are summarized in Table 4.2. Each polytype side view and the order of stacking are plotted at Fig. 4.8.

	Staking Sequence	Number of Hexagonal	Number of Cubic
<b>2H</b>	AB	1	0
<b>3C</b>	ABC	0	1
<b>4H</b>	ABCB	1	1
<b>6H</b>	ABCACB	1	2
<b>15R</b>	ABCACBCABACBCB	2	3

**Table 4.2** Staking sequence in the c-axis direction for different SiC polytypes

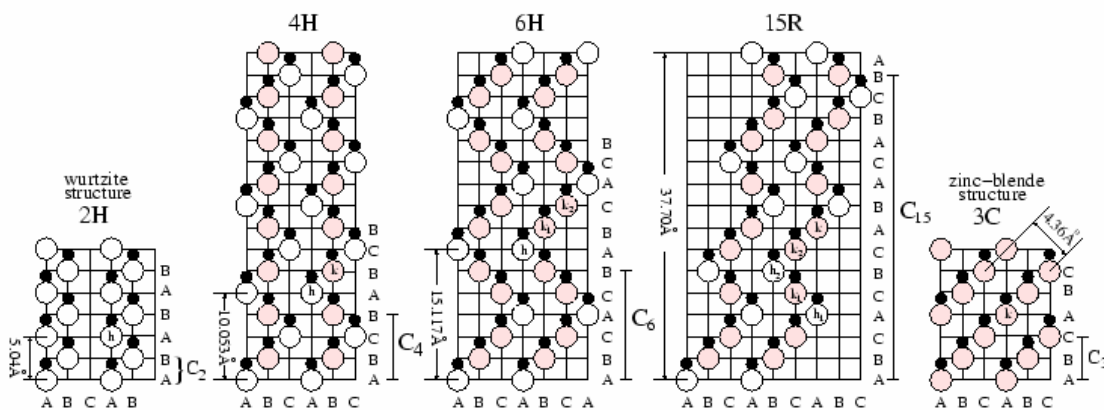


**Figure 4.8** Staking sequences for different SiC polytypes in the [1120] plane [61]

In order to examine the silicon-carbon bonding, 3C SiC (which is also called as  $\beta$ -SiC)

structure was prepared.  $\beta$ -SiC is the only form of SiC with a cubic crystal lattice structure. The crystal lattice form of  $\beta$ -SiC is zinc blende as shown in Fig. 4.9 (a). The lattice parameter of the crystal lattice is 0.436nm and the bond length of silicon and carbon is 0.189nm.

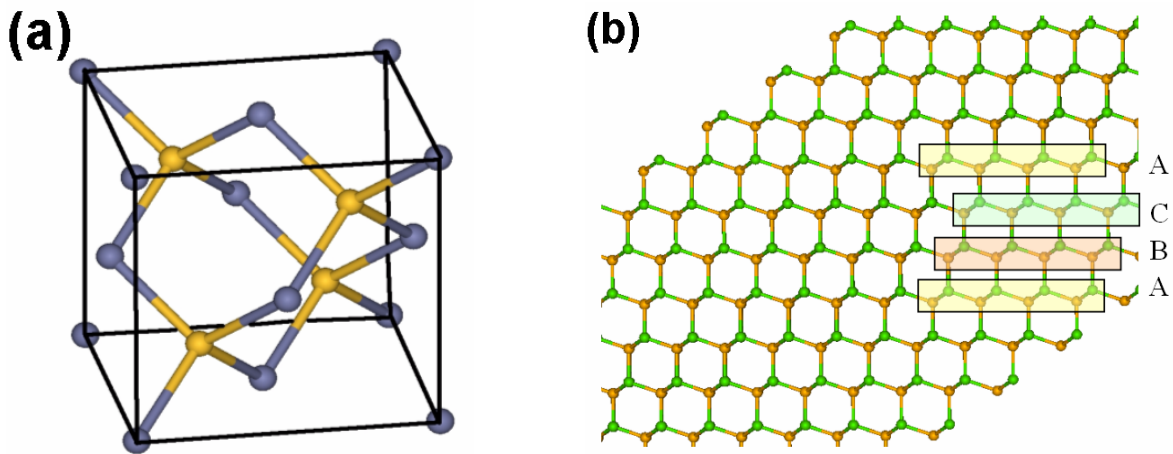


**Figure 4.9** (a) The zinc blende lattice structure of the  $\beta$ -SiC and (b) the generated bulk size of  $\beta$ -SiC.

A  $17.44\text{\AA} \times 17.44\text{\AA} \times 130.8\text{\AA}$  silicon carbide structure was used in MD simulation. In this structure, 1920 atoms are silicon and the other 1920 atoms are carbon. The prepared structure is plotted in Fig. 4.9 (b). The staking sequence of ABCA is indicated with different colored boxes. The initial structure was quenched to 0K for 20,000 MD time steps and followed by equilibration at 300K for 500,000 MD steps. The thermal conductivity was calculated with Fourier method. As shown in Fig. 5.10, the middle of structure was heated up to 320K, while the end of structure was cooled down to 280K. For the steady state heat flow simulation was performed for the last 80,000 steps out of 150,000 total MD simulation

steps.

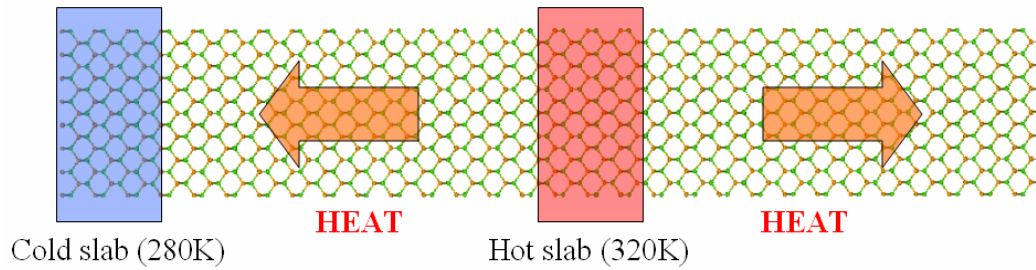


**Figure 4.10** The configuration of applying the Fourier method to the bulk  $\beta$ -SiC.

Thermal conductivity of  $\beta$ -SiC was calculated as 4.4W/cmK at 300K. This result is close enough to standard thermal conductivity of silicon at 300K (4.9W/cmK).

# **CHAPTER FIVE**

## **HEAT PULSE PROPAGATIONS IN DOUBLE WALL**

### **CARBON NANOTUBES**

#### **5.1 Introduction**

Carbon nanotubes exhibit thermal conductivities at room temperature that are higher than diamond and graphite. For example, some of the recent measurements of the thermal conductivities of multiwall and single wall nanotubes reported values exceeding 3000 W/mK at room temperature [2], whereas measured thermal conductivities of diamond (including type II and thin films grown using chemical vapor deposition (CVD) process) range from 1300 to 2200 W/mK and that of graphite range from 1800 to 2000 W/mK [3,4]. However, the thermal conductivities of both diamond and graphite reach their maximum values well below room temperature (175K for diamond and 100K for graphite) [3,4]. On the other hand, the measured thermal conductivities of single wall nanotubes (SWNT) and multiwall carbon nanotubes (MWNT) exhibit a monotonic increase up to room temperature [2,29]. Furthermore, nanotube bundles and mats exhibit lower thermal conductivities compared individual SWNT and MWNT [32] and showed improvement under alignment [34]. A lowering of the thermal conductivity of individual multi-wall nanotubes with increased diameter to values lower than that of graphite was also reported in [2]. Investigations of the thermal conductivity of carbon nanotubes (CNT) using molecular dynamics (MD) simulation also report a wide range of thermal conductivities and show

dependence of sample length [37-41]. These investigations used non-equilibrium molecular dynamics (NEMD) method based on Fourier law [37,38], NEMD using fictitious external forces [37], and equilibrium molecular dynamics (EMD) based on the Green-Kubo approach [38] to calculate the thermal conductivity of CNT. However, NEMD and EMD methods use the steady state overall heat flux in calculating the thermal conductivity of CNT. Unfortunately, these methods do not provide any information about the participating phonon modes or the energy carried by individual phonon modes because the heat flux is either evaluated from velocity scaling to balance a temperature gradient or an external force for NEMD and velocity and energies of atoms for EMD [40]. On the other hand, investigations of heat pulse propagation in CNTs can provide information about the participating phonon modes and their contribution to overall heat conduction [41,62,63].

The drop in thermal conductivities beyond its maximum is attributed to defects and anharmonic phonon-phonon scattering (Umklapp process) [64]. Therefore, the onset of Umklapp processes occur at low temperatures in graphite and diamond compared to nanotubes which exhibit a drop beyond room temperature. This indicates differences in the phonon scattering processes between diamond, graphite and nanotubes. For example, there is no one to one correspondence between phonon modes in nanotubes and graphite, even though nanotubes can be viewed as rolled graphene sheets. The acoustic phonon modes in SWNT include (1) doubly degenerate transverse acoustic modes (TA) that involve vibrations perpendicular to the nanotube axis (as in plucking a string), (2) longitudinal acoustic mode (LA) with vibrations along the nanotube axis, and (3) twisting mode (TW)

with displacements in the cylindrical plane perpendicular to the axis of an isolated nanotube [65]. The out of plane tangential acoustic (TA) mode in graphene sheet corresponds to the radial breathing mode in a nanotube (TB) [65]. However, the radial breathing mode has nonzero frequency at zero wave-vector ( $k=0$ ) and thus can be viewed as an optical phonon mode. The acoustic twisting phonon mode and the radial breathing modes are exhibited by nanotubes and are not present in graphite or diamond. Furthermore, the radial phonon modes show strong dependence on nanotube diameter and their effect on heat flow in multiwall nanotubes will depend on the number of shells in a MWNT. Changes in nanotube diameters can excite different radial phonon modes that participate in transmitting heat and phonon-phonon interactions at high temperatures. Recent theoretical investigations of relaxation through Umklapp processes in zigzag nanotubes have shown phonon mean free path length of the order of 1  $\mu\text{m}$  at 300 K [66].

The molecular dynamics approach provides an ideal platform for investigating the thermal conductivity and the processes involved in transient heat transport because the underlying phonon-phonon interactions are included in a natural way. However, classical MD approach does not account for electron contribution to the thermal conductivity even though all carbon nanotubes are either metallic or semiconducting. Fortunately, the experimentally measured ratio of the electron to phonon thermal conductances  $\kappa_{el} / \kappa_{ph}$  are quite small [31,34] which makes it possible to neglect the role of electron contribution to thermal conductivity. The theoretical model in [67] predicts a ratio that is an order of magnitude higher than the experimentally observed ratio.

Heat pulse measurements at low temperatures in NaF revealed Ballistic LA and TA phonon mode propagation as well as second sound waves at temperatures below 14 K [68,69]. Therefore heat pulse experiments provide quantitative information on transport by diffusion, ballistic phonons, and second sound waves. The speed of the leading edges of pulses arriving at the detector was determined from the arrival time and the sample length and used to identify the ballistic phonon modes (LA or TA) [68,69]. Heat pulse propagation in one- two- and three- dimensional  $\alpha$ -iron lattices was investigated using MD simulation approach in [70] and showed that the application of strong heat pulse generated several heat wave packets moving at different speeds corresponding to different phonon mode. They also reported that the propagation of leading heat wave packet coincided with the propagation of the strong longitudinal stress wave ( $S_{zz}$ ).

Recently, we investigated using MD simulations transient heat pulse flow in (7, 0), (10, 0), and (5, 5) single wall carbon nanotubes with particular emphasis on the role of nanotube chirality and diameter at very low temperatures and showed that the heat pulse generated wave packets that moved at the speed of sound corresponding to different phonon modes, second sound waves, and diffusive components [62]. The energy in the wave packets corresponding to LA, TW phonon modes and second sound in zigzag nanotubes was also found to be larger than in armchair nanotubes of similar diameter. Furthermore, the energy carried by LA phonon mode wave packets was found to be 10 and 40 times smaller than the TW and second sound wave packets, respectively, which indicate a smaller contribution by ballistic LA phonons to the overall thermal conduction at very low temperatures [41,62]. Diffusive heat conduction in (5, 5) SWNT at 50 K following

application of a heat pulse was also investigated using MD in [63]. They performed a spectral analysis of the phonon modes that dominate diffusive heat flow and reported that diffusive heat propagation in SWNT can be described by dual relaxation time model rather than the conventional hyperbolic energy equation. Sound wave propagation in MWNT was also examined using analytical approach in MWNT [71].

In this research, we investigate heat pulse propagation in zigzag and armchair double wall carbon nanotubes (DWNT) with the goal of understanding the role of different phonon modes in heat conduction. Additionally, MD simulations of single wall nanotubes (SWNT) corresponding to the shells of the DWNT were also investigated and compared to the inner and outer shells of the DWNT to determine the role van der Waals interaction between the shells in MWNT. The energies and propagation speeds of the leading heat wave packets in DWNT and corresponding SWNT were examined. We limit our analysis to the leading heat wave packets in DWNT and SWNT to understand the reason behind the significant increase in the energies of the leading LA wave packets in DWNT compared to SWNT. Simple strains due to bond stretching and/or bond angle bending within the LA mode in the outer and inner shells of the zigzag and armchair DWNTs were also found to be larger than those in the corresponding SWNT.

## **5.2 Methodology**

The MD simulation used the Tersoff-Brenner bond-order potential for carbon-carbon interaction with predictor-corrector algorithm and fixed time step of 0.5fs [55,57]. The non-bonding carbon-carbon interaction between shells in DWNT is modeled

by 6-12 Lennard-Jones type van der Waals potential:

$$U_{vdW} = \sum_{\text{non-bonded pairs}} 4\epsilon \left[ \left( \frac{\sigma}{r_{ij}} \right)^{12} - \left( \frac{\sigma}{r_{ij}} \right)^6 \right] \quad (5.1)$$

Where  $r_{ij}=|r_i-r_j|$  is the separation between two atoms,  $i$  and  $j$  in the different shells,  $\epsilon = 4.41\text{meV}$  is the potential well depth,  $\sigma=3.35 \text{ \AA}$  is the van der Waals separation distance and the cut off distance  $r_{\text{cut}}=8.875 \text{ \AA}$  [72].

The armchair DWNT consists of (5,5) inner shell and (10,10) outer shell, whereas the zigzag DWNT had a (9,0) and (18,0), inner and outer shells respectively. The separation between shells is  $3.4\text{\AA}$  for armchair DWNT and  $3.5 \text{ \AA}$  for zigzag DWNT [73]. All carbon nanotubes used in this simulation are divided into 250 slabs and the width of each slab is  $4.26\text{\AA}$  in zigzag CNT and  $4.92 \text{ \AA}$  for armchair CNT. The total length of 250 slabs amounted to  $1065 \text{ \AA}$  and  $1230 \text{ \AA}$  for the zigzag and armchair CNTs, respectively. The number of atoms per slab increases as the diameter of the nanotube increases. For each simulation, energy minimization of the DWNT structure with respect to the relative orientation and lateral displacements of the shells was initially performed to achieve a stable configuration of the system. The details of the boundary conditions and the procedures for applying heat pulse are the same as those reported earlier for single wall nanotubes [62].

The MD simulations of heat pulse propagations were performed on the following

systems (1) zigzag (9,0)/(18,0) DWNT, (2) armchair (5,5)/(10,10) DWNT, (3) armchair (10,10)/(15,15) DWNT, (4) armchair (5,5) and (10,10) SWNTs and (5) zigzag (9,0) and (18,0) SWNTs. For the first two cases, the DWNTs were chosen to have similar radii to examine the role of chirality and how the interaction between nanotube shells affects heat flow through the DWNT. In order to examine the role of curvature of DWNT shells in heat flow and strain, MD simulation of armchair DWNT (10,10)/(15,15) was performed and compared to armchair DWNT (5,5)/(10,10). During heat pulse propagation, both inner and outer shells undergo different deformations depending on the vibrational modes of atoms within a given wave packet. The van der Waals interaction between shells also influences the manner in which each shell changes shape and tends to result in an inward force on some of the shells [74]. Within each slab, the distances  $L_1$  and  $L_2$  shown in Fig. 5. 1(a), were calculated at certain time intervals from the positions of the atoms and repeated along the circumference of the slab for atoms with similar symmetry.

The average distance  $\bar{L}_2$  is given by

$$\bar{L}_2 = \frac{1}{N} \sum_{i=1}^N [Z_u(i) - Z_d(i)] \quad (5.2)$$

Where  $Z_u(i)$  and  $Z_d(i)$  are the z-coordinates of the atom pairs at time t and N is the number of atoms along the circumferences at  $Z_u(i)$  and  $Z_d(i)$ . From the values  $\bar{L}_2$  at time t and the corresponding equilibrium value, the change  $\Delta L = \bar{L}_2(t) - \bar{L}_2(0)$  is evaluated. The same procedure is used to determine  $\bar{L}_1$  and the corresponding change  $\Delta L = \bar{L}_1(t) - \bar{L}_1(0)$ .

The fractional change in bond length  $\varepsilon = \Delta L / L(0)$  is used as a measure of the simple strain along the nanotube axis [75]. This definition ignores contributions from shear strain which can lead to a tensor form for the strain. As will be shown in the next section, significant strain occurs within the wave packets associated with LA phonon modes where one expects compressions and dilation along the nanotube axis. For the armchair nanotube, only one distance  $L$ , shown in Fig. 5.1(b), is evaluated due to the symmetry of the unit cell.

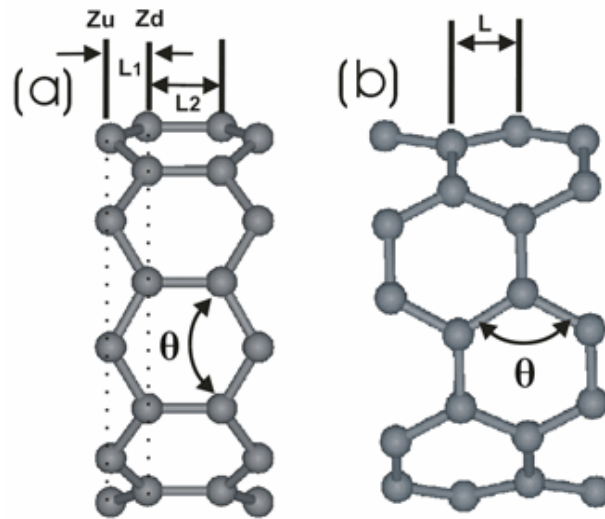


**Figure 5.1** The structure of a cell of (a) zigzag CNT and (b) armchair CNT shows the parameters for bond stretching and bond bending

### 5.3 Results and Discussion

The temporal and spatial variations of the overall kinetic temperature in zigzag DWNT are shown in Fig. 5.2 and clearly demonstrate how heat pulse develops and propagates as

separate wave packets on the DWNT.

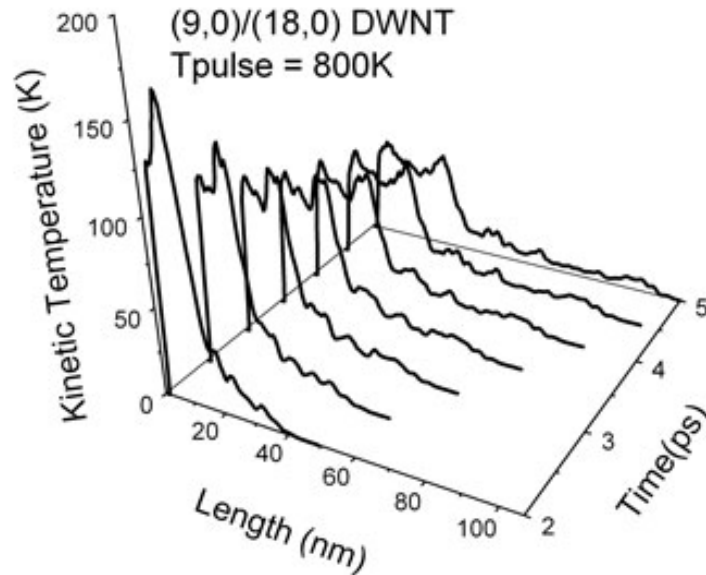


**Figure 5.2** Temporal and spatial distribution of kinetic temperature along zigzag DWNT

At longer times, relatively weak leading heat wave packets form and move at higher speeds compared to the strong diffusive thermal background. We focus on the physical properties of leading heat wave packets in DWNT, the contributions of the inner and outer nanotubes, and how they compare to SWNT. The total energy transferred to the zigzag DWNT system during the 1ps heat pulse was 0.264 eV/atom of which 0.226 eV/atom was delivered to the inner shell and 0.283 eV/atom to the outer shell. Under the same simulation conditions, the energies delivered to (9,0) SWNT and (18,0) SWNT were 0.27 eV/atom and 0.278 eV/atom, respectively.

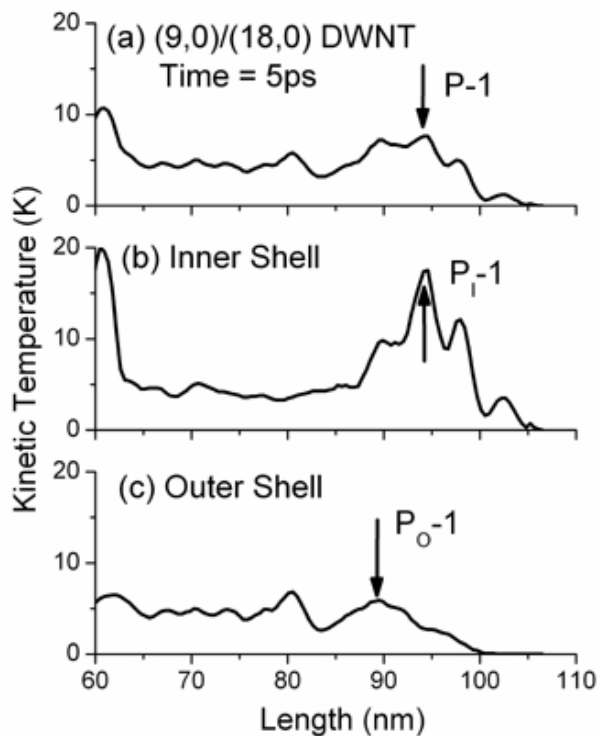


**Figure. 5.3** Spatial distribution of kinetic temperature at 5ps after application of heat pulse: (a) zigzag DWNT, (b) (9,0) inner shell and (c) (18,0) outer shell.

Figure 5.3(a) shows the leading heat wave packets in zigzag DWNT at 5ps. The broader leading wave packet in the range of 84 nm~106.5 nm has several peaks and yields an average speed 20.1km/s, which corresponds to the speed of sound associated with LA phonon mode. In order to get more quantitative information about heat wave propagation in inner and outer shells of the DWNT and to understand how each nanotube shell in DWNT contributes the overall kinetic temperature, the kinetic temperature of the inner and outer nanotube were calculated separately and the results are shown in Figs. 5.3(b) and (c). The average speed of the leading heat wave packets in the inner (denoted as  $P_i-1$ ) and the outer

nanotubes (denoted as  $P_0-1$ ) are 20.4km/s and 18.7km/s, respectively, which are close to the speed of sound associated with LA phonon mode.

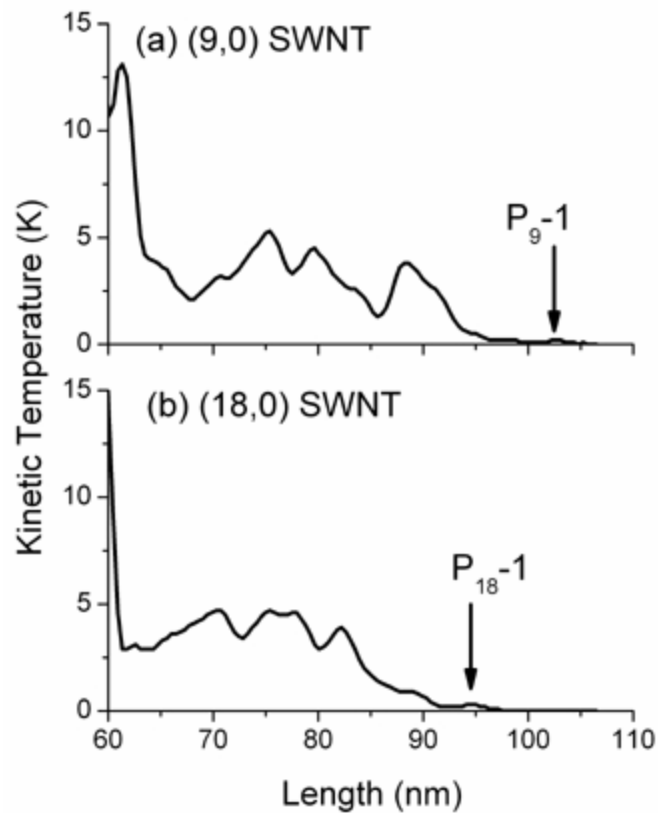


**Figure. 5.4** Spatial distribution of kinetic temperature at 5ps along (a) (9,0) SWNT and (b) (18,0) SWNT.

In order to determine whether the interlayer van der Waals interaction influences heat flow in DWNT, heat pulse propagation in (9,0) and (18,0) zigzag SWNTs were simulated and the resulting leading wave packets are shown in Fig. 5.4. The speeds of leading wave packets ( $P_9-1$  and  $P_{18}-1$ ) in (9,0) and (18,0) SWNT were found to be 20.8km/s and 19.3km/s, respectively which correspond to LA phonon modes. Although these speeds

are similar to the speeds of the leading heat in DWNT, the intensity of the leading wave packets beyond 85 nm in SWNTs are considerably weaker than those in the corresponding shells of the DWNT. For example, heat energy content of the leading wave packets (87.3 nm~106.5 nm) in the (9,0) inner shell of the DWNT denoted by P<sub>I-1</sub> in the Fig. 5.3 (b) is seven times larger than the heat energy in the same region of (9,0) SWNT (60 meV vs. 8 meV) as can be seen in Fig. 5.4 (a). Similarly, the energy in the (18,0) outer shell of the DWNT in the region covered by the broad wave-packet (P<sub>O-1</sub>) is 5 times larger than the energy in (18,0) SWNT (20 meV vs. 4 meV). Within the leading heat wave packets in both zigzag SWNT and DWNT, which propagate at the speed of sound associated with LA mode, bond stretching and bond angle bending lead to local strain variations within the nanotubes. It is well known that compressive elastic deformations in metallic materials lead to a decrease in volume and an increase in temperature [76,77]. Furthermore, tight binding and MD simulations of torsionally strained nanotubes demonstrated higher chemical reactivity of carbon nanotubes in kink regions where strain is high [78,79]. Therefore, the higher kinetic temperature in the shells of DWNT within the LA mode wave packets compared to the corresponding SWNTs can be attributed to their being subjected to stronger strain fields. The simple strain along the axis of the DWNT and SWNT due to bond stretching was calculated following the procedure discussed in section 2. The values of  $\Delta L_1$  and  $\Delta L_2$  accounting for the changes in  $L_1$  and  $L_2$  shown in Fig. 5.1(a), were first averaged over the circumference of the CNT and the two neighboring unit cells before computing the simple strain  $\varepsilon_1 = \Delta L_1 / L_1(0)$  and  $\varepsilon_2 = \Delta L_2 / L_2(0)$ . The strain  $\varepsilon_2$  is mainly due to bond stretching whereas both bond stretching and angle bending contribute to strain  $\varepsilon_1$ . For the zigzag

DWNT shells and SWNTs, within each slab we combine both changes  $\Delta L_1$  and  $\Delta L_2$  in evaluating the simple strain  $\varepsilon = (\Delta L_1 + \Delta L_2) / (L_1(0) + L_2(0))$ . Fig. 5.5 shows that within the leading wave packet, the inner shell undergoes significant longitudinal compression as evidenced by the negative values of the strain whereas the outer shell bonds are stretched. As can be seen the magnitude of the strain in the inner shell is almost twice as large as the strain in the outer shell. The width of the regions with strong strain and positions of the maxima coincide with the leading heat wave packets ( $P_{1-1}$  and  $P_{0-1}$ ) as shown in Figs. 5.3 (b) and (c). The strain in (9,0) and (18,0) SWNT are shown in Fig. 5.6. The maximum average strain in the inner shell of the DWNT is seven times larger than that in (9,0) SWNT whereas the outer shell exhibits a strain that is nine times larger strain than that of (18,0) SWNT.

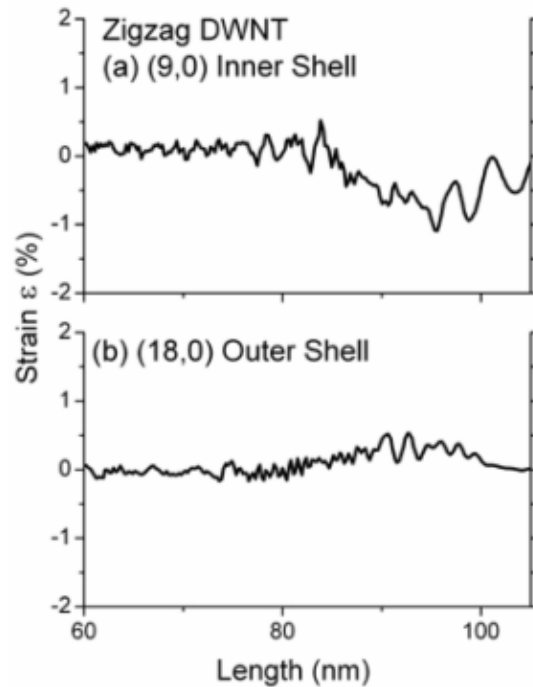


**Figure 5.5** The distribution of strain  $\varepsilon$  in (9,0)/(18,0) DWNT (a) inner shell and (b) outer shell.

The larger strain in the inner shell compared to the outer shell accounts for the larger kinetic temperature of the peaks of the leading wave packet in the inner shell compared to outer shell of the DWNT. The heat energy stored in each shell within these wave packets (see Fig. 5.3) is 60 meV for inner shell and 20 meV for outer shell. Therefore, within the leading LA mode wave packets, the outer and inner shells in DWNT experience stronger strain compared to SWNTs.

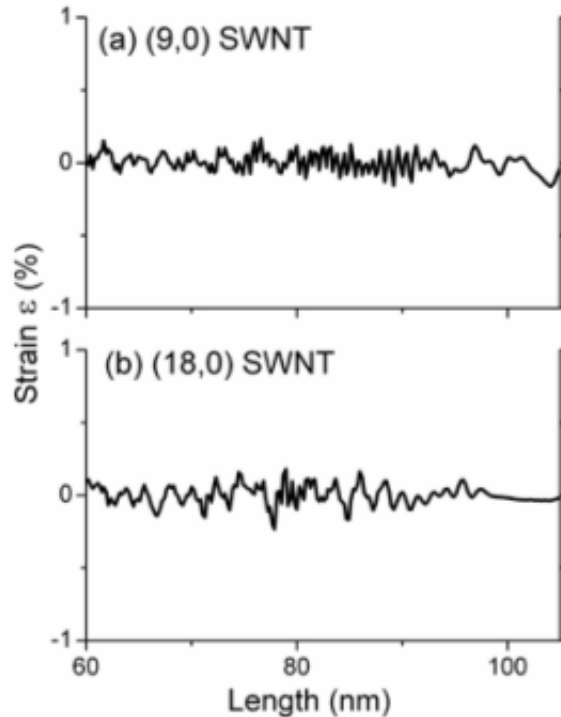


**Figure 5.6** The distribution of strain  $\epsilon$  in (a) (9,0) SWNT and (b) (18,0) SWNT

In order to understand the connection between strong strain and high energy within the leading heat wave packets in DWNT, we calculated the strain from strain rate using the kinetic temperature distribution in Fig. 5.3. Because, the changes in bond length

and bond angles are time dependent during heat pulse propagation along the nanotube, one can define the strain rate  $\dot{\varepsilon} = \frac{d\varepsilon}{dt}$  [80]. Furthermore, because the velocity is known at every point, the strain rate can be expressed as

$$\dot{\varepsilon} = \frac{d\varepsilon}{dt} = \frac{v_1 - v_2}{L} \quad (5.3)$$

where  $v_1$  and  $v_2$  are the local instantaneous velocities at any two points separated by a distance  $L$  [80]. The velocity  $v$  is related to the kinetic temperature  $T$  shown in Fig. 5.7(a) by  $v = \sqrt{kT/m}$ , where  $k$  is Boltzmann constant and  $m$  is the mass. In our case, the kinetic velocity  $v_2 = 0$  at the leading edge and the average strain rate  $\dot{\bar{\varepsilon}}$  over the distance  $L_z$  can be approximated by  $\dot{\bar{\varepsilon}} \approx v_1 / L_z$  [81]. The average strain over the distance  $L_z$  is then obtained by integrating equation (3) as follows

$$\bar{\varepsilon} = \int \dot{\bar{\varepsilon}} dt \approx \frac{v_1}{L_z} \Delta t \quad (5.4)$$

Where  $\Delta t$  is the time it takes to travel the distance  $L_z$  and is obtained by examining the temperature profiles at different earlier time steps. Using the velocity profile along the inner shell of zigzag DWNT shown in Fig. 5.7, which corresponds to the kinetic temperature profile in Fig. 5.3 (b), the calculated average strain was found to be  $\bar{\varepsilon} = 0.55\%$ .

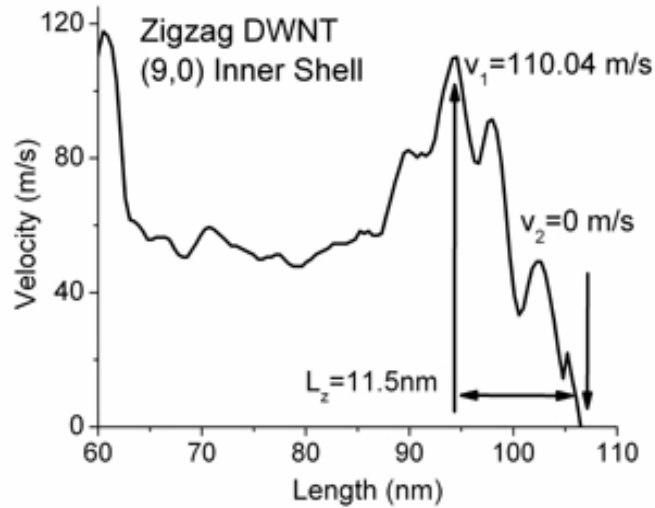


**Figure 5.7** Velocity distribution along (9,0) inner shell of (9,0)/(18,0) DWNT.

On the other hand, the average strain over the same region obtained from Fig. 5.5 was = 0.48% which is of the same order of magnitude. The difference is attributed to the fact that the strains are the instantaneous values at 5 ps whereas the velocities are time averaged. Therefore the higher energy in leading heat wave packets in DWNT is strongly related to the stronger strain in DWNT compared to SWNT [82].

The MD simulations were also performed on (5,5)/(10,10) armchair DWNT with the same heat pulse parameters to examine how chirality affects the energy flow in the DWNT. Furthermore, in order to understand how the van der Waals interactions between the inner and outer shells of the DWNT affect the heat flow in armchair DWNT, heat pulse propagation in (5,5) and (10,10) SWNTs were also simulated. The total energy supplied by the heat pulse to the armchair DWNT during first 1ps was 0.238 eV/atom. The energy of

0.243 eV/atom and 0.235 eV/atom were delivered to inner and outer armchair CNT.

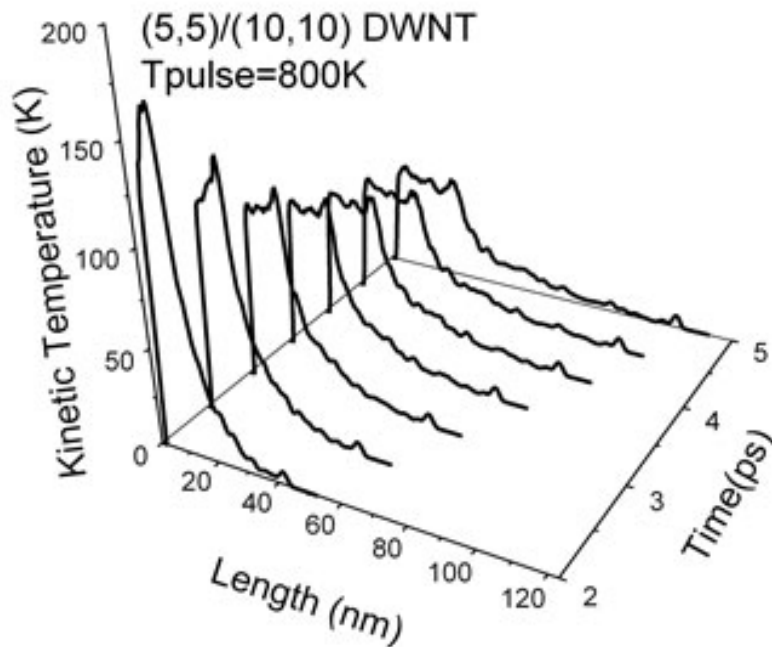


**Figure 5.8** Temporal and spatial distribution of kinetic temperature along armchair (5,5)/(10,10) DWNT

The temporal and spatial variations of the overall kinetic temperature in armchair DWNT are shown in Fig. 5.8 where as the leading heat wave packets beyond 60 nm at 5ps are plotted in Fig. 5.9(a). The physical properties of the leading heat wave packets for both inner and outer armchair CNT were examined in detail and compared to zigzag DWNT, (5,5) and (10,10) SWNTs. The average speed of the leading wave packets in armchair DWNT, P-1 and P-2 in Fig. 5.9(a) was 20.8 km/s, which corresponds to the speed of LA modes [62]. The kinetic temperatures of the inner and outer shells of the DWNT and the corresponding SWNTs are shown in Figs. 5.9(b), (c) and 5.10.

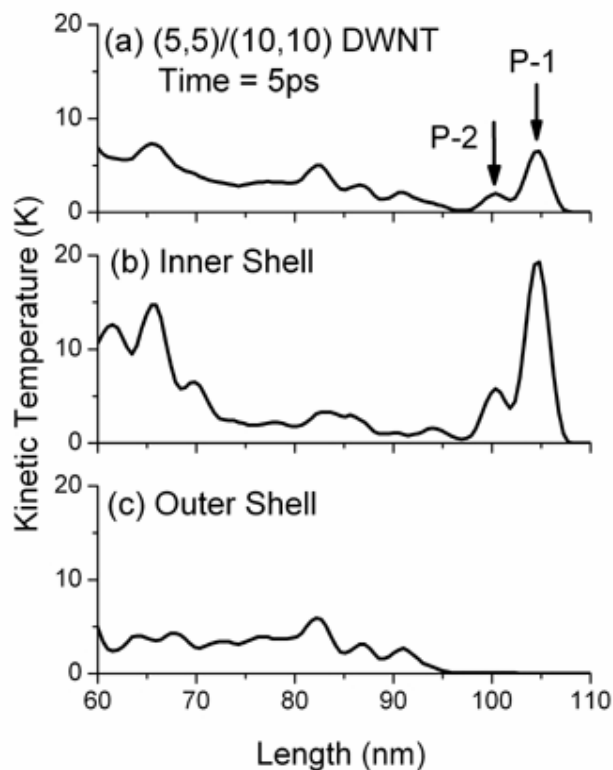


**Figure 5.9** Spatial distribution of kinetic temperature at 5ps along (a) armchair (5,5)/(10,10) DWNT, (b) (5,5) inner shell and (c) (10,10) outer shell.

The leading wave packet in the inner shell of the DWNT is stronger than the ones in the outer shell and (5,5) SWNT. The peak kinetic temperature of the leading wave packet in the inner shell of the DWNT is about 20 K which is about 40 times larger than that of the leading wave packet peak in (5,5) SWNT. Furthermore, this strong peak is located further away into the nanotube compared to the one in SWNT (104.8 nm vs. 98.4 nm from left end of the CNT). The average speed of the three leading peaks in the inner shell of the DWNT is 20.4 km/sec whereas that of the one in SWNT is 20.3 km/s indicating that these peaks propagate at the speed of sound corresponding to LA phonons. The overall total kinetic

energy of the atoms within the three peaks of (5,5) inner shell of the DWNT is about 26 meV which is significantly larger than the 0.2 meV carried by atoms within the weak leading wave packet in (5,5) SWNT. The peak of the leading wave packet in the outer shell maintains an average kinetic temperature of 3 K and is higher than the maximum kinetic temperature of the leading wave packet in (10,10) SWNT.

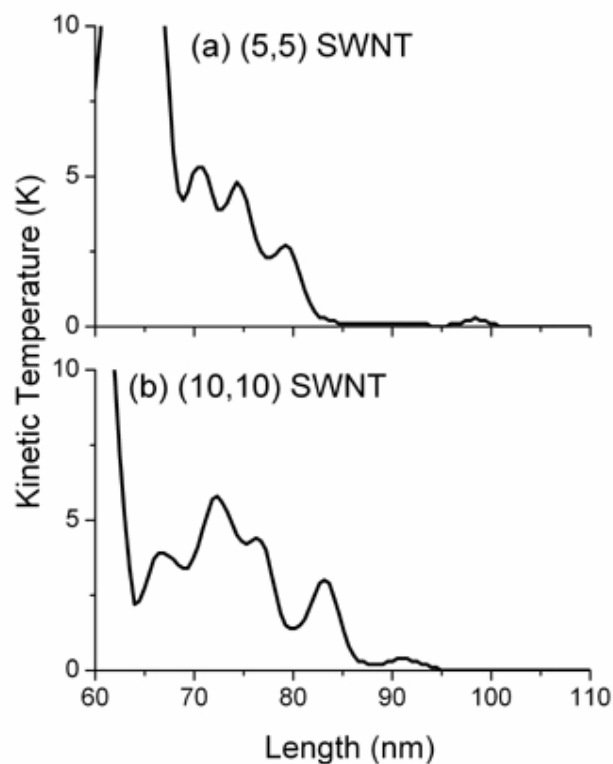


**Figure 5.10** Spatial distribution of kinetic temperature at 5ps along (a) (5,5) SWNT and (b) (10,10) SWNT.

The overall energy content of leading heat wave packets in the (10,10) outer shell of DWNT ( $P_0-1$ ) is about 3 times larger than the energy in (10,10) SWNT (15 meV vs. 5 meV). The simple strain along the axis of the DWNT and SWNT due to the changes in

bond length and/or bond angles was calculated using the procedure discussed earlier, in order to understand the reason behind the higher kinetic temperatures in the inner and outer shells of armchair DWNT compared to the corresponding SWNTs. The induced strain  $\epsilon$  in DWNT and SWNT at 5ps is shown in Figs. 5.11 and 5.12, respectively.

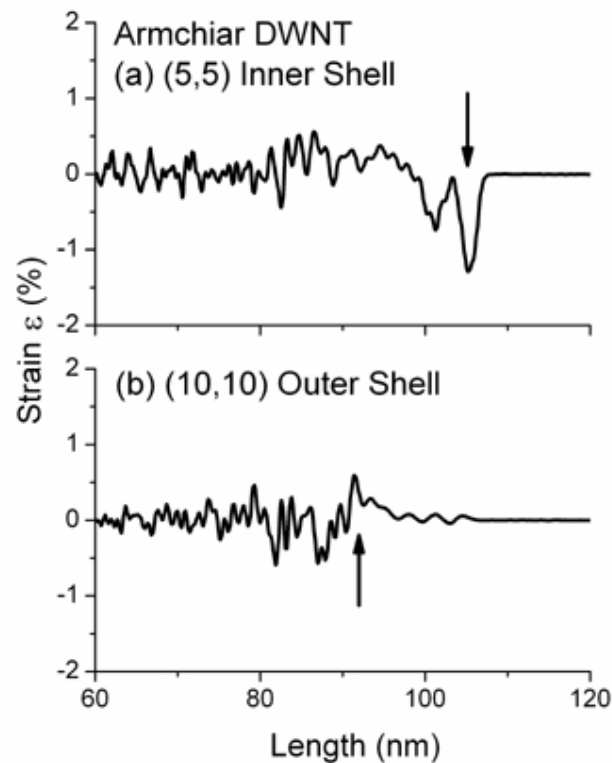


**Figure. 5.11** The distribution of strain within the leading wave packets in (5,5)/(10,10) DWNT (a) inner shell and (b) outer shell.

Fig. 5. 11(a) shows that the inner shell in DWNT experiences stronger strain compared to the outer shell. Furthermore, the maximum strain in the inner shell occurs close to the leading edge of the propagating wave packet and is negative indicating a strong compression. Additionally, the locations of the regions with maximum negative strain

coincide with the regions of the maximum kinetic temperatures of the two leading peaks as can be seen in Figs. 5.9(b) and 5.11(a). The outer shell, on the other hand, experiences a positive strain within the leading LA wave packet and its magnitude is smaller than that in inner shell. The larger strain in the inner shell compared to the outer shell accounts for the larger temperature of the peaks of the leading heat wave packets in inner shell in comparison to the outer shell.

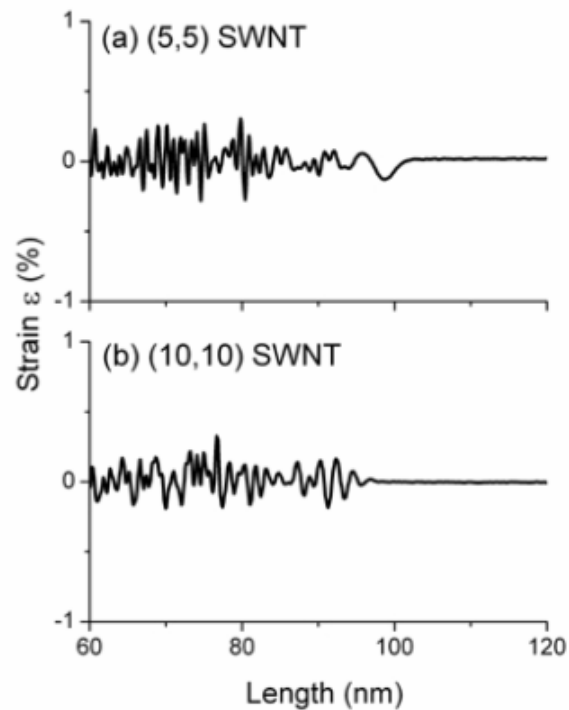


**Figure 5.12** The distribution of strain within the leading wave packets in (a) (5,5) SWNT and (b) (10,10) SWNT

The induced strain in (10,10) and (5,5) SWNTs were significantly smaller than in DWNT as can be seen in Fig. 5.12. For example, the maximum average strain in the inner

nanotube of the DWNT is about ten times larger than that in (5,5) SWNT where as the outer shell has 3.6 times larger strain than that of (10,10) SWNT. The calculated average strain in the inner shell of armchair DWNT using the kinetic temperature distribution in Fig. 5.9 was 0.5% which is comparable with the 0.7% average obtained from the data in Fig. 5.11.

Heat pulse propagation in the larger DWNT, (10,10)/(15,15) was also investigated using the same simulation conditions to determine whether the curvature of the inner shell is responsible for the strong strain in inner shell. The temperature and strain along the inner and outer shells of the (10,10)/(15,15) are shown in Figs. 5.13 and 5.14.

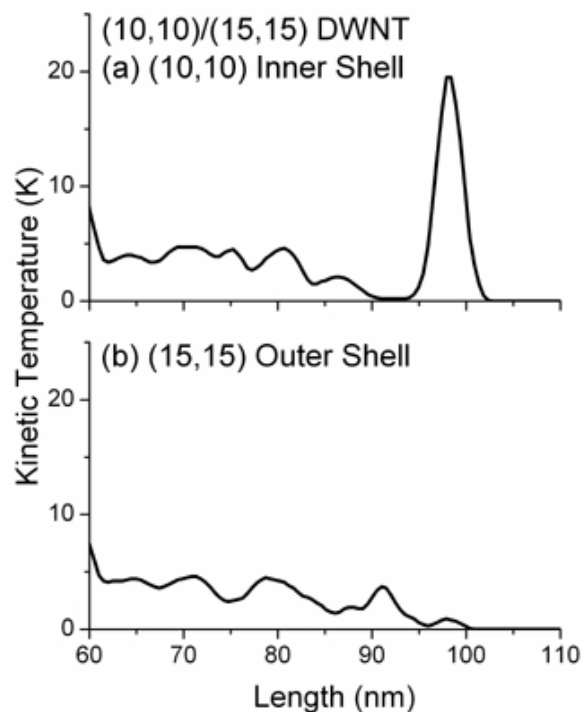


**Figure 5.13** Spatial distribution of kinetic temperature at 5ps along (10,10)/(15,15) DWNT: (a) (10,10) inner shell and (b) (15,15) outer shell.

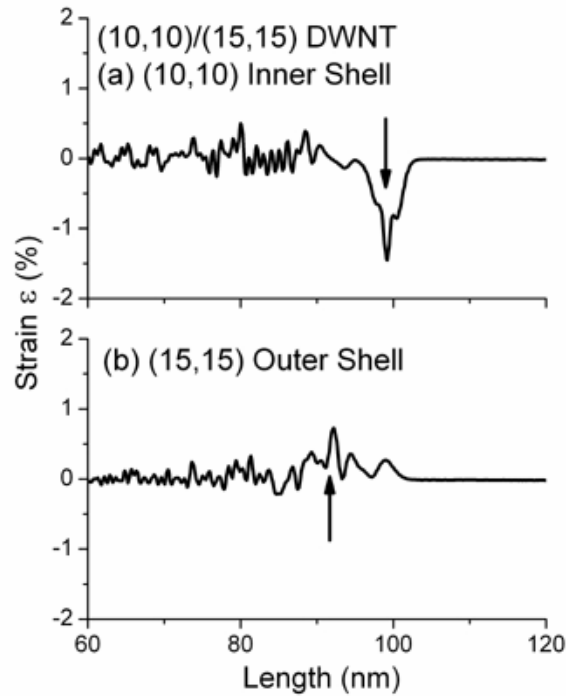


**Figure 5.14** The distribution of strain within the leading wave packets in (10,10)/(15,15) DWNT (a) inner (10,10) shell and (b) outer (15,15) shell.

The peak kinetic temperature of the leading wave packet in the inner shell of the DWNT is about 20 K whereas that of the outer shell is about 1 K. These are similar to the values of the leading wave packet in the smaller (5,5)/(10,10) DWNT. Moreover, the maximum strain within the leading heat wave packets in inner (10,10) shell was ~6 times greater than that of outer shell (15,15). Therefore, for the two DWNTs (i.e. (5,5)/(10,10) and (10,10)/(15,15)) with difference in the inner shell curvatures does not affect the magnitudes of the strain. However, the larger energy and strain in the inner shell compared to the outer shell is due to the asymmetry in the inter-shell van der Waals interaction potential in DWNT arising from the large number of atoms in the smaller

curvature outer shell cells compared to large curvature inner shell cells. For example, the number of atoms per slab in (5,5), (10,10), and (15,15) nanotubes are 40, 80 and 120, respectively. Within the van der Waals potential cut off distance in (5,5)/(10,10) DWNT, each atom in the inner shell interacts with around 63 atoms outer shell atoms whereas an outer shell atom interacts with only about 25 inner shell atoms. This leads to a net inward force (or pressure) on the inner shells [74] which accounts for the higher strain and energies within the peaks associated with LA modes.

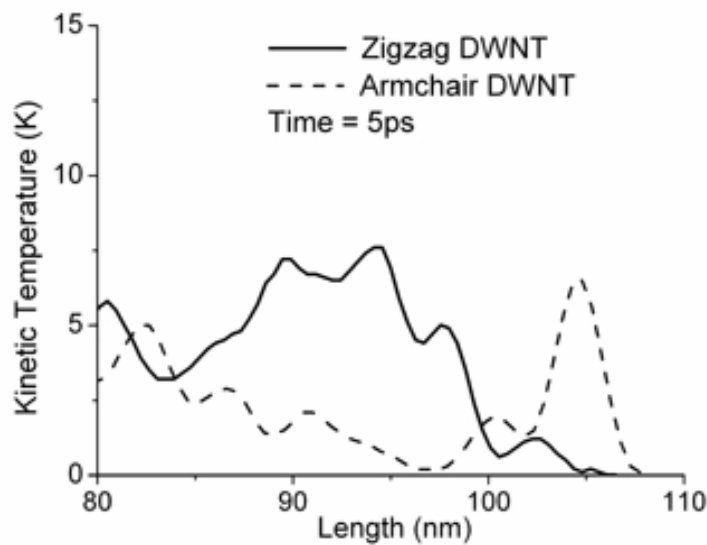


**Figure 5.15** Kinetic temperature of the leading LA mode wave packets in zigzag DWNT (solid line) and armchair DWNT (dashed line).

The kinetic temperatures of the leading LA mode wave packets in the range of 85 nm ~110 nm in the inner shells of the zigzag and armchair DWNTs are shown in Fig. 5.15. Note that the armchair DWNT has a strong heat peak at 105 nm, which is coincident with

the localized strong strain in the inner shell (see Fig. 5.11(a)). On the other hand, the strain in the inner and outer shell zigzag DWNT is strong and spread over a wider region as can be seen in Fig. 5.5, leading to a broader and relatively strong leading heat wave packets. In both zigzag and armchair DWNTs, the energy carried by LA mode wave packets in the inner shells were larger than those in the outer shells. Furthermore, as can be seen in Fig. 5.15, the total kinetic energy carried by the wave packets in zigzag DWNT is 60 meV which is four times larger than the 15 meV kinetic energy for armchair DWNT.

## 5.5 Summary and Conclusion

MD simulations have been used to investigate heat pulse propagation in zigzag (9,0)/(18,0) DWNT, armchair (5,5)/(10,10) DWNT, armchair (10,10)/(15,15) DWNT and the corresponding SWNTs. It is found that the leading heat wave packets in both armchair and zigzag DWNTs propagate at the speed of longitudinal acoustic modes. The intensities of leading heat wave packets in outer and inner shells in DWNTs were found to be five to seven times larger than that of the corresponding SWNTs. The higher energy of the LA mode waves in DWNT shells can be attributed to the presence of higher strain fields in DWNT compared to individual SWNT. The higher strain in the inner shells of DWNT arises from the pressure due to van der Waals interactions and is responsible for the three to five fold higher kinetic energy of leading heat wavepackets in inner shells compared to those in outer shells. The heat energy carried by the leading heat wave packets in zigzag DWNT was about four times more than those in armchair DWNT shells. The induced

strain fields in the outer inner shells of zigzag DWNT were out phase by  $180^\circ$  and distributed over a wider region compared to armchair DWNT.

# CHAPTER SIX

## MOLECULAR DYNAMICS SIMULATION OF CARBON NANOTUBES AND SILICON INTERFACE

### 6.1 Introduction

The thermal interfacial resistance of carbon nanotube with experimental and MD simulation approaches were described in Chapter 4.5. In this research, we examine the interfacial thermal contact resistance between armchair (11,11) CNT and silicon using MD simulations for three different types of interactions between silicon atoms and (11,11)CNT atoms: (1) bonded interaction with sum of non-bonded Si-C interactions and (2) non-bonded bonded interactions (van der Waals interaction) only. The MD simulations are performed at different ambient temperatures and different hot and cold temperatures. The thermal interfacial resistances for each case are calculated as a function of temperature from the temperature discontinuity at the interface. Furthermore, the phonon power spectrum for each case is also calculated from the fast Fourier transform of velocity auto-correlation functions. In addition, the thermal interfacial resistance of zigzag (19,0) SWNT and both armchair (6,6)/(11,11) and zigzag (10,0)/(19,0) DWNTs were examined at  $T=300\text{K}$ .

## 6.2 Methodology

The MD simulation approach is used to investigate heat transfer between CNT and silicon to estimate the thermal interfacial resistance. The Tersoff Brenner bond order potential is used for the simulation of C-C interactions in CNT [18,55,56]. The Si-Si interaction in bulk silicon uses the Tersoff potential with the parameters reported [55,56]. For silicon-carbon interaction, two interactions were applied; (1) The Si-C bonded interaction due to the Tersoff potential [55,56] and (2) the 6-12 Lennard-Jones type van der Waals interaction given by

$$U_{vdW} = \sum_{\text{non-bonded pairs}} 4\varepsilon_{ij} \left[ \left( \frac{\sigma_{ij}}{r_{ij}} \right)^{12} - \left( \frac{\sigma_{ij}}{r_{ij}} \right)^6 \right] \quad (6.1)$$

where  $r_{ij}=|r_i-r_j|$  is the separation distance between carbon and silicon atoms. The Lennard-Jones interaction parameters,  $\varepsilon_{ij}$  and  $\sigma_{ij}$  between silicon and carbon, are calculated by Lorentz-Berthelot mixing rules:

$$\varepsilon_{ij} = \sqrt{\varepsilon_{ii}\varepsilon_{jj}} \quad (6.2)$$

$$\sigma_{ij} = \frac{\sigma_{ii} + \sigma_{jj}}{2} \quad (6.3)$$

where  $\varepsilon_{c-c}=4.41\text{meV}$ ,  $\sigma_{c-c}=3.35\text{\AA}$  for carbon and  $\varepsilon_{\text{Si-Si}}=4.41\text{meV}$ ,  $\sigma_{\text{Si-Si}}=2.28\text{\AA}$  for silicon and the cutoff distance  $r_{\text{cut}}=7.1\text{\AA}$ . The van der Waals interaction plays an important role in

thermal and interface structure stability. The MD simulation approach is used with these interactions to solve Hamilton's classical equations of motions with predictor-corrector algorithms with fixed time step of 0.5 fs.

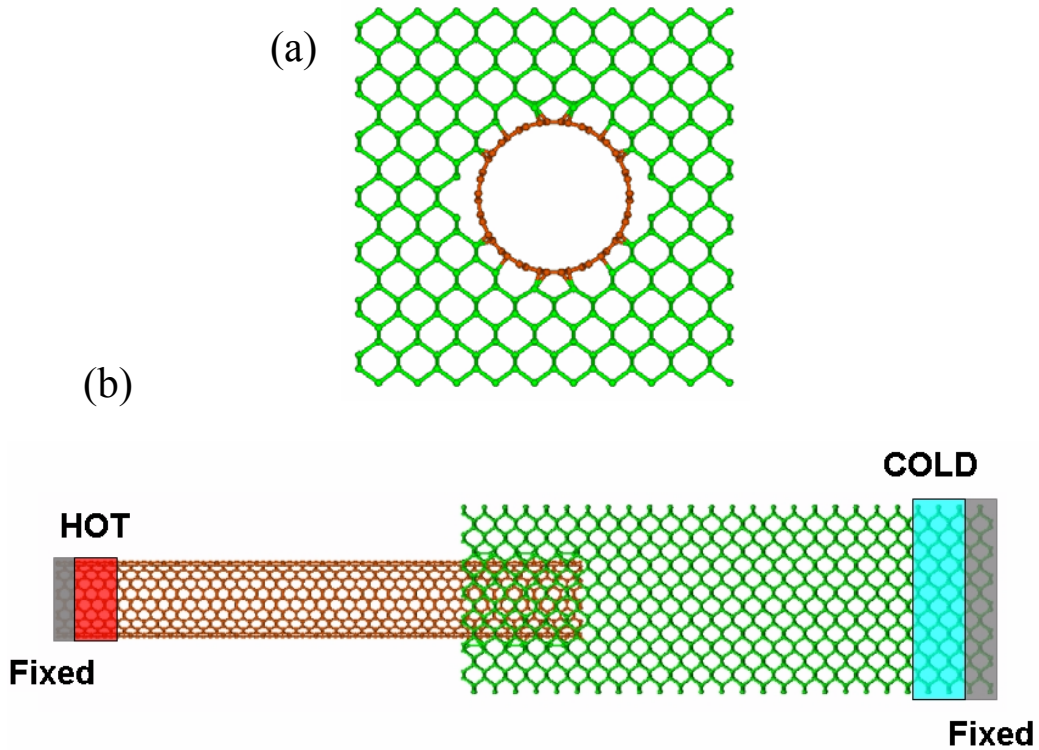


**Figure 6.1.** (a) The cross section of silicon groove which (11,11) SWNT is positioned at the center and (b) side view of the CNT-silicon interface. Both ends (gray) are fixed and 2 slabs in CNT is hot slabs with  $T_{hot} = T_{amb} + 50K$  and 2 slabs in silicon is cold slabs with  $T_{cold} = T_{amb} - 50K$ .

In a CNT thermal switch, a combination of nanotube ends and the sides of bent nanotubes contact the silicon surface during low resistance mode. However, the number of carbon atoms at the nanotube end that can bond to silicon atoms on the surface is very small which makes it difficult to obtain reasonable values for the heat flux in order to

compute the thermal interface resistance. Therefore we opted to align the CNT parallel to the Si(001) surface for our MD simulations of the interfacial resistance between silicon and CNT. The silicon reconstructed  $(2\times 1)$   $(0,0,1)$  surface was used in earlier MD simulations of energetic  $C_{60}$  impact on silicon surface [83] and the investigations of nanoscale etching and indentation of silicon  $(2\times 1)$   $(0,0,1)$  surface with CNT tips [84]. Also using density functional theory calculations structure calculations, the stable atomic geometries for adsorption of  $(5,5)$  armchair CNT on Si $(0,0,1)$  stepped-surface were determined in [60] where they showed that the highest adsorption energy was obtained for  $(5,5)$  armchair carbon nanotube placed between dimer rows on silicon  $(0,0,1)$  surface or at the step edge next to the dimer row. The C-Si bond lengths for these two favorable adsorption sites were 1.97 Å and 2.0-2.05 Å, respectively. In order to increase the number of bonded Si-C pairs, the carbon nanotube was inserted into an etched cylindrical groove in silicon (100) surface as shown in Fig. 6.1. Within the groove the embedded CNT is surrounded by two  $(2\times 1)$  (001) silicon surfaces and 4 step edges. For a groove depth of 2.47 nm and for 2.07 nm long CNT, the number of Si-C atom pairs with inter-atomic separation shorter than the bond cut-off for Tersoff potential were examined for  $(10,10)$  and  $(11,11)$  armchair carbon nanotubes centered within the groove. The bond length distributions are shown in Fig. 6.2. As can be seen in Fig 6.2, the  $(11,11)$  armchair CNT has 94 silicon-carbon atom pairs with inter-atomic separations that fall within the cut-off distance of Tersoff's potential compared to 29 pairs only for the  $(10,10)$  armchair CNT. It is interesting to note that the majority of C-Si bond lengths for the  $(11,11)$  CNT fall within the calculated bond length corresponding to the favorable sites reported in [60].

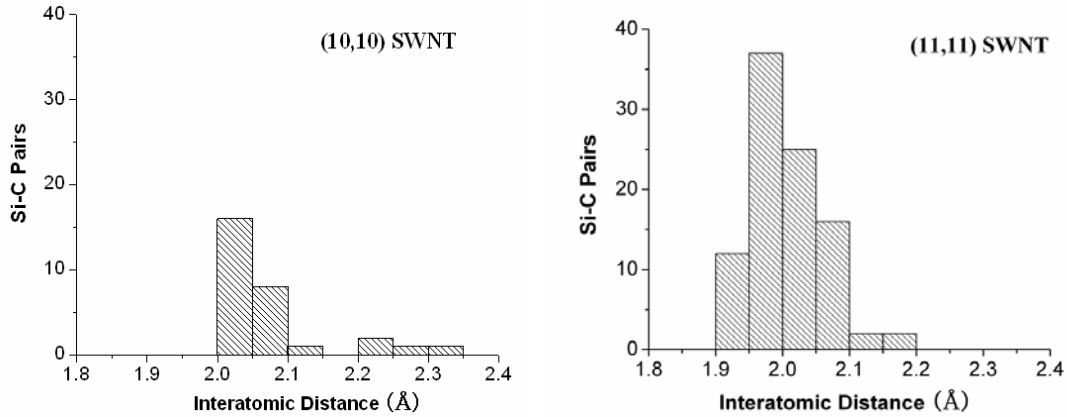


**Figure 6.2** The distribution of bonded pairs of (a) (10,10) SWNT and (b) (11,11) SWNT in the silicon groove.

For the MD simulations of bonded interaction between CNT and silicon, a 10 nm long silicon sample with 3.84 nm×3.84 nm cross-section is used. The sample has a cylindrical groove of 1.86 nm diameter and 2.47nm depth bored in one of its cross-sections. The length of the (11,11) armchair SWNT is 9.84 nm. In calculating bonded interactions, the Si-C bonded pairs are excluded from van der Waals interactions calculation [85]. For the MD simulations of the thermal interfacial resistance due to non-bonded interaction only, the cylindrical groove is widened to increase the inter-atomic spacing between silicon and carbon atoms beyond the cut-off length for bonded Si-C tersoff potential. The cross-sectional silicon is also increased to 4.6nm×3.84nm.

Both CNT and silicon are divided into slabs of uniform width along the length of the sample. To stabilize the structure during the simulation, both end slabs of CNT and silicon

are fixed, where as periodic boundary conditions are applied to silicon structure in the direction perpendicular to nanotube axis.

The MD simulations involved an initial quenching of the whole structure to 0K using 20,000 MD time steps followed by heating up to the desired temperature (100 K) where equilibrium is achieved after 200,000 MD time steps before applying any temperature gradients. The temperature is increased at increments of 50K from 100 K to 300K followed by 200,000 MD time steps at each intermediate temperature to achieve equilibrium temperature distribution in the structure. During heat flow simulation, the temperatures in the two slabs next to the fixed end slab in each material are regulated to achieve the desired hot and cold regions required for maintaining a temperature gradient in the system. The temperatures of the hot and cold slabs were regulated by scaling the velocity of the atoms within each slab as follows

$$v_{i,new} = v_{i,old} \sqrt{\frac{T_{control}}{T_{current}}} \quad (6.4)$$

where  $T_{control}$  is the desired temperature and  $T_{current}$  is the current temperature of the slabs. For the hot slab,  $T_{control}=T_{amb}+\Delta T$  and for the cold slab,  $T_{control}=T_{amb}-\Delta T$ , where  $T_{amb}$  is the initial equilibrium temperature of the system and  $\Delta T=50K$ . The temperature drop at the interface with bonded interaction is 50K~65K depending on the temperature, and the temperature drop of non-bonded interaction is ~95K. in order to cover these temperature

range,  $\pm 50\text{K}$  temperature was applied. The heat flux in a thermally equilibrated segment is calculated from the change of energy in control slabs at each time step using the following expression:

$$J = \frac{\left\langle \frac{1}{2} m \sum_{i=1}^N (v_{i,new}^2 - v_{i,old}^2) \right\rangle}{\Delta t} \quad (6.5)$$

where  $N$  is the number of atoms in the hot or cold slabs,  $m$  is the mass of carbon or silicon, and  $v_{i,new}$  is calculated using equation (6.4). The heat flow simulation uses 300,000 MD time steps and both the heat flux  $J$  and the steady state temperature profile along the sample are calculated by time averaging over the final 100,000 steps. The discontinuity in the temperature at the interface between silicon and CNT ( $T_{drop}$ ) is calculated by averaging the temperature differences between overlapping slabs in silicon and CNT within the groove. The thermal interfacial resistance ( $R_{TIR}$ ) is given by

$$R_{TIR} = \frac{A \cdot T_{drop}}{J} \quad (6.6)$$

where cross sectional area  $A$  is given by [86,87]

$$A = 2\pi \left( R_{NT} + \frac{h_{vdW}}{2} \right) L_{NT} \quad (6.7)$$

where  $R_{NT}$  is the radius of CNT,  $L_{NT}$  is the length of embedded CNT in the silicon groove

and  $h_{vdW}$  is the average interfacial separation, which is set to zero for bonded interaction.

### 6.3 Results and Discussion

Heat flow at ambient temperature ( $T_{amb}=300K$ ) from CNT with one end maintained at  $T_{hot} = T_{amb} + 50K$  to silicon with temperature at one end maintained at  $T_{cold} = T_{amb} - 50K$ , as shown in Fig. 6.1, has been investigated using MD simulations. The desired temperatures  $T_{hot}$  and  $T_{cold}$  of the hot and cold slabs, respectively, were maintained using velocity scaling method. At each ambient temperature, 200,000 MD time steps are used to achieve equilibrium and 300,000 MD time steps to evaluate the heat flux and temperature drop between CNT and silicon.

The temperature profile along the CNT and silicon structure at 300K with, non-bonded and bonded interactions are plotted in Fig. 6.3. At the CNT-silicon interface, temperature profile shows a sharp discontinuity due to the thermal interfacial resistance. The temperature drop for the bonded interactions cases was around 53K as can be seen in Figs. 6.3(a). On the other hand, a significantly larger temperature drop of 99 K is obtained for the case involving only non-bonded van der Waals interaction. (the spacing between CNT and silicon groove for non-bonded interaction is  $3.0\text{\AA}$ ). The simulations were repeated at 250K, 200K, 150K and 100K. For each temperature, the temperature drop at the interface, heat flux and thermal interface resistance were calculated following the procedure discussed in simulation method.

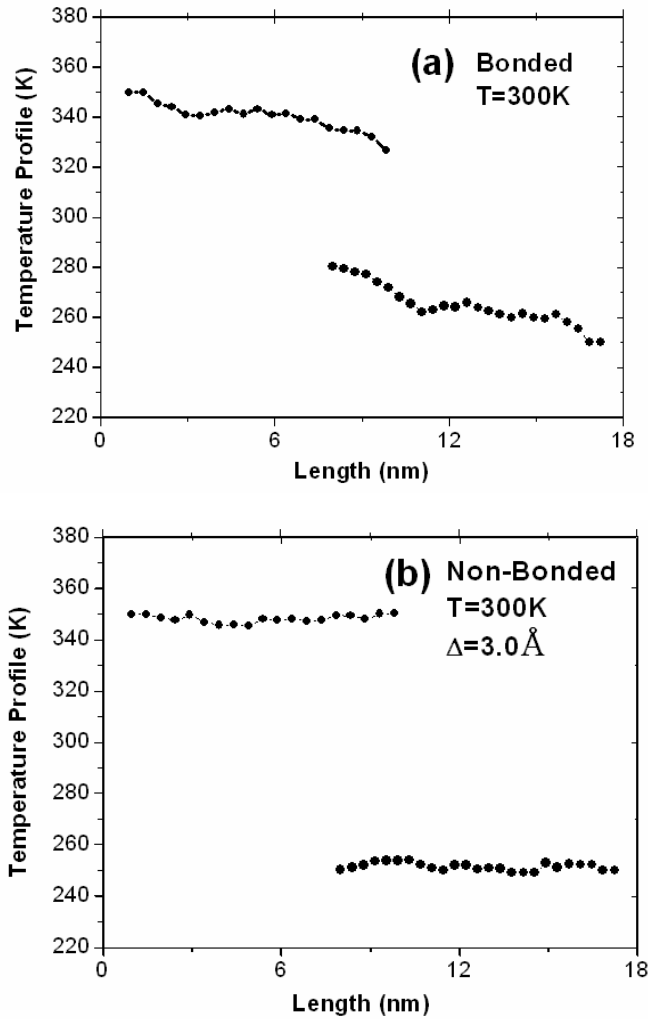


**Figure 6.3** Temperature profile of (a) bonded interaction and (b) non-bonded interaction.

The dependence of the thermal interfacial resistance on temperature is shown in Fig. 6.4. For the bonded interaction case, the thermal interface resistance decreases as the temperature increases due to increase in heat flux as result of increased phonon population and phonon coupling at the interface at higher temperatures [88]. The details of phonon

couplings and their contribution on heat flow across the interface will be discussed later on this paper. The calculated thermal interface resistance at room temperature for the silicon-CNT with bonded Si-C pairs is  $2.85 \times 10^{-9} \text{ m}^2\text{K/W}$ .

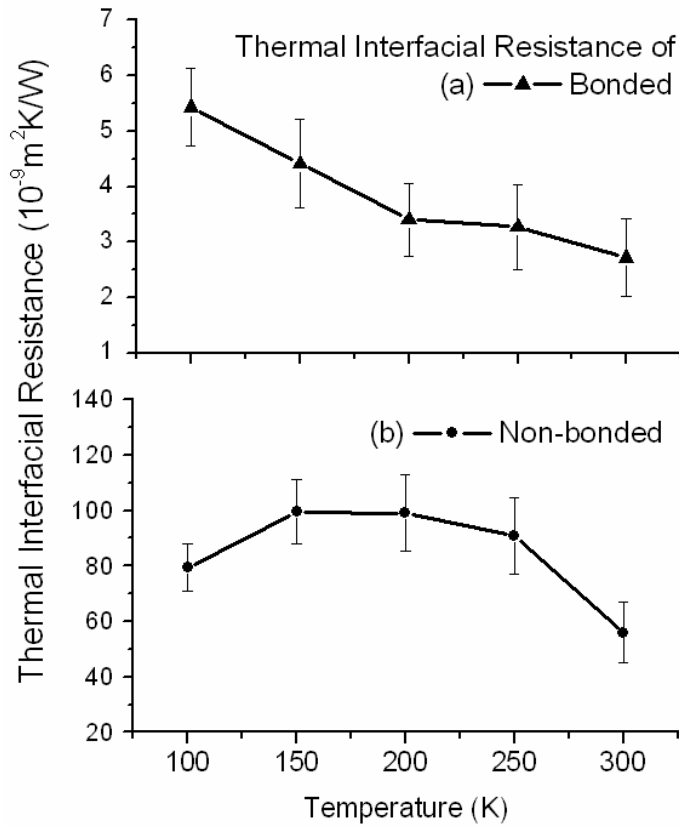


**Figure 6.4** Thermal interfacial resistance of (a) bonded interaction and (b) non-bonded interaction.

The thermal interfacial resistance of non-bonded interaction at 300K is  $5.6 \times 10^{-8} \text{ m}^2\text{K/W}$ , which value is close to the interfacial resistance of two CNTs [52]. The discrepancy between MD simulation results and experimental results is caused by the

distance at the contact. In MD simulation, the distance between surfaces is few Å, however, in the experiment, is ranges for few nm to 100nm due to the surface roughness. Zhong et al results shows that as the separation between CNT increases to 1nm, thermal interfacial resistance increases to  $5.6 \times 10^{-6} \text{m}^2\text{K/W}$ .

For overall temperature range, non-bonded interaction has ~20 times greater average thermal interfacial resistance than bonded interaction for overall temperature.

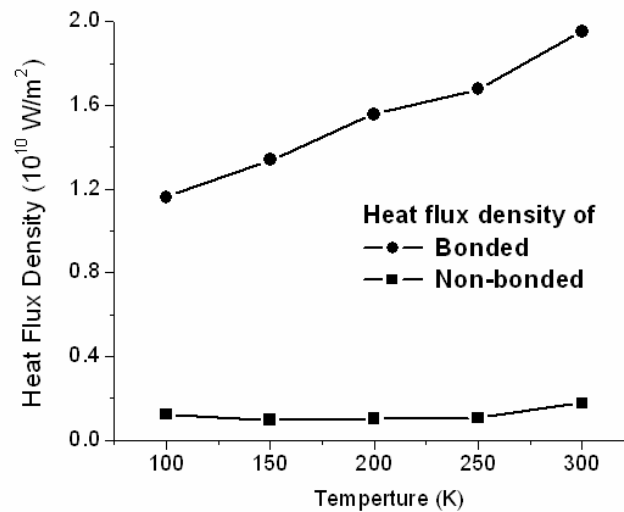


**Figure 6.5** Heat flux density of bonded interactions and non-bonded interaction

The heat flux energy density of two cases at the steady state heat flow is plotted at Fig. 6.5. The bonded interaction has larger heat flux energy density than the non-bonded interaction. This results show the minor role of non-bonded interaction in heat transfer at the interface. For overall temperature range, the average heat flux energy of bonded interactions is 11 times greater than that of non-bonded interaction. The temperature dependence of heat energy can be explained by phonon population increase and phonon

coupling at the interface between two materials. Baowne et al have investigated the thermal interfacial resistance between two dissimilar anharmonic lattices [88]. As the temperature increases, the phonon coupling between two materials increases and results in more heat flow at the interface. This is also the main reason of smaller thermal interfacial resistance at high temperature. On the other hand, the heat flux density on the non-bonded interaction shows different mechanism. At low and high temperatures, the heat flux density is greater than middle range temperature. The heat transport in non-bonded interaction does not depend on the phonon coupling or excitation materials (which is discussed later), the heat flux density may more depend on each material's thermal properties itself. The thermal conductivity of pure bulk silicon reaches maximum value near 100K and decreases rapidly with temperature. The thermal conductivity of CNT, however, gradually increases and reaches maximum at 300K. Therefore, the heat transport across the interface depends on thermal conductivity of silicon at low temperature and that of carbon nanotube at room temperature.

The contact groove geometry of our interface is optimized in bonded and non-bonded interactions and designed to examine the best condition for the heat flow between CNT and silicon interface. The discrepancy between numerical and experimental thermal interfacial resistance was also reported by Zhong et al [17]. They reported MD simulation based thermal interfacial resistance between two straight (10,10) SWNTs. As the space between two CNT increased 0~8 Å, thermal interfacial resistance increases in the order of  $10^{-8} \text{m}^2\text{K/W}$ .

The phonon power spectrum was also different for separated parts of the system to understand phonon modes at the interface. The phonon spectra are obtained by taking the Fourier transform of the velocity autocorrelation function.

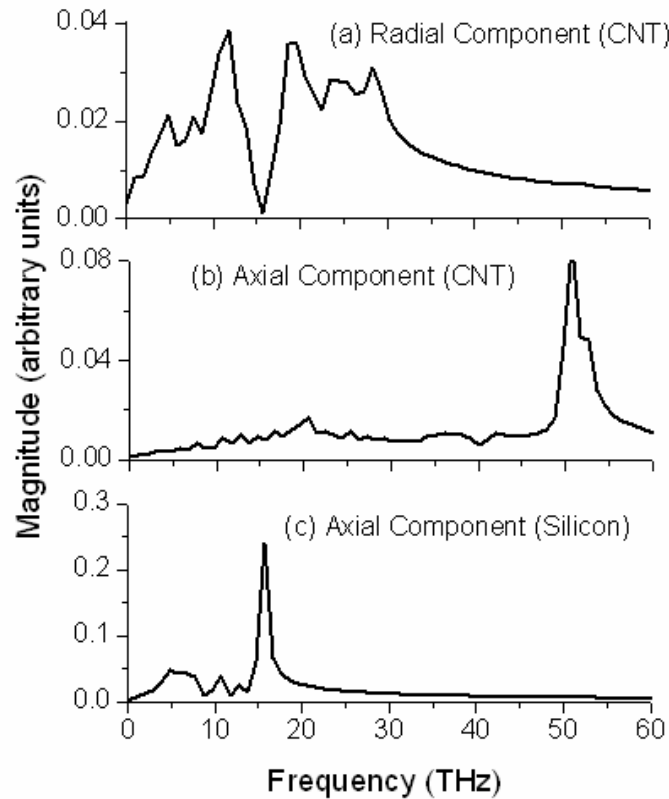


**Figure 6.6** The phonon power spectrum of silicon and CNT ends: (a) radial component (CNT), (b) axial component (CNT) and (c) axial component (silicon)

In order to see the phonon behavior at the interface and compare them with other parts of the system, velocity auto-correlation functions are calculated for 4 CNT slabs inside silicon groove, 4 CNT slabs next to the fixed CNT slabs, 4 silicon slabs surround the

groove, and 4 silicon slabs next to the fixed silicon slabs. Of interest are the frequency distributions of atomic vibrations along radial, azimuthal and axial components for CNT and for the silicon. To compare the phonon behavior with bonded interaction, the auto-correlation functions are calculated for the same regions of the structure which only non-bonded interaction is applied.

At first, the radial and axial components of 4 CNT slabs next to the fixed slabs are calculated and plotted at the Fig. 6.6 (a) and (b). (The azimuthal phonon component is not shown since it has almost the same pattern as the axial component). The axial component of 4 silicon slabs next to fixed slabs are plotted at the Fig. 6.6 (c). These phonon spectra for each phonon component in CNT and silicon is the same with their isolated systems. [89, 90, 91].

The phonon spectra of 4 CNT slabs inside silicon groove have different behavior as shown in Fig. 6.7 (a) and (b). In the radial mode, the absence of phonon spectra at 15THz is disappeared This brings that the population of radial phonon at the interface is increased under the silicon-carbon bonded interaction. The other important change is the excitation of phonon spectra near 5 THz, which corresponds to the radial breathing mode (RBM) of (11,11). In recent researches, it was found that the low frequency radial mode the major phonon mode in transporting heat across the interface of CNT and with other materials [90,92]. When the other molecules attached inside and outside CNT, high frequency the tangential or axial phonon modes do not participate on heat flow. But the low frequency radial vibration mode based on the RBM transport heat across the interface. The radial phonon spectra of 4 CNT slabs in silicon groove where only non-bonded interaction is

applied also strongly support the role of radial mode as shown in Fig. 6.7(c). Compared to the radial phonon mode of the bonded interaction, non-bonded interaction radial phonon mode does not change any radial modes of isolated CNT.

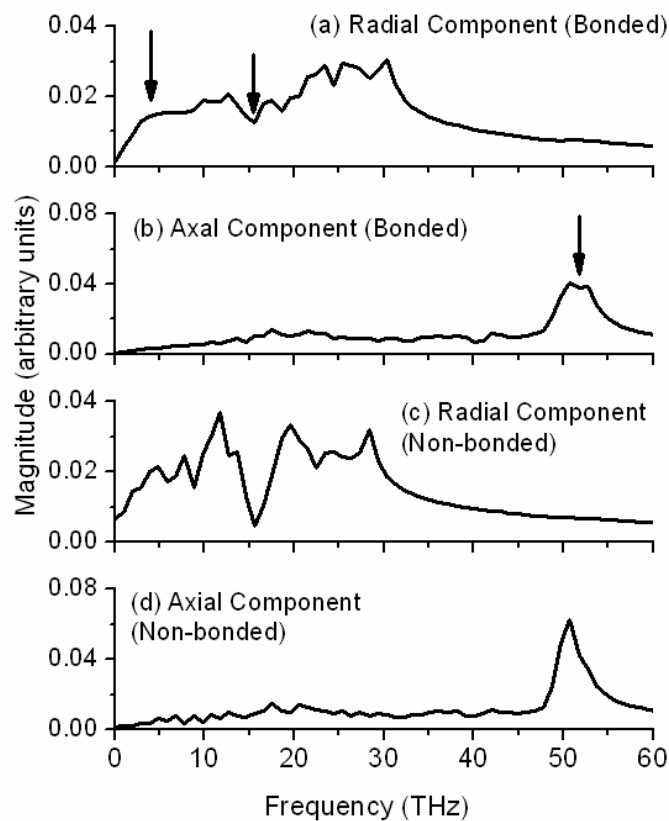


**Figure 6.7** The phonon power spectrum of CNT inside silicon groove: (a) radial component, (b) axial component in bonded interactions, (c) radial component in non-bonded interaction and (d) axial component in non-bonded interaction.

There is obvious difference at high frequency phonon spectra between bonded and non-bonded interaction. The sharp phonon peak at 50THz in Fig. 6.5 (b) is due to the high

frequency graphitic in-plane stretching mode (G-band) and the disorder-induced mode (D-band) [89]. Clifford et al reported that the peak of this mode decreases and broadening as the functionalization of chemical attachments increases due to the change of  $sp^2$  bonded carbon to  $sp^3$  [93]. The same mechanism explains the reduced phonon peak at Fig. 6.7 (b). The change of  $sp^2$  of carbon bond to  $sp^3$  by silicon–carbon bonding inside silicon groove causes to reduce and broaden the phonon spectra at 50THz. However, the phonon peak at 50THz of non-bonded interaction in Fig. 6.7(d) does not show any change inside silicon groove from that of the outside.

The phonon behavior of silicon around groove under the bonded interaction is plotted at Fig.6.8 (a). Compared to the phonon spectra of isolated silicon, the shape of 5THz is almost the same. However, the phonon peak at 15THz is reduced compared to the phonon peak at Fig. 6.6(c). This phonon behavior is caused by the dimer rows on the silicon groove surface. At the silicon surface, which covered by silicon dimer rows, the phonon peaks near 15THz are almost disappeared [94]. In addition, since most silicon atoms in phonon modes are not affected by silicon-carbon bonding (94 silicon atoms bonded out of 1190 silicon atoms in groove region) whereas 94 carbon atoms bonded with silicon out of 352 carbon atoms inside silicon groove, the phonon spectra of silicon with bonded interaction (Fig. 6.8(a)) and non-bonded interaction (Fig. 6.8(b)) are almost identical.

The decrease of thermal interfacial resistance with temperature has been reported by Robert et al and Twu et al [50,95]. This dependence of thermal resistance on temperature was also reported between nonmetal (Si) and metal (Cu) contact by Prasher et al [96]. The temperature dependence on thermal interfacial resistance was also measured experimentally

[97,98]. Theoretically, these results can not be expected by the mismatch model, since it predicts temperature independent thermal interfacial resistance above the Debye temperature. In the classical limit, the inelastic scattering contributes heat energy transport across interface rather than elastic scattering does above the Debye temperature.

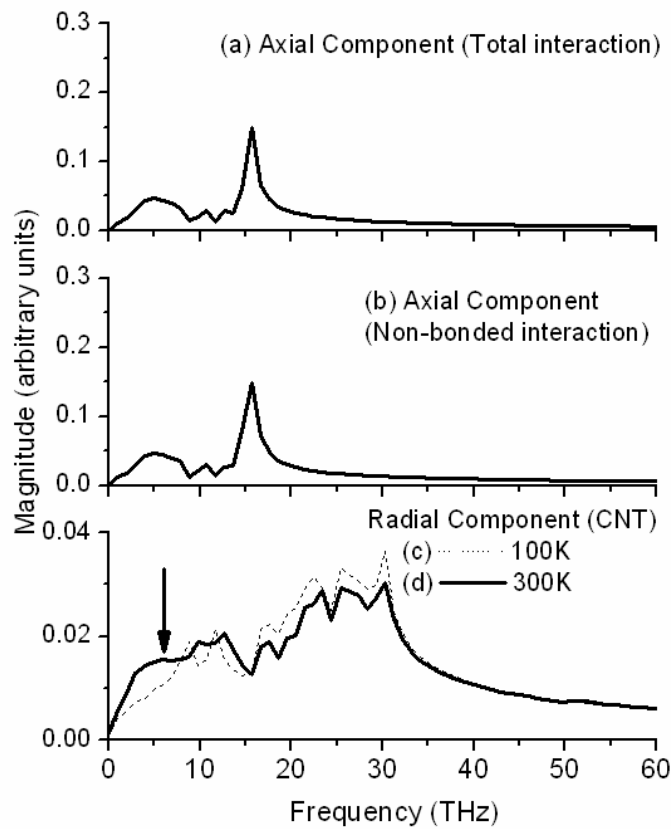


**Figure 6.8** The phonon spectrum of silicon groove in (a) bonded interaction and (b) non-bonded interaction. The radial phonon power spectrum of CNT in groove with bonded interactions at (c) 100K and (d) 300K.

The scattering process is proportional to the phonon population, which linearly increases with temperature at high temperature [50]. Recently the heat transport between

CNT and surrounding liquid was studied to understand the thermal interfacial resistance between CNT and liquid. In their research, the low frequency bending and squeezing phonon modes are strongly coupled with the liquid. However, low frequency twisting and longitudinal mode are coupled very weakly [92]. On the other hand, the heat energy transport of CNT which encloses  $C_{60}$  can be account for the excitation of low-frequency radial phonon modes and the coupling of the radial mode with the longitudinal mode in the low-frequency region [90]. The heat transport across CNT and silicon interface discussed so far shows the same mechanism. At high frequency phonon modes, there is no phonon mode coupling observed. However, at low frequency below than 16THz, the radial phonon mode in CNT was excited due to the phonon coupling with silicon as shown in Fig. 6.7 (a). However, it is already mentioned that no phonon interaction at low frequency is obtained in the non-bonded interaction system. Meanwhile, the excitation of radial mode also explains the increase heat flux density with temperature. The radial breathing mode (RBM) of (11,11) SWNT is near 5THz [99] and Fig. 6.8(c) show that the RBM of (11,11) inside silicon groove is more excited at 300K than 100K. In addition, the radial modes which are lower than 15THz is comparably more populated than 100K. Therefore, more heat energy is transported due to the RBM and near radial modes as temperature increases even though higher frequency phonon modes are slightly attenuated at 300K.

#### **6.4 Thermal Interfacial Resistance of Zigzag SWNT and DWNTs.**

The thermal interfacial resistance of zigzag SWNT at 300K was calculated to examine the effect of chirality on thermal interfacial resistance. (19,0) SWNT was chosen due to the similar diameter (1.506nm) with that of (11,11) SWNT (1.51nm). Since the slab size of zigzag CNT is 0.426nm, whereas armchair CNT has 0.492nm, 23 slabs of (19,0) SWNT was used. Therefore, the length of 23 slabs of (19,0) CNT is 9.8nm and the length of (11,11) CNT is 9.83nm. Meanwhile, the same size of silicon with same groove was used for MD simulation. The structure of (19,0) CNT with silicon structure is plotted in Fig. 6.9. The MD simulations involved an initial quenching of the whole structure to 0K using 20,000 MD time steps followed by heating up to the desired temperature (100 K) where equilibrium is achieved after 200,000 MD time steps. The temperature is increased at increments of 50K from 100 K to 300K followed by 200,000 MD time steps at each intermediate temperature to achieve equilibrium temperature distribution in the structure.

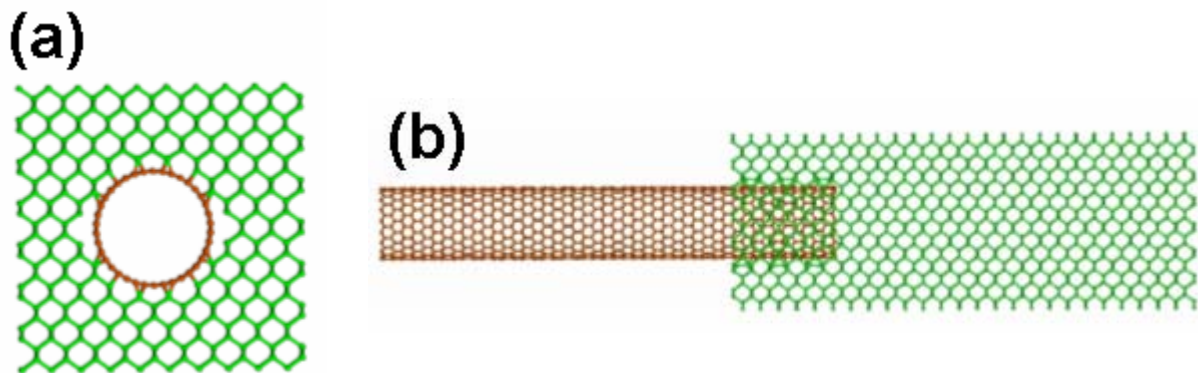


**Figure 6.9** (a) The cross section and (b) the side view of (19,0) SWNT in the silicon groove and structure of (19,0) SWNT. The diameter and length of (19,0) CNT is 1.506nm and 9.83nm, respectively.

Thermal interfacial resistance was calculated by same simulations procedures used

in (11,11) SWNT case. The number of bonded C-Si pairs of (19,0) SWNT in silicon groove is 90. The temperature profile of (19,0) SWNT with silicon is plotted in Fig. 6.10. The temperature drop at the silicon-CNT interface is 56.32, which is almost the same with temperature drop of (11,11) SWNT. Since the diameter of (19,0) SWNT is the same with (11,11) SWNT, the same cross sectional area was used to calculate thermal interfacial resistance. The thermal interfacial resistance of (19,0) SWNT at 300K is  $3.34 \times 10^{-9} \text{ m}^2\text{K/W}$ . This result is 1.17 times greater than thermal interfacial resistance of (11,11) SWNT.

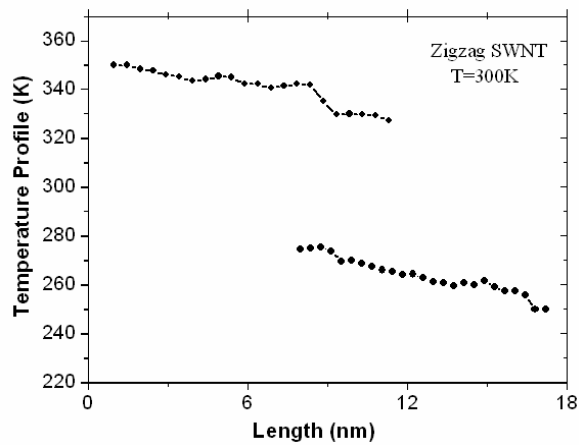


**Figure 6.10** Temperature profile of (19,0) SWNT and silicon at T=300K.

In order to investigate the effect of CNT shell on the thermal interfacial resistance, both armchair and zigzag DWNTs were used. Since the outer shells fit the silicon groove, smaller inner shells were placed into the (11,11) and (19,0) CNTs. Therefore, armchair DWNT consists of (6,6)/(11,11) and zigzag DWNT consists of (10,0)/(19,0). The diameters of (6,6) and (10,0) CNTs are 0.79 and 0.82nm respectively and the inter distance between inner and outer shells are 0.35nm and 0.34nm each. Before the MD simulation of thermal

interfacial resistance started, the energy minimization of each DWNT was performed first. In order to compare the cases of SWNTs, the same length of DWNTs were used for the same size of silicon. The number of bonded Si-C pairs in armchair DWNT was 94 and bonded Si-C pairs of zigzag DWNT was 90. Therefore, the bonded pair numbers of both DWNTs are the same with those in DWNTs. The structures of both DWNTs are plotted in Fig. 6.11.

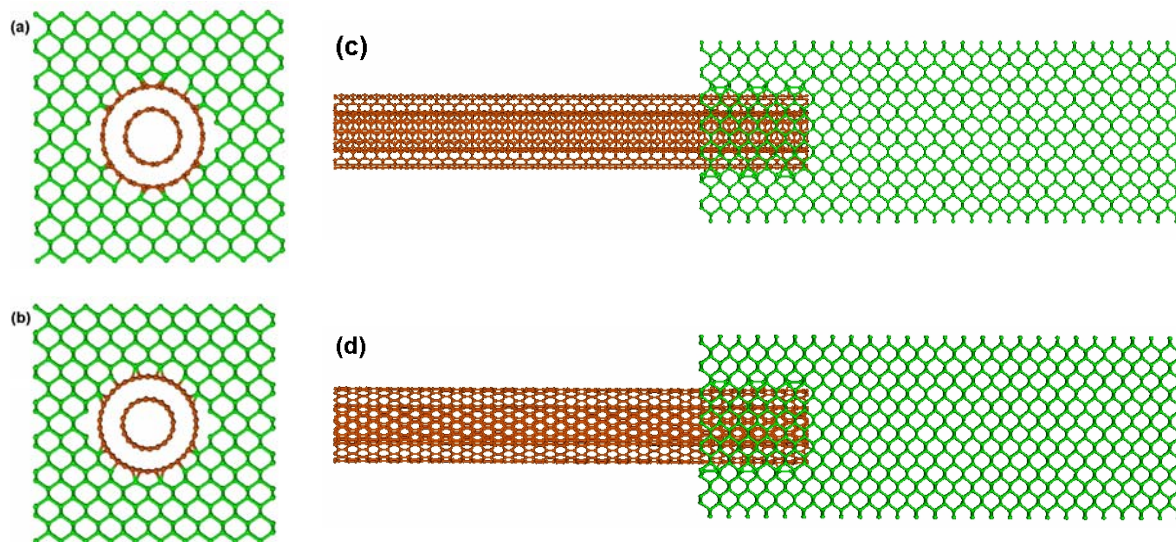


**Figure 6.11** The cross section of (a) armchair (6,6)/(11,11) DWNT, (b) zigzag DWNT (10,0)/(19,0), the side view of (c) armchair (6,6)/(11,11) DWNT, (d) zigzag DWNT (10,0)/(19,0). The length of both DWNTs are 9.83nm and 9.8nm respectively.

The simulation procedures for MD simulation in DWNTs are the same with those of SWNTs. Thermal interfacial resistance at 300K was examined and compared with thermal interfacial resistance with SWNTs. The temperature profiles of both DWNTs are plotted in Fig. 6.12. Temperature drop of armchair DWNT was 55.7K which is almost the same when

(11,11) SWNT was used.. The temperature of zigzag DWNT was 60K, which is 3.5K higher than (19,0) SWNT was used. For the both DWNTs, the temperature profile of inner CNT is higher than average and overall temperatures.

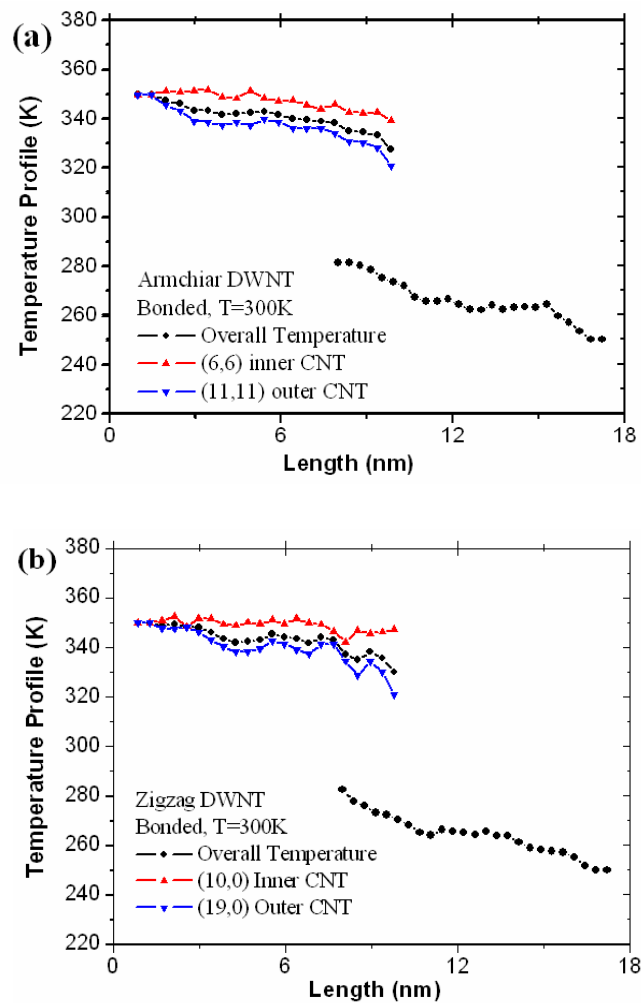


**Figure 6.12.** Temperature profile of (a) (6,6)/(11,11) DWNT and (b) (10,0)/(19,0) DWNT with silicon at  $T=300\text{K}$ .

Thermal interfacial resistance of armchair and zigzag DWNT was  $2.7 \times 10^{-9} \text{m}^2\text{K/W}$  and  $3.1 \times 10^{-9} \text{m}^2\text{K/W}$  respectively and these values are only less than 10 % smaller than

thermal interfacial resistance with SWNTs. The mechanism behind small improvement of thermal interfacial conductance in DWNTs is minor contribution of heat flow in the inner CNT. The inter distance between inner and outer CNT is  $\sim 0.35\text{nm}$  and the distance between outer shell and silicon groove is  $\sim 0.3\text{nm}$ . The distance between inner CNT and silicon groove is  $\sim 0.65\text{nm}$ , which is close to the cutoff distance of Si-C van der Waals interaction ( $0.7\text{nm}$ ). Therefore, the main heat flow from the inner CNT to silicon takes place via the interaction between inner and outer shell, which is van der Waals interaction and majority of heat flow from DWNT to silicon relies on the bonded interaction between outer CNT and silicon. During the steady state heat flow in armchair DWNT,  $15.1\text{eV}$  of energy was delivered into the hot slabs in the inner CNT while  $57.3\text{eV}$  of energy was delivered into the hot slabs in the outer CNT. For zigzag DWNT,  $10.7\text{eV}$  and  $54.3\text{eV}$  of energy were delivered into the hot slabs in inner and outer CNTs.

## **6.5 Thermal Interfacial Resistance of (5,5) CNT Bundle**

The heat transport of carbon nanotube bundle across the silicon interface was also investigated. (5,5) CNT bundle with length of  $9.8\text{nm}$  is inserted into large silicon groove as shown in Fig. 6.13. The angular separation between CNT shells is  $60^\circ$  and the separation distance between center and surrounded CNTs is  $0.34\text{nm}$ . Two carbon nanotubes are bonded on the silicon dimers at top and bottom of the silicon groove. Other four carbon nanotubes are bonded on silicon step edges. The center carbon nanotube has no bonding on the silicon.

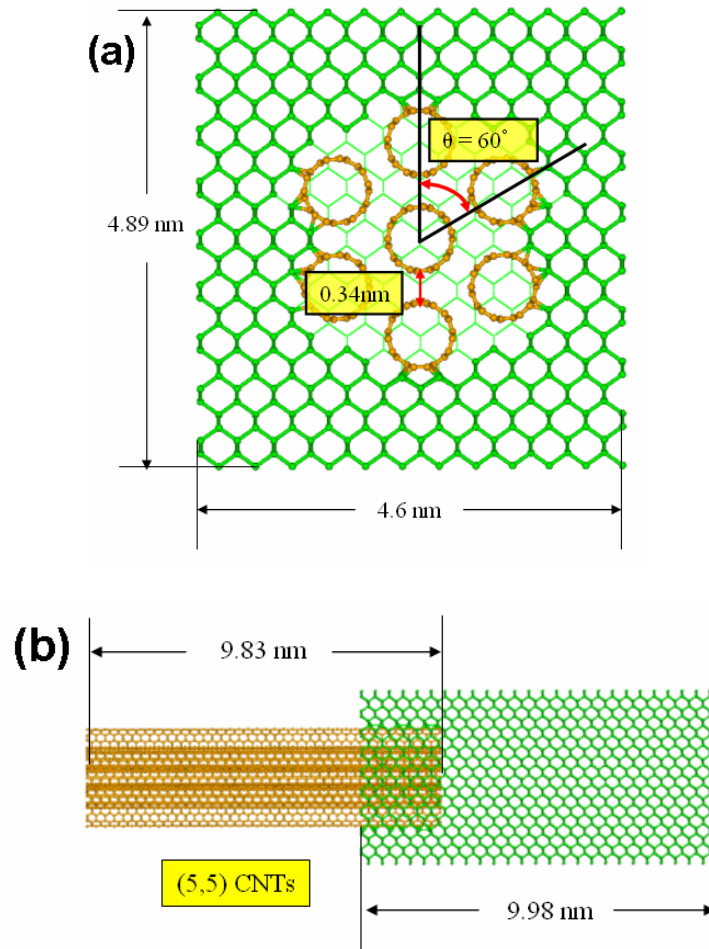


**Figure 6.13** The cross section of (a) (5,5) CNT bundle inside silicon groove and (b) side view of (5,5) CNT bundle with silicon

The C-Si bonded pairs inside silicon groove is 104. The MD simulation was used for the thermal interfacial resistance of CNT bundle and silicon at 100K and 300K. Thermal interfacial resistance at 100K and 300K are  $7.1 \times 10^{-9} \text{m}^2\text{K/W}$  and  $4 \times 10^{-9} \text{m}^2\text{K/W}$  respectively. Compared to the thermal interfacial resistance of (11,11) SWNT with same

length of silicon, these values are 25% greater.

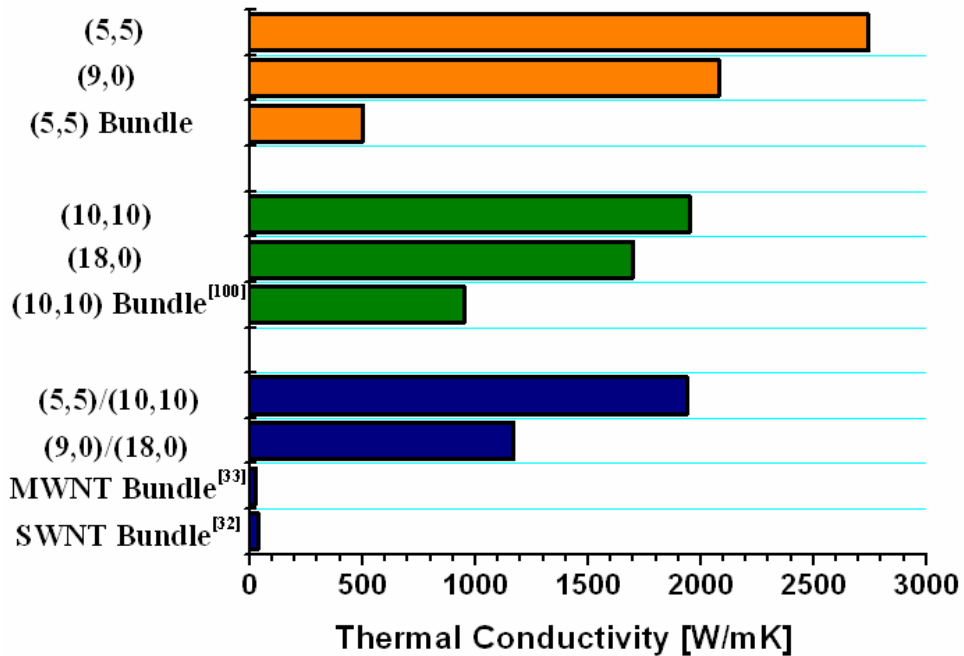


**Figure 6.14** Thermal conductivity of SWNT, DWNT and CNT bundles All these results are calculated by Fourier law with MD simulation except (10,10) bundle, MWNT bundle and SWNT bundle [32,33,100].

Thermal conductivity of armchair and zigzag SWNTs, DWNTs and CNT bundles at 300K are plotted in Fig. 6.14. Compared to the thermal conductivity of SWNTs, thermal conductivity of (5,5) SWNT bundle was calculated as 75% smaller by Fourier method and 50% smaller by Green-Kubo method [100]. In addition, the measured thermal conductivity of CNT bundles is ~30W/mK [32,33]. Therefore, the low thermal conductivity of CNT bundle is responsible for the high thermal interfacial resistance of CNT bundle.

The effect of different interface on thermal interfacial resistance was also investigated

with (1) two parallel (11,11) SWNTs, (2) two (0,0,1) silicon surfaces and (3) CNT-plain (0,0,1) silicon surface. The length of (11,11) SWNT is 9.8nm and the separation between CNTs is 0.35nm with 0.25nm. Two  $1.53\text{nm} \times 1.53\text{nm} \times 10.6\text{nm}$  are aligned along the z axis with separation of 0.256nm between (0,0,1) silicon surfaces. 9.8nm of (11,11) CNT is placed 0.32nm above (0,0,1) silicon surface with 0.25nm overlap. All three interfaces are plotted in Fig. 6.15.

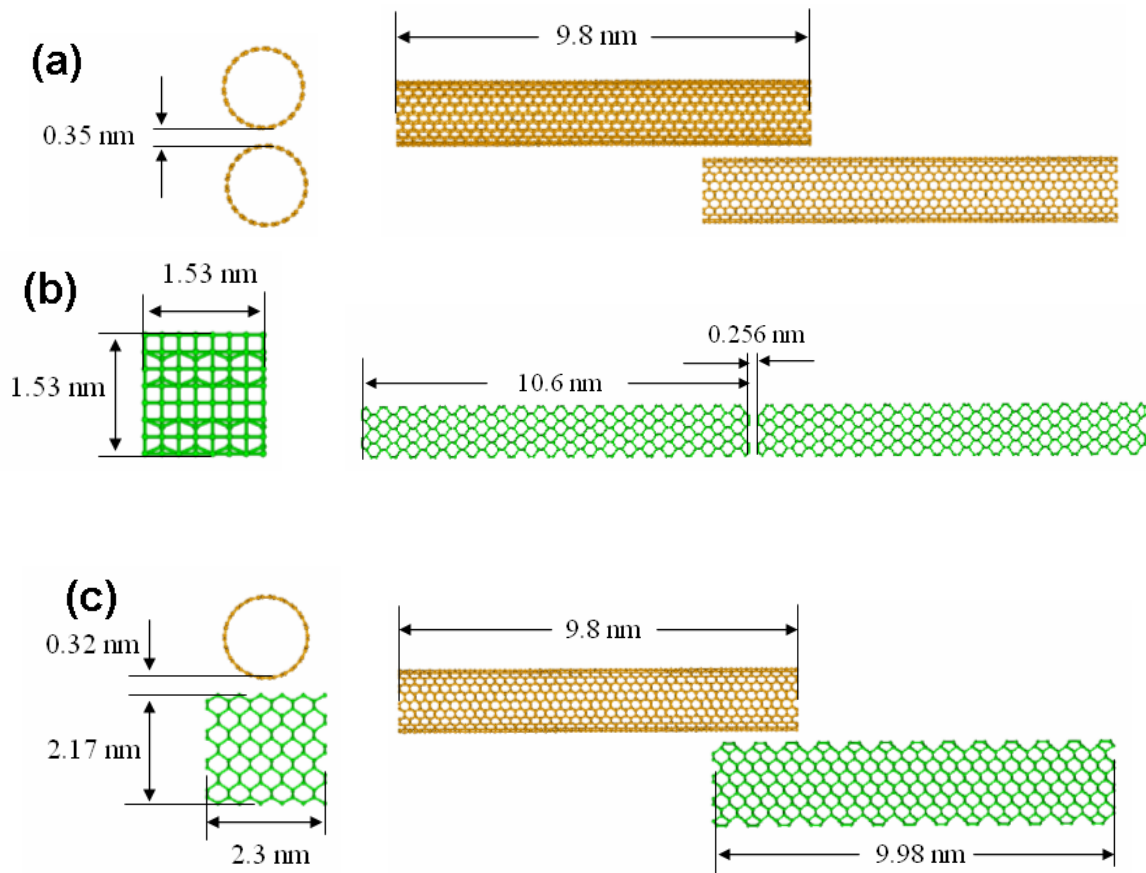


**Figure 6.15** Three interfaces of (a) two (11,11) CNTs, (b) silicon-silicon (0,0,1) surfaces and (c) (11,11) CNT-silicon (0,0,1) surfaces.

The separation distances of three interfaces are the equilibrium distance of van der Waals interaction between each material. All MD simulation were performed at 350K and temperature gradient between hot and cold slab at each material ends was  $\pm 50\text{K}$ . The thermal interfacial resistance of CNT-CNT, CNT-Si and Si-Si are  $3.1 \times 10^{-8} \text{m}^2\text{K/W}$ ,  $2.5 \times 10^{-8} \text{m}^2\text{K/W}$ , and  $1.2 \times 10^{-8} \text{m}^2\text{K/W}$ .

## 6.6 Summary and Conclusion

In summary, MD simulation modeling for the CNT and silicon interface was developed by inserting CNT tip into the bored silicon groove. For non-bonded and bonded interactions, the temperature drops at the interface due to the thermal resistance were calculated. The thermal interfacial resistance for case the bonded interaction was found to be smaller thermal resistance than that of non-bonded interaction case. From the phonon spectrum analysis, it was shown that the low frequency radial phonon modes in CNT were excited due to the coupling with silicon phonon modes and they contributed heat energy transport across the interface. The excitation of the radial breathing mode (RBM) increased with temperature leading to more heat transport more heat energy across the interface and lower thermal interfacial resistance.

Additionally, the thermal interfacial resistance of zigzag SWNT, armchair and zigzag DWNTs with silicon interface were calculated. The thermal interfacial resistances of zigzag SWNT and DWNT are 1.15 times greater than those of armchair DWNTs. The thermal interfacial resistance was slightly improved ( $\leq 10\%$ ) with DWNTs. The participation of inner CNT in heat flow across the interface is very small due to weak van der Waals

interaction with large distance between inner CNT and silicon ( $\sim 0.55\text{nm}$ ).

Thermal interfacial resistance of (5,5) CNT bundle with silicon interface was calculated as 25% greater than (11,11) SWNT for both 100K and 300K. The low thermal conductivity of CNT bundle is responsible for the high thermal interfacial resistance of CNT bundle.

## Appendix- A CARBON NANOTUBES

### A. 1 Introduction

Carbon is the 6<sup>th</sup> element in the periodic table and its electron orbital is  $1s^2, 2s^2$ , and  $2p^2$ . Two electrons in  $1s^2$  orbital are core electrons and 4 electrons in last orbital are valence electrons. The wave functions of  $2s$  and  $2p$  are mixed together and make  $sp^n$  hybridization. In the carbon based compound molecules, acetylene has  $sp$  hybridization, polyacetylene has  $sp^2$  hybridization and methane has  $sp^3$  hybridization. The 2 dimensional graphite sheets, which are also called graphene, have  $sp^2$  hybridization. Since the carbon nanotube (CNT) has the cylindrical shape of rolling up with graphene, it has  $sp^2$  hybridization. However, due to the periodicity along the circumferential direction, electronic structure of CNT is different from graphene.

### A. 2 Hybridization in a Carbon Atom

A linear combination of the  $2s$  orbital and one of the  $2p$  orbitals of a carbon atom can form  $sp$  hybridization. The hybridized  $sp$  orbitals, denoted  $|sp_a\rangle$  and  $|sp_b\rangle$ , are expressed by the linear combination of  $|2s\rangle$  and  $|2p_x\rangle$  wavefunctions,

$$|sp_a\rangle = C_1|2s\rangle + C_2|2p_x\rangle \quad (\text{A.1})$$

$$|sp_b\rangle = C_3|2s\rangle + C_4|2p_x\rangle \quad (\text{A.2})$$

where  $C_i$  are coefficients. From the orthonormality conditions,

$$\langle sp_a | sp_b \rangle = \begin{cases} 0 & \text{for } a \neq b \\ 1 & \text{for } a = b \end{cases} \quad (\text{A.3})$$

$C_i$  can be calculated. The equation (A.4) and (A.5) becomes .

$$|sp_a\rangle = \frac{1}{\sqrt{2}}(|2s\rangle + |2p_x\rangle) \quad (\text{A.4})$$

$$|sp_b\rangle = \frac{1}{\sqrt{2}}(|2s\rangle - |2p_x\rangle) \quad (\text{A.5})$$

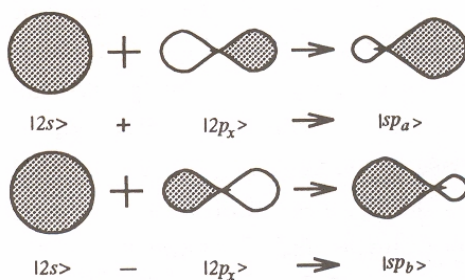


**Figure A.1.**  $sp$  hybridization of  $2p_x$  orbitals (from ref 26)

The schematic view of the  $|sp_a\rangle$  and  $|sp_b\rangle$  orbital is plotted at Fig. A.1. Compared to the  $|2p_x\rangle$  function, the overlap of  $|sp_a\rangle$  with the wavefunction at  $x > 0$  becomes large and this gives rise to a higher binding energy. As an example, consider  $sp$  hybridization of acetylene,  $\text{HC}\equiv\text{HC}$ . The hybridized  $|sp_a\rangle$  orbital of one of carbon atoms forms a covalent bonding with the  $|sp_b\rangle$  orbital of the other carbon atom. This bonding is called a  $\sigma$  bond.

However,  $2p_y$  and  $2p_z$  wavefunctions of each carbon atom are perpendicular to the  $\sigma$  bond and these wavefunctions form relatively weaker bond, which is called  $\pi$  bond. The  $\sigma$  bond which is parallel to HC-CH and two  $\pi$  bonds which are perpendicular to the  $\sigma$  bond in  $\text{HC}\equiv\text{HC}$  are plotted in Fig. A.2.

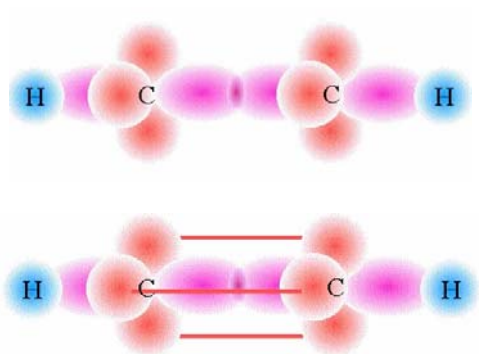


**Figure A.2** Example of  $\sigma$  and  $\pi$  bands wavefunctions in  $\text{HC}\equiv\text{HC}$  (from ref 26)

In  $sp^2$  hybridization, the  $2s$  orbital and two  $2p$  orbitals are hybridized. Ployacetylene ( $\text{HC}\equiv\text{HC-}$ )<sub>n</sub> (See Fig. A.2) is an example of  $sp^2$  hybridization. All  $\sigma$  bonds in ployacetylene are in  $xy$  plane while  $\pi$  bond is perpendicular to the plane.

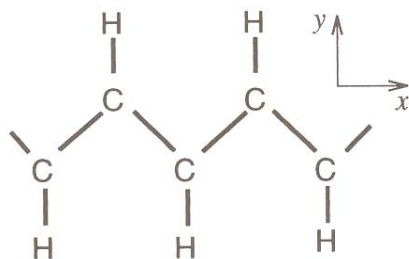


**Figure A.3** Trans-polyacetylene,  $(\text{HC}\equiv\text{HC-})_n$  with  $sp^2$  hybridization (from ref 26)

From Fig. A.3, the direction of  $\sigma$  bonds are given by  $(0,-1,0)$ ,  $(\sqrt{3}/2,1/2,0)$ , and  $(-\sqrt{3}/2,1/2,0)$  and the  $sp^2$  hybridized orbitals  $|sp_i^2\rangle$  where  $i=a,b,c$ , are followings:

$$\begin{aligned}
 |sp_a^2\rangle &= \frac{1}{\sqrt{3}}|2s\rangle - \sqrt{\frac{2}{3}}|2p_y\rangle \\
 |sp_b^2\rangle &= \frac{1}{\sqrt{3}}|2s\rangle + \sqrt{\frac{2}{3}}\left\{\frac{\sqrt{3}}{2}|2p_x\rangle + \frac{1}{2}|2p_y\rangle\right\} \\
 |sp_c^2\rangle &= -\frac{1}{\sqrt{3}}|2s\rangle + \sqrt{\frac{2}{3}}\left\{-\frac{\sqrt{3}}{2}|2p_x\rangle + \frac{1}{2}|2p_y\rangle\right\}
 \end{aligned} \tag{A.6}$$

where all coefficients can be calculated from the orthonormality conditions, equation (A.6). Therefore,  $sp^2$  orbitals have large bonding amplitude along the three nearest neighbor atoms, which is denoted as *trigonal* bonding.

We can expand the same idea for the  $sp^3$  hybridization with the example of methane ( $CH_4$ ). For  $CH_4$ , tetrahedral bond is formed with nearest neighbor atoms with the direction of  $(1,1,1)$ ,  $(-1,-1,1)$ ,  $(-1,1,-1)$  and  $(1,-1,1)$ . Generally,  $n+1$  electrons are belong to the hybridized  $\sigma$  bond whereas  $4-(n+1)$  electrons are in  $\pi$  orbital. Therefore, 4 electrons in  $2s^1$  and  $2p^3$  states are in  $\sigma$  bond and no  $\pi$  bond is available for  $sp^3$  hybridization.

### A. 3 Tight Binding calculation of Molecules and Solids

In lattice structure, the unit cells are repeated in the direction of lattice vector, which satisfy Bloch's theorem.

$$T_{\vec{a}_i} \Psi = e^{i\vec{k} \cdot \vec{a}_i} \Psi \quad (i=1, \dots, 3) \quad (\text{A.7})$$

where  $T_{\vec{a}_i}$  is a translational operation along the lattice vector  $\vec{a}_i$  and  $\vec{k}$  is the wave vector. One of the functional form which satisfy equation (A.10) is j-th atomic orbital in the unit cell in the lattice. A tight binding, Bloch function  $\Phi_j(\vec{k}, \vec{r})$  is given by,

$$\Phi_j(\vec{k}, \vec{r}) = \frac{1}{\sqrt{N}} \sum_{\vec{R}} e^{i\vec{k} \cdot \vec{R}} \varphi_j(\vec{r} - \vec{R}), \quad (j=1, \dots, n) \quad (\text{A.8})$$

where  $\vec{R}$  is the position of the atom and  $\varphi_j$  denotes the atomic wavefunction in state j.

From the Bloch's theorem, equation (A.10), the translation operation of equation (A.11) is

$$\Phi_j(\vec{k}, \vec{r} + \vec{a}) = e^{i\vec{k} \cdot \vec{a}} \Phi_j(\vec{k}, \vec{r}) \quad (\text{A.9})$$

where the periodic boundary condition for the  $M=N^{-1/3}$  unit vectors in each  $\vec{a}_i$  direction is applied. Then equation (A.12) becomes

$$\Phi_j(\vec{k}, \vec{r} + M\vec{a}) = \Phi_j(\vec{k}, \vec{r}) \quad (i=1, \dots, 3) \quad (\text{A.10})$$

consistent with the boundary condition,  $T_{M\vec{a}_i} = 1$ . From the boundary condition, the phase factor in equation (2.10) gives following relation,

$$k = \frac{2p\pi}{M\bar{a}_i} \quad (\text{A.11})$$

where p is the integer.

Now, consider the energy state of the solid lattice system. The eigenfunctions  $\Psi_j(\vec{k}, \vec{r})$  in the solid can be expressed by the linear combination of Bloch functions  $\Phi_{j'}(\vec{k}, \vec{r})$  with the coefficients,  $C_{jj'}(\vec{k})$  as follow,

$$\Psi_j(\vec{k}, \vec{r}) = \sum_{j'=1}^n C_{jj'}(\vec{k}) \Phi_{j'}(\vec{k}, \vec{r}) \quad (\text{A.12})$$

Now, the eigenvalue of the j-th wavefunction,  $E_j(\vec{k})$ , is given  $\vec{k}$  by following equation:

$$E_j(\vec{k}) = \frac{\langle \Psi_j | H | \Psi_j \rangle}{\langle \Psi_j | \Psi_j \rangle} = \frac{\int \Psi_j^* H \Psi_j dr}{\int \Psi_j^* \Psi_j dr} \quad (\text{A.13})$$

where H is the Hamiltonian of the solid. Substituting equations (A.15) into (A.16), after change subscripts, we get

$$E_i(\vec{k}) = \frac{\sum_{j,j'}^n C_{ij}^* C_{ij'} \langle \Psi_j | H | \Psi_{j'} \rangle}{\sum_{j,j'}^n C_{ij}^* C_{ij'} \langle \Psi_j | \Psi_{j'} \rangle} = \frac{\sum_{j,j'}^n H_{ij'}(\vec{k}) C_{ij}^* C_{ij'}}{\sum_{j,j'}^n S_{jj'}(\vec{k}) C_{ij}^* C_{ij'}} \quad (\text{A.14})$$

Here,  $H_{jj'}(\vec{k})$  and  $S_{jj'}(\vec{k})$  are called transfer integral matrices and overlap integral

matrices respectively. When both matrices  $H_{jj'}(\vec{k})$  and  $S_{jj'}(\vec{k})$  are defined by  $n \times n$  matrix for a given  $\vec{k}$  value, the coefficient  $C_{ij}^*$  is optimized so as to minimize  $E_j(\vec{k})$ . Namely, from the minimum condition of partial derivative at zero,  $\partial E_i(\vec{k})/\partial C_{ij}^* = 0$  the following relation is obtained.

$$\sum_{j''=1}^N H_{jj''}(\vec{k})C_{ij''} = E_i(\vec{k}) \sum_{j''=1}^N S_{jj''}(\vec{k})C_{ij''} \quad (\text{A.15})$$

This equation can be more compact from with the definition of column vector,  $C_i$ ,

$$C_i = \begin{pmatrix} C_{i1} \\ \vdots \\ C_{iN} \end{pmatrix} \quad (\text{A.16})$$

$$[H - E_i(\vec{k})S]C_i = 0 \quad (\text{A.17})$$

At this point, if the inverse matrix of  $[H - E_i(\vec{k})S]$  exists, equation A.20 becomes  $C_i = 0$  which means no wavefunction exists. Therefore, eigenfunctions exist only when the inverse matrix does not exist. Namely,

$$\det[H - E_i(\vec{k})S] = 0 \quad (\text{A.18})$$

where equation (A.21) is called the secular equation.

## A. 4 Electronic structure of Polyacetylene

In this section, we consider the electronic structure of polyacetylene which structure is close to the 2 dimensional graphite structures. The unit cell of trans-polyacetylene  $(CH)_x$  contains two equivalent carbon atoms as it is plotted in Fig. A.4. As it was discussed before, each carbon atom has one  $\pi$  electron which is perpendicular to the plane they makes two  $\pi$ -energy bands within carbon atoms pair. One energy band is called bonding and the other is called anti-bonding  $\pi$  band.

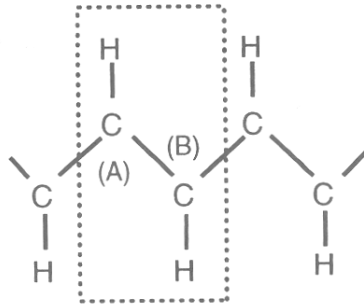


**Figure A.4** The unit cell of trans-polyacetylene bounded by a box defined with dotted lines. (from ref 26)

The atom A and B are periodically repeated as unit cell and the Bloch orbitals consisting of A and B atoms are given by

$$\Phi_j(\vec{k}, \vec{r}) = \frac{1}{\sqrt{N}} \sum_{R_\alpha} e^{ikR_\alpha} \varphi_j(\vec{r} - R) \quad (\text{A.19})$$

where the summation is taken over the atom site for A or B. In order to calculate the eigenvalues of this system,  $(2 \times 2)$  Hamiltonian matrix,  $H_{\alpha\beta}$ , ( $\alpha$  for A and  $\beta$  for B), is

obtained by substituting equation (2.19) into  $H_{jj'}(\vec{k})$ . First, consider Hamiltonian for the same atom, AA (or BB),  $H_{AA}(\vec{k})$

$$\begin{aligned}
H_{AA}(r) &= \frac{1}{N} \sum_{R,R'} e^{ik(R-R')} \langle \varphi_A(r-R') | H | \varphi_A(r-R) \rangle \\
&= \frac{1}{N} \sum_{R=R'} \varepsilon_{2p} + \frac{1}{N} \sum_{R=R' \pm a} e^{\pm ik} \langle \varphi_A(r-R') | H | \varphi_A(r-R) \rangle \\
&\quad + (\text{terms equal to or more distance than } R=R' \pm 2a) \\
&= \varepsilon_{2p} + (\text{terms equal to or more distance than } R=R' \pm a) \quad (A.20)
\end{aligned}$$

In equation (2.23), the maximum energy is obtained when the matrix element of  $H_{AA}$  comes from  $R=R'$ , which gives  $H_{AA}=\varepsilon_{2p}$ . By the same way,  $H_{BB}$  has the value of  $\varepsilon_{2p}$ .

Next, we consider the  $H_{AB}$ . In this case, the major contribution on  $H_{AB}$  is when atom A and atom B are the nearest neighbor. For this case,  $R'$  becomes  $R'=R \pm a/2$  and  $H_{AB}$  is given by

$$\begin{aligned}
H_{AB}(r) &= \frac{1}{N} \sum_R \{ e^{ika/2} \langle \varphi_A(r-R) | H | \varphi_B(r-R-a/2) \rangle + e^{-ika/2} \langle \varphi_A(r-R) | H | \varphi_B(r-R+a/2) \rangle \} \\
&= 2t \cos(ka/2) \quad (A.21)
\end{aligned}$$

where  $t$  can be written as

$$t = \langle \varphi_A(r-R) | H | \varphi_B(r-R \pm a/2) \rangle \quad (A.22)$$

From the Hermitian conjugation relation,  $H_{AB} = H_{BA}^*$  and since  $H_{AB}$  is real,  $H_{AB} = H_{BA}$ .  $S_{ij}$  can be calculated the same way with  $H_{ij}$ . With the normalized wavefunctions,

$S_{AA}=S_{BB}=1$  and  $S_{AB}=S_{BA}=2s\cos(ka/2)$ , where  $s$  is the overlap integral between nearest atoms, A and B,

$$s = \langle \varphi_A(r-R) | \varphi_B(r-R \pm a/2) \rangle \quad (\text{A.23})$$

Now, all component of  $2 \times 2$  matrix of secular equation are collected and for  $2p_z$  orbital ( $\pi$  bonding) of  $[(CH)_x]$ , the results of secular equation yield the eigenvalues of the energy dispersion relations,

$$E_{\pm}(\vec{k}) = \frac{\varepsilon_{2p} \pm 2t \cos(ka/2)}{1 \pm 2s \cos(ka/2)}, \quad \left(-\frac{\pi}{a} < k < \frac{\pi}{a}\right) \quad (\text{A.24})$$

In Fig. A.5, the graphical results of equation (A.26) is plotted, where  $+$  and  $-$  sign corresponds to each branch. The energy level  $E_+$  ( $k$ ) and  $E_-(k)$  are called bonding  $\pi$  and antibonding  $\pi^*$  energy bands, which are stated in early of this section. The level of  $E_+$  and  $E_-$  are degenerate at  $ka = \pm\pi$ .

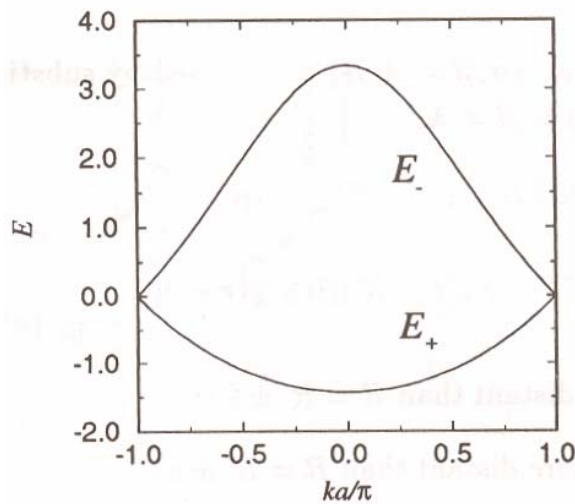


**Figure A.5** The energy dispersion relation  $E_{\pm}(k)$  for polyacetylene  $[(CH)_x]$ . (from ref 26)

## A. 5 Two Dimensional Graphite (Graphene)

Since the carbon nanotube has the cylindrical shape which is rolled up with graphite sheet, it is very important to understand the energy state of graphite sheet. Graphite is the three dimensional structure which composed with two dimensional hexagonal lattice layers as shown in Fig. A.6. The distance between graphite layers is  $3.35\text{\AA}$ . A single graphite layer is called 2D graphite or graphene.

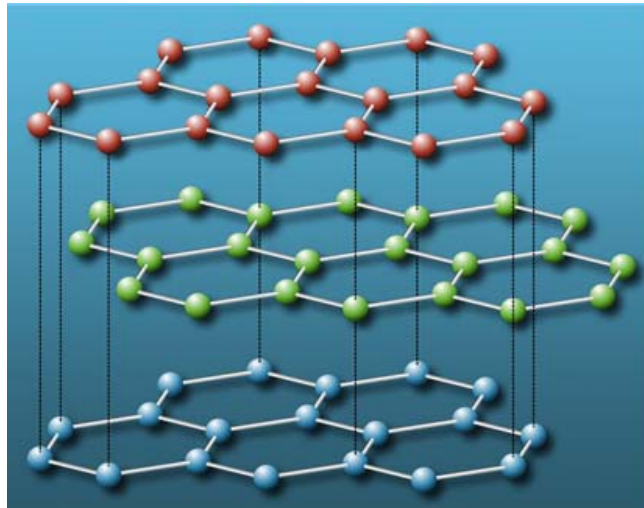


**Figure A.6** The structure of graphite with graphene layers (from ref 26)

In Fig. A.7, the unit cell and the Brillouin zone of graphene is plotted with unit vector,  $\vec{a}_1$ ,  $\vec{a}_2$  and reciprocal lattice vectors,  $\vec{b}_1$ ,  $\vec{b}_2$  on reciprocal lattice. As it was discussed at chapter 2.4, three  $\sigma$  bonds are hybridized in  $sp^2$  configuration with parallel to the graphite plane and two  $\pi$  covalent bonds are perpendicular to the graphene plane with  $2p_z$ .

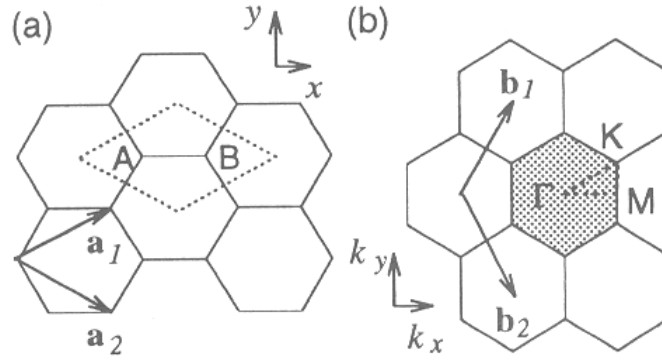


**Figure A.7** (a) The unit cell and (b) the Brillouin zone of two dimensional graphite. (from ref 26)

### ● $\pi$ Bands of graphene

In this section, we consider the  $\pi$  energy band of graphene. As it is discussed in chapter A.4, the Hamiltonian of single atom A and B in Fig A.4 are calculated as  $H_{AA}=H_{BB}=\epsilon_{2p}$ . The difference between polyacetylene and graphene is that there are three more nearest carbon atoms for each A and B site which are corresponding to the off diagonal matrix element of H. If we put three distance vectors  $\vec{R}_1$ ,  $\vec{R}_2$ , and  $\vec{R}_3$  from site A to nearest atom site, B,  $H_{AB}$  can be written as

$$H_{AB} = t(e^{i\vec{k}\cdot\vec{R}_1} + e^{i\vec{k}\cdot\vec{R}_2} + e^{i\vec{k}\cdot\vec{R}_3}) = tf(\mathbf{k}) \quad (\text{A.25})$$

where  $t$  is given by equation (A.25) and  $f(\mathbf{k})$  is a function of the sum of the phase factors of  $e^{i\vec{k}\cdot\vec{R}_j}$ ,  $(j=1, \dots, 3)$ . The function  $f(\mathbf{k})$  can be written with  $x, y$  coordinates of Fig. A.4. as

following.

$$f(k) = e^{ik_x a / \sqrt{3}} + 2e^{-ik_x a / 2\sqrt{3}} \cos\left(\frac{k_y a}{2}\right) \quad (\text{A.26})$$

In this case, the Hamiltonian is complex conjugate since  $f(k)$  is complex function. Therefore,  $H_{BA} = H_{AB}^*$ . The overlap matrix  $S$  can be also calculated by similar way. For the same atom site,  $S_{AA} = S_{BB} = 1$  and for diagonal matrix elements,  $S_{AB} = sf(k) = S_{BA}^*$ , where  $s$  is given by equation (A.26). Therefore,  $H$  and  $S$  are given by

$$H = \begin{pmatrix} \varepsilon_{2p} & tf(k) \\ tf(k)^* & \varepsilon_{2p} \end{pmatrix} \quad S = \begin{pmatrix} 1 & sf(k) \\ sf(k)^* & 1 \end{pmatrix} \quad (\text{A.27})$$

Therefore, the secular equation can be calculated with above expression and give the eigenvalues of the system as:

$$E_{g2D}(\vec{k}) = \frac{\varepsilon_{2p} \pm t\omega(\vec{k})}{1 \pm s\omega(\vec{k})} \quad (\text{A.28})$$

where + sign corresponds to the bonding  $\pi$  energy band whereas – sign corresponds to the anti-bonding  $\pi^*$  energy band. The function  $\omega(\vec{k})$  is given by  $\omega(\vec{k}) = \sqrt{|f(\vec{k})|^2}$ .

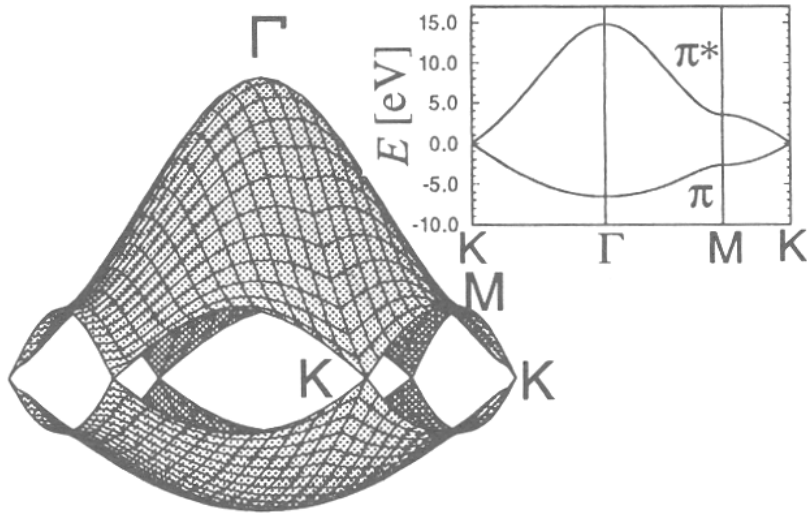


**Figure A.8** The energy dispersion relations for 2D graphite in the whole region of the Brillouin zone. (from ref 26)

The energy dispersion relation is plotted in Fig. A.8 for the Brillouin zone. For this results, the parameters of  $\varepsilon_{2p}=0$ ,  $t=-3.033\text{eV}$ , and  $s=0.129$  are used. The upper half dispersion curve is the anti-bonding  $\pi^*$  energy band and the lower half curve is the bonding  $\pi$  energy band. As it was mention earlier, there are two  $\pi$  electrons in graphene, and these two electrons are fully occupied the lower  $\pi$  energy band. The density of states at the Fermi level is zero for graphene and it makes the graphene a zero-gap semiconductor. At the point K, the energy gap becomes zero and this indicates that two carbon atom sites A and B in hexagonal lattice are equivalent.

## A. 6 Electronic Structure of Carbon Nanotube

The electronic structure of carbon nanotube can be obtained from that of two

dimensional graphite sheets (graphene). There are two directional vectors which determine the physical structure of nanotube, (1) the chiral vector  $\vec{C}_h$  and (2) the translational vector  $\vec{T}$ . The periodicity of the boundary condition is determined by chiral function  $\vec{C}_h$ , which quantized the wave vector in circumferential direction. However, the wave function along the translational vector  $\vec{T}$  remains continuous for nanotube axial direction.

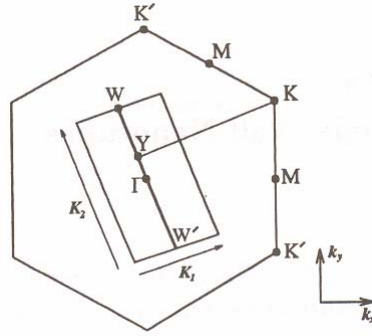


**Figure A.9** The condition for metallic energy bands (from Ref 26).

Along the chiral vector  $\vec{C}_h$  direction, the energy dispersion relations of two dimensional graphite,  $E_{g2D}(K)$  at line segments shifted from  $WW'$  by  $\mu\vec{K}_1$  ( $\mu=0, \dots, N-1$ ). These are folded on the wave vectors parallel to  $\vec{K}_2$  coincide with  $WW'$  as shown in Fig. A.9 and  $N$  pairs of 1D energy dispersion relations  $E_\mu(K)$  are obtained. These 1D energy dispersion relations are given by

$$E_\mu(k) = E_{g2D}\left(k \frac{\vec{K}_2}{|\vec{K}_2|} + \mu\vec{K}_1\right), \quad (\mu=0, \dots, N-1, \text{ and } -\pi/T < k < \pi/T) \quad (\text{A.29})$$

and it is corresponding to the energy dispersion relations of a single wall carbon nanotube. For a arbitrary (n,m) nanotube, if the cutting line passes a point through the K point and if its  $\pi$  and  $\pi^*$  energy band degenerate by symmetry, one dimensional energy band have a zero energy gap as it was discussed in chapter A.5. In addition, the density of state at the Fermi level has a finite value and this makes the system metallic. However, if the cutting line does not pass through the point K, then the nanotube's behavior becomes semiconducting due to the finite energy gap between the valence and conducting bands. Therefore, whenever the ratio of vector YK becomes an integer, the nanotube becomes metallic. Since the vector YK is given by

$$\vec{YK} = \frac{2n+m}{3} \vec{K}_1 \quad (\text{A.30})$$

if (2n+m) or (n-m) equal to a multiple of 3, the nanotube is metallic. The armchair nanotube (n,n) is always metallic and the zigzag nanotube (n,0) is metallic only when n is multiple of 3.

## References

---

- 1 S. Iijima, **Nature** (London) 354, 56 (1991)
- 2 P. KIM, L. Shi, A. Majumdar, and P. L. McEuen, **Phys. Rev. Lett.** 87, 215502 (2001)
- 3 B. T. Kelly, Physics of Graphite, **Applied Science Publishers** (1981)
- 4 J. E. Graebner, H. Altmann, N. M. Balzaretti, R. Campbell, H. –B. Chae, A. Degiovanni, R. Enck, and A. Feldman, ” **Diamond and Related materials** 7, 1589 (1998)
- 5 J.H.Cho, C.D. Richards, D.F. Bahr, R.F. Richards, and J.Jiao, **ASME Int. Mech. Eng. Congress and RD & D Expo**, 1 (2006)
- 6 Jun Xu, T. S. Fisher, **International Society Conferences on Thermal Phenomena** ,549 (2004)
- 7 Y. Wu, C. H. Liu, H. Huang, and S. S. Fan, **Appl. Phys. Lett.** 87, 216108 (2005)
- 8 B. A. Cola, X. Xu and T. S. Fisher, **Appl. Phys. Lett.** 90, 093513 (2007)
- 9 P. B. Amama, B. A. Cola, T. D. Sands, X. Xu and T. S. Fisher, **Nanotechnology** 18, 385303 (2007)
- 10 P.L. Kapitza, "The study of heat transfer in Helium II," **Zhurnal ksperimentalnoi i teoreticheskoi fiziki**, 11, 1-31 (1941)
- 11 C. W. Padgett and D. W. Brenner, **Nano Lett.** 4, 1051 (2004)
- 12 S. Shenogin, L. Xue, R. Ozisik, P. Keblinski and D. G. Cahill, **J. Appl. Phys.** 95, 8136 (2004)
- 13 H. Zhong and J. R. Lukes, **Phys. Rev. B.** 74, 125403 (2006)
- 14 S Maruyama, Y. Igarashi, T. Tanisuchi and Y. Shibuta **Proceedings of the 1<sup>st</sup> International Symposium on Micro and nano technology** 1 (2004)
- 15 J. S. Robert, M. N. Pamela and V. Z. Leonid, **IMECE2004-60334**
- 16 A. Desai, S. Mahajan, G. Subbarayan, W. Jones, J. Geer, B. Sammakia, **J. Electronic Packaging**, 128, 92 (2006)

- 
- 17 H. Zhong and J. R. Lukes, **Phys. Rev. B.** 74, 125403 (2006)
  - 18 J. Tersoff, **Phys. Rev. B.** 39, 5566-5568 (1988)
  - 19 H.F. Chuang, S. M. Cooper, M. Meyyappan, and B. A. Cruden, **J. Nanosci. Nanotech.** 4, 964 (2004)
  - 20 Jun X, T. S. Fisher, **Int. J. of Heat and Mass Transfer** 49, 1658-1666 (2006)
  - 21 P. B. Amama, B. A. Cola, T. D. Sands, X. Xu and T. S. Fisher, **Nanotechnology** 18, 385303 (2007)
  - 22 J.H.Cho, "Design Fabrication, and Characterization of a MEMS Thermal Switch and Integration with a Dynamics Micro Heat Engine, dissertation, 48, 2007.
  - 23 H.F. Chuang, S. M. Cooper, M. Meyyappan, and B. A. Cruden, **J. Nanosci. Nanotech.** 4, 964 (2004)
  - 24 S. Shenogin, L. Xue, R. Ozisik, P. Keblinski and D. G. Cahill, **J. Appl. Phys.** 95, 8136 (2004)
  - 25 S. T. Huxtable, D. G. Cahill, S. Shenogin, L. Xue, R. Ozisik, P., Barone, M. Usrey, M. S. Strano, G. Siddons, M. Shim, and P., Keblinski, **Nat. Mater.** 2, 731 \_2003.
  - 26 R. Saito, C. Dresselhaus and G. Dresselhaus, **Physical Properties of carbon nanotubes**, Imperial College Press, London, 1998.
  - 27 <http://www.tipmagazine.com/tip/INPHFA/vol-10/iss-1/p24.html>
  - 28 J. E. Graebner, H. Altmann, N. M. Balzaretta, R. Campbell, H. –B. Chae, A. Degiovanni, R. Enck, and A. Feldman, ” **Diamond and Related materials** 7, 1589 (1998)
  - 29 C. Yu, L. Shi, Z. Yao, D. Li, and A. Majumdar, **Nano lett.** 5, 1842 (2005)
  - 30 M. S. Dresselhaus, G. Dresselhaus, Ph. Avouris (Eds.): **Carbon Nanotubes, Topics Appl. Phys.** 80, J. Hones, 273-286 (2001)
  - 31 Y. Xiao, X. H. Yan, J. X. Cao, and J. W. Wang, **J. Phys.: Condens. Matter** 15, L341

- 
- (2003).
- 32 J. Hone, M. Whitney, C. Piskoti, and A. Zettl, **Phys. Rev.** B59, R2514 (1999)
- 33 Yi, W.; Lu, L.; Zhang, D.L.; Pan, Z.W.; Xie, S.S. **Phys. Rev., B** 1999, 59, R9015–R9018.
- 34 J. Hone, M. C. Llaguno, N. M. Names, and A. T. Johnson, **App. Phys. Lett.** 77, 666 (2000)
- 35 Motoo Fujii, Xing Zhang et al, **Phys. Rev. Lett.** 95, 065502, (2005)
- 36 Eric Pop, David Mann, Qian Wang, Kenneth Goodson, and Hongkie Dai, **Nano letters** Vol 6, No. 1 96-100
- 37 M. A. Osman and D. Srivastava, **Nanotechnology** 12, 21 (2001)
- 38 S. Maruyama, **Physica B**, 323, 193 (2002).
- 39 S. Berber, YK. Kwon, and D. Tomanek, **Phys. Rev. Lett.** 84, 4613 (2000)
- 40 Z. Yao, J. S. Wang, B. Li, and G. R. Liu, **Phys. Rev. B** 71, 085417 (2005)
- 41 M.A. Osman, A.W. Cummings and D. Srivastava, In **Molecular Building Blocks for Nanotechnology**, G.A. Mansoori, T.F. George, L. Assoufid and G. Zhang, Eds., New York Springer, 2007. Chapter 7. (2001)
- 42 Wei Zhang, et al, **Nanotech.** 15, 936-939, 2004
- 43 J. Cho, T. Wiser, C. Richards, D. Bahr, R. Richards, **Sensors and Actuators A** 133, 55-63 (2007)
- 44 Jun Xu, T. S. Fisher, **International Society Conferences on Thermal Phenomena** (2004)
- 45 H.F. Chuang, S. M. Cooper, M. Meyyappan, and B. A. Cruden, **J. Nanosci. Nanotech.** 4, 964 (2004)
- 46 Jun. X, T. S. Fisher, **Init. J. of Heat and mass Transfer**, 49 (2006)
- 47 P.L. Kapitza, "The study of heat transfer in Helium II," **Zhurnal kspperimentalnoi**

- 
- iteoreticheskoi fiziki, 11, 1-31 (1941)
- 48 B. Li, J. Lan and L. Wang, **Physical Review Letters**, 95, 104302 (2005)
- 49 R. S. Prasher, P.E. Phelan, **J. Appl. Phys.** 100, 063538 (2006)
- 50 J. S. Robert, M. N. Pamela and V. Z. Leonid, **IMECE2004-60334**
- 51 Swartz, E.T. and R.O. Pohl, 1987, "Thermal resistance at interfaces," **Appl. Phys. Letters**, **51**, pp. 2200-2202.
- 52 H. Zhong and J. R. Lukes, **Phys. Rev. B.** 74, 125403 (2006)
- 53 A. Desai, S. Mahajan, G. Subbarayan, W. Jones, J. Geer, B. Sammakia, **J. Electronic Packaging**, 128, 92 (2006)
- 54 Gibson, J. B. et al, **Phys. Rev.** 120 (1960), 1229
- 55 J Tersoff, **Phys. Rev. Lett.** 61, 2879-2882 (1988)
- 56 J. Tersoff, **Phys. Rev. Lett**, 64, 1757
- 57 D. W. Brenner, **Phys. Rev. B** 42, 9458 1990
- 58 Paul A. Temple and C. E. Hathaway, **Phys. Rev. B.** Vol.7, No8, 1973
- 59 James. S, Larry. W. B and M. S. Gordon, **J. Chem. Phys**, 112 6 2994 (2000)
- 60 S. Berber and A. Oshiyama, **Phys. Rev. Lett.** 96, 105505, (2006)
- 61 [www.iue.tuwien.ac.at/phd/ayalew/node20.html](http://www.iue.tuwien.ac.at/phd/ayalew/node20.html)
- 62 M. A. Osman, and D. Srivastava, **Phys. Rev. B** 72, 125413 (2005)
- 63 J. Shiomi and S. Maruyama, **Phys. Rev. B**, 73, 205420 (2006)
- 64 W. Yi, L. Lu, Z. D. Lin, Z. W. Pan and S. S. Xie, **Phys. Rev. B** 59 9015 (1999)
- 65 R. Saito, C. Dresselhaus and G. Dresselhaus, *Physical Properties of carbon nanotubes*, Imperial College Press, London, 1998. Chapter 9.
- 66 Y. Xiao, X. H. Yan, J. X. Cao, and J. W. Wang, **J. Phys.: Condens. Matter** 15, L341 (2003).
- 67 T. Yamamoto, S. Watanabe, K. Watanabe, **Phys. Rev. Lett.**, 92, 075502 (2004)

- 
- 68 H.E. Jackson and C.T. Walker, **Phys. Rev. B** **3**, 1428 (1971).
- 69 T.F. McNelly, S.J. Rogers, D.J. Channin, R.J. Rollefson, W.M. Goubau, G.E. Schmidt, J.S. Krumhansl and R.O. Pohl, **Phys. Rev. Lett.**, **24**, 100 (1970).
- 70 R. A. MacDonald and D. H. Tsai, **Physics Reports**, **46**, 1 (1978)
- 71 J. Yoon, C. Q. Ru, and A. Mioduchowski, **J. App. Phys.** **93**, 4801 (2003)
- 72 C. Wei, K. Cho and D. Srivastava, **App. Phys. Lett.** **82**, 2512 (2003)
- 73 C. –H. Kiang, M. Endo, P.M. Ajayan, G. Dresselhaus, and M. S. Dresselhaus, **Phys. Rev. Lett**, **81**, 1869 (1998)
- 74 D. Qian, G. J. Wagner, W. K. Liu, M-F. Yu and R. S. Ruoff, **Appl. Mech. Rev.**, **55**, 495 (2002)
- 75 A. N. Cleland, *Foundations of Nanomechanics*, Springer, Berlin, 2003, Chapter 4.
- 76 K. N. Pandey and S. Chand, **Int. J. of Pressure and Piping** **80**, 673, (2003)
- 77 R. Kapoor and N. N Sia, **Mechanics of Materials**, **27**, 1 (1998)
- 78 Y. Wang, X. X. Wang and X. Ni, **Modeling Simul. Mater. Sci. Eng.** **12**, 1099 (2004)
- 79 D. Srivastava, D. W. Brenner, J. D. Schall, K. D. Ausman, M. Yu, and R. S. Ruoff, **J. Phys. Chem. B****103**, 4330 (1999)
- 80 A Santos, MJ Ledesma\_Carbayo, N Malpica, M Desco, JC Antoranz, P Marcos-Alberca, and MA Garcia-Fernandez, Proc. **SPIE Vol. 4325** (2001)
- 81 M. A. Shehadeh, H. M. Zbib and T. Diaz de la Rubia, **Phil. Mag.**, **85**, 1667 (2005)
- 82 R. D. Noebe, C. L. Cullers and R. R. Bowman, **J. Mater. Res.** **7**, 605 (1992)
- 83 X. Hu, K. Albe and R. S. Averback, **J. Appl. Phys** **88**, 49 (2000)
- 84 F. N. Dzegilenko, D. Srivastava and S. Saini, **Nanotech.** **10**, 253 (1999)
- 85 Gromacs User Manual, Ver. 3.3, [www.gromacs.org](http://www.gromacs.org)
- 86 R. B. Capaz, C. D. Spataru, P. Tangeny, M. L. Cohen and S.G. Louie, **Phys. Stat. Sol.**, **241**, 3352, (2005)
- 87 J. Gou and K. Lau, “Modeling and Simulation of Carbon Nanotube / Polymer Composites”, **Handbook of Theoretical and Computational Nanotechnology**, **1**, 1

---

(2005)

- 88 B. Li, J. Lan and L. Wang, **Phys. Rev. Lett**, 95, 104302 (2005)
- 89 N. R. Paravikar, P. Keblinski, A. M. Rao, M. S. Dresslhaus, L. S. Schadler, and P. M. Ajayan, **Phys. Rev. B** 66, 235424 (2002)
- 90 E. G. Noya, D. Srivastava, L. A. Chernozatonskii and M. Menon, **Phys. Rev. B.** 70, 115416 (2004)
- 91 P. A. Temple and E. Hathaway, **Phys. Rev. B.** 7, 3685 (1973)
- 92 Shenogin, L. Xue, R. Ozisik, P. Keblinski and D. G. Cahill, **J. Appl. Phys.** 95, 8136 (2004)
- 93 C. W. Oadgett and D. W. Brenner, **Nano Lett.** 4, 1051 (2004)
- 94 S. Saito, T. M. Inerbaev, H. Mizuseki, N. Igarashi, R. Note and Y. Kawazoe, **Chem. Phys. Lett.** 433, 86 (2006)
- 95 C. J. Twu and J. R. Ho, **Phys. Rev. B.** 67, 205422 (2003)
- 96 R. S. Prasher, P.E. Phelan, **J. Appl. Phys.** 100, 063538 (2006)
- 97 E. Gmelin, M. Asen-Palmer, M. Reuther, and R. Villar, **J. Phys. D: Appl, Phys.** 32 R19, (1999)
- 98 C. Yu, S. Saha, J. Zhou, L. Shi, A. M. Cassell, B. A. Cruden, Q. Nao and J. Li, **J. Heat Transfer**, 128, 235, 2006
- 99 V. P. Sokhan, D. Nicholson and N. Quirke, **J. Chem. Phys.** 113, 2007 (2000)
- 100 J. Che, T. Cagin, and W. A. Goddard III, **Nanotech.** 11 65~69 (2000)